Agent-based mathematical modeling of pancreatic cancer growth and several therapies

Chen, Jiao

DOI
10.4233/uuid:42e7f02f-0844-4367-8678-e2d5a3fa959f

Publication date
2020

Document Version
Final published version

Citation (APA)
Chen, J. (2020). Agent-based mathematical modeling of pancreatic cancer growth and several therapies. https://doi.org/10.4233/uuid:42e7f02f-0844-4367-8678-e2d5a3fa959f

AGENT-BASED MATHEMATICAL MODELING OF PANCREATIC CANCER GROWTH AND SEVERAL THERAPIES

Dissertation

for the purpose of obtaining the degree of doctor
at Delft University of Technology
by the authority of the Rector Magnificus prof. dr.ir. T.H.J.J. van der Hagen
chair of the Board for Doctorates
to be defended publicly on
Thursday 23 January 2020 at 12:30 o'clock

by

Jiao CHEN

Master of Science in Biochemistry and Molecular Biology,
Northwest A&F University, China
born in Xian Yang, Shaanxi Province, China

This dissertation has been approved by the promotors Prof. dr. ir. C. Vuik and Dr. ir. F. J. Vermolen.

Composition of the doctoral committee:

Rector Magnificus,	chairman
Prof. dr. ir. C. Vuik	Delft University of Technology, promotor
Dr. ir. F. J. Vermolen	Delft University of Technology, promotor
Independent members:	
Prof. dr. A. Madzvamuse	University of Sussex, the United Kingdom
Prof. dr. ir. L. Geris	Katholieke Universiteit Leuven, Belgium
Prof. dr. ir. A. W. Heemink	Delft University of Technology
Prof. dr. A. A. Zadpoor	Delft University of Technology
Prof. dr. ir. C.W. Oosterlee	Delft University of Technology, reserve member
Dependent members:	
Dr. D. Weihs	Technion-Israel Institute of Technology, Israel

Keywords: Reaction-diffusion equation, Biomechanics, Cell-based modeling, Cellular automata, Monte Carlo simulations, Pancreatic cancer, Cancer therapy

This research was supported by the China Scholarship Council (CSC).

ISBN 978-94-6366-245-1
Printet by: ProefschriftMaken
An electronic version of this dissertation is available at
https://www.globalacademicpress.com/ebooks/jiao_chen

SUMMARY

Cancer is known as one of the leading causes of death in the world with difficult diagnose at early stages, poor prognosis and high mortality. Animal-based experiments and clinical trials have always been the main approach for cancer research, albeit they may have limitations and ethical issues. Mathematical modeling as an efficient method is used to predict results, optimize experimental design and reduce animal use. Our work focuses on the phenomenological simulation of cancer progression and therapies at the cell scale level.

Pancreatic cancer has a rare structure where cancer cells preferably accumulate into clusters at early stages and cause a cancer-associated desmoplastic extracellular matrix (ECM) to be produced circumferentially around it. This desmoplastic ECM is anisotropic and plays as a physical defense for cancer cells against the entry of some agents, e.g. immune cells, drugs, etc. To investigate the impacts of anisotropic ECM on the migration of immune cell T-lymphocytes at early stages, we develop a model on cell migration in T-lymphocytes mediated antitumor response with an application to pancreatic cancer in Chapter 2. Cell displacement is updated by solving a large system of stochastic differential equations with the Euler-Maruyama method. As expected, our cell-based model is able to show the phenomenon successfully, where T-lymphocytes can hardly invade cancer cells under anisotropic ECM orientation. Furthermore, the obstructing effect of ECM orientation enhances the progression of the tumor with the increase in the degree of anisotropy. In addition, the model predicts cancer growth under various immune conditions.

As an extension in Chapter 3, the model is refined and applied to the stage of treatment. Gemcitabine is known as the front-line drug for pancreatic cancer therapy, which inhibits the proliferation of cancer cells. Since this drug is often used in conjunction with other drugs, we combine gemcitabine with another drug that can weaken the anisotropic ECM orientation. The enzyme PEGPH20 aims at depleting hyaluronan in desmoplastic ECM and hence increases the penetration of many different agents. Therefore, the therapeutic model of PEGPH20 + gemcitabine is considered and compared with the corresponding mouse-based experiments in the literature. The concentration of drugs is based on Green's fundamental solutions of the reaction-diffusion equation. The administration of drugs is assumed to be given by injections, and the results show that PEGPH20 enzyme-mediated therapy facilitates the anti-tumor immune response. However, the likelihood of success of a cure relies on the stage of diagnosis and timely treatment. To investigate the correlations of possibilities of success of the therapy and uncertainties of input parameters, Monte Carlo simulations are performed in a two-dimensional model. To conclude, the likelihood of healing significantly reduces as the treatment is postponed. Moreover, the model is able to predict the likelihood of success of the therapy and to provide a reference for experiment design regarding the drug dose according to different stages of cancer progression.

To mimic a larger scale like tissue level, we set up a three-dimensional cellular automata model with an application to pancreatic cancer in Chapter 4. This chapter presents a simulation of oncolytic virotherapy, which employs genetically modified viruses that selectively kill cancer cells. The spread of viruses is modeled by using the diffusion-reaction equation that is discretized by the finite difference method and integrated by the IMEX approach. Furthermore, some cell biomedical processes are dealt with using probabilistic principles. As we expected, this cellular automata model can simulate the cancer progression at early stages and cancer attenuation under viral intervention well. Since the residual viruses may have toxicity to patients, Monte Carlo simulations are performed to investigate the correlations between input variables and numerical results (total residual viruses and cancer area).

Albeit desmoplastic ECM inhibits the entry of agents, cancer cells are able to degrade the ECM by secreting enzyme MMPs once they start to metastasis. Metastasis is a major cause of cancer mortality, and cells normally undergo many morphological changes during the transmigration. Therefore, we develop a model of cell deformation where also the deformation of the nucleus is incorporated in two and three-dimensions in Chapter 5. The movement of migrating cells is chemotaxis/ durotaxis treated by using Green's fundamental solutions and an IMEX time integration method is used to update the displacement of cells. In addition, Poisseuille flow is incorporated to simulate a microvascular flow, where the bloodstream is treated as an incompressible fluid. As a result, this is a successful model to describe morphological evolution of one cell and its nucleus when it encounters the specific obstacles or paths during the metastasis. Analogously, Monte Carlo simulations are carried out to quantitatively evaluate the impact of uncertainties on numerical results.

Mathematical modeling reshapes the understanding of cancer and it will definitely be a useful tool for the optimization of cancer therapy and for cancer research in the future.

SAMENVATTING

Kanker is bekend als een van de belangrijkste doodsoorzaken met, als de kanker in een vroeg stadium is, een moeilijke diagnose-stelling. Verder zijn de prognoses voor patiënten veelal slecht en is de sterftekans niet zelden hoog. Dierproeven en klinische proeven zijn altijd, ondanks hun beperkingen en ethische bezwaren, de belangrijkste methoden geweest in wetenschappelijk onderzoek naar kanker. Wij stellen dat wiskundig modelleren als een efficiënte methode gebruikt kan worden om verschillende scenario's te voorspellen, therapie te optimaliseren, en om het aantal dierproeven te verminderen. Het huidige werk simuleert de ontwikkeling van kanker en therapie op cel niveau.

Alvleesklierkanker heeft een zeldzame eigenschap waarin kankercellen zich in de vroege stadia bij voorkeur opéénhopen in groepjes (clusters) en daarmee het aanmaken van een kanker-geassocieerd desmoplastische extracellulaire matrix (ECM) rond een cluster tot stand brengen. Dit desmoplastische ECM is anisotroop en manifesteert zich als een fysieke barrière die de kankercellen beschermt tegen invloeden van buitenaf, zoals immuumcellen (T-lymphocyten), en medicatie. Om de invloed van het anisotrope ECM op de migratie van immuumcellen in vroege stadia te kwantificeren, ontwikkelen we in hoofdstuk 2 een model voor celmigratie van T-lymphocyten die werkzaam zijn tegen het ontstaan en ontwikkelen van alvleesklierkanker. De verplaatsing van cellen wordt berekend door het oplossen van een groot stelsel stochastische differentiaalvergelijkingen met behulp van de Euler-Maruyama methode. Zoals verwacht is ons celmodel in staat om het verschijnsel, dat de T-lymphocyten nauwelijks de kankercellen kunnen opruimen als de ECM anisotroop is, te reproduceren. Men ziet dat een meer anisotrope oriëntatie van de ECM voor een snellere ontwikkeling van de tumor zorgt. Verder voorspelt het model groei van kanker onder verschillende sterktes van het afweersysteem van de patiënt.

In hoofdstuk 3 komt een uitbreiding van dit model aan de orde. Het model wordt verder verfijnd om de invloed van therapie door te rekenen. Gemcitabine is een bekend medicijn om alvleesklierkanker te behandelen. Dit medicijn verlaagt de intensiteit van deling van kankercellen. Omdat dit medicijn vaak gebruikt wordt in combinatie met andere medicatie, wordt hier gemcitabine gecombineerd met een medicijn dat zorg draagt voor het terugbrengen van de anisotropie van ECM. Het enzym PEGPH20 zorgt voor het verwijderen van hyaluronan in desmoplastische ECM waardoor veel andere stoffen de kans krijgen om de ECM binnen te dringen. Daarom beschouwen we een therapeutisch model van een cocktail van PEGPH20 en gemcitabine en vergelijken we de modeluitkomsten met experimenten uit de literatuur op muizen. Het veld van de concentratie van de medicijnen wordt berekend door middel van Greense fundamentaaloplossingen van de reactie-diffusie vergelijking. We nemen in de simulaties aan dat het toedienen van de medicatie plaatsvindt door injecties, en de resultaten laten zien dat PEGPH20 enzym-geinduceerde therapie de afweer tegen kanker versterkt. De kans op succes van een behandeling hangt dan af van het moment van diagnose en het moment waarop met de therapie wordt begonnen. Om de correlaties met een succesvolle behandeling en de onzekerheid in de invoerparameters te onderzoeken, worden Monte Carlo simulaties gebruikt in een twee-dimensionaal model. We kunnen hiermee in kaart brengen hoe de kans op succes van de behandeling kleiner wordt als met de behandeling later wordt begonnen. Het model is hiermee in staat richtlijnen te geven voor een benodigde dosis medicatie om alvleesklierkanker te bestrijden als op verschillende stadia begonnen wordt. Bij te laat beginnen met de medicatie is de kans op succes helaas verwaarloosbaar.

Om op een grotere fysische schaal te simuleren, hebben we in hoofdstuk 4 een drie-dimensionaal cellular automata model opgezet voor alvleesklierkanker. Dit hoofdstuk beschrijft een simulatie van oncolytische virale therapie waarin genetisch gemodificeerde virussen selectief kankercellen aanvallen. De verspreiding van virussen wordt gemodelleerd met een reactie-diffusie vergelijking die we discretiseren met behulp van een eindige differentiemethode voor de plaatscoordinaten en integreren over de tijd met een IMEX methode. Andere celgerelateerde processen als celmigratie, celdeling en celsterfte worden gemodelleerd met stochastische principes. Zoals verwacht kan dit cellulaire automata model worden gebruikt om de ontwikkeling van kanker gedurende vroege stadia, al dan niet in combinatie met virustherapie, modelleren. Omdat virussen toxiciteitsproblemen kunnen opleveren voor patiënten, worden Monte Carlo methoden gebruikt om de correlaties tussen invoervariabelen en numerieke uitvoer (zoals het totale aantal virussen dat overblijft na de behandeling en het uiteindelijke volume/oppervlakte van de tumor) te onderzoeken.

Hoewel desmoplastische ECM het binnendringen van allerlei stoffen en cellen naar de tumor frustreert, kunnen kankercellen, als ze zich beginnen te verspreiden naar andere delen van het lichaam (uitzaaien), de ECM degraderen door het uitscheiden van enzymatische MMPs. Uitzaaiing van kanker is een zeer belangrijke doodsoorzaak van kankerpatiënten. Kankercellen ondergaan grote morfologische veranderingen (vormveranderingen) tijdens de migratie door de ECM heen om andere delen van het lichaam te bereiken. Om dit in kaart te brengen, wordt in hoofdstuk 5 een model beschreven voor zowel twee- als driedimensionale vormveranderingen (celdeformaties) van kankercellen en hun nuclei. De verplaatsing van de cellen wordt gemodelleerd door chemotaxis of durotaxis mee te nemen en in het model wordt gebruik gemaakt van Greense fundamentaal oplossingen om concentratievelden te berekenen en een IMEX tijdsintegratiemethode om de positie van gridpunten op het celoppervlak en het oppervlak van de celkern te bepalen. Verder wordt de verspreiding in de bloedstroom van een kleine ader gesimuleerd middels een Poisseuille stroming. Deze vereenvoudiging neemt impliciet aan dat de stroming incompressibel is. Dit model beschrijft succesvol de vormveranderingen van een cel en zijn nucleus als deze bepaalde obstakels of paden tegenkomt tijdens de metastase (uitzaaiing). Hier worden weer Monte Carlo methoden gebruikt om de invloed van onzekerheid op de numerieke resultaten in kaart te brengen.

Kort samengevat: Wiskundig modelleren vernieuwt en vergroot het begrip van kanker en dit modelleren is een bruikbaar stuk gereedschap voor het optimaliseren van behandeling van kanker en voor toekomstig wetenschappelijk onderzoek naar kanker.

CONTENTS

1

INTRODUCTION

1.1. BACKGROUD

Cancer has become one of the leading causes of death in developed countries and its global mortality rate is rising [2]. Cancer initiates and develops by a series of processes comprising cell mutation, abnormal proliferation, angiogenesis and metastasis accompanied by the evolution of cell morphology. Many studies have utilized in vitro systems using primary cells or cell lines. While those studies have provided important understanding of cancer, the interaction between cancer cells and their microenvironments is difficult to reproduce accurately. Thus, for more physiologically relevant conditions, animal experiments have been used.

Animal-based experiments have been crucially important in cancer research, in particular in cancer pathology, tumor transplant, immunization and treatment. However, the cruelty and ethical views caused by animal experiments have caused a reduction in their use. In 1959, the conception of 'Three Rs' was proposed as the principles of Replacement, Reduction and Refinement in *The Principles of Humane Experimental Technique* and the concept has been a hot issue in the EU legislation since 1986, aimed at protecting animals [3, 4]. Therefore, in the wake of research requirements and experimental regulations, well designed experiments are crucially important, which definitely need the input from various disciplines like mathematics, physics, computer science, etc.

The contents of this chapter have been published in paper [1]: Jiao Chen, Daphne Weihs and Fred Vermolen. "Computational Cell-Based Modeling and Visualization of Cancer Development and Progression." New Developments on Computational Methods and Imaging in Biomechanics and Biomedical Engineering. Springer, Cham, 2019. 93-119.

To validate developed hypotheses regarding biological processes occurring during cancer development, it is necessary to assess experimental outcomes. Since experimental results are usually represented in the form of patterns and numbers, the developed hypotheses need quantification. This quantification requires the translation of hypotheses into quantitative relations, which generally pose a set of mathematical relations. The combination of the mathematical relations constitutes the backbone of the mathematical model that is used to simulate the biological process of interest. Mathematical models are capable of reproducing situations that are beyond the measured data. Despite all advantages of mathematical modeling, one should be careful in the evaluation of the results due to possible shortcomings in the model. Shortcomings in mathematical models arise from neglecting several features in biological processes due to lack of knowledge, as well as by uncertainty of parametric values. The latter shortcoming requires parameter sensitivity analysis. Facing the societal burden, mathematical modeling of cancer is a promising approach to combine with experiments in vitro and in vivo, using both animal and human materials. On one hand, the modeling results lead to predictions [5] and further description with examples can be found in [6]. On the other hand, with computational modeling, the number of animal trials could be reduced and the experiments can be designed better, however, conversely, mathematical models could be validated by corresponding experiments.

As early as in 1942, a book named ‘On Growth and Form’ by Thompson et al. [7] cited the following quote from a statistician Karl Pearson (first published in 1901):

> `I believe the day must come when the biologist will - without being a mathematician - not hesitate to use mathematical analysis when he requires it`

and presents mathematical principles in his book. A 100 years later, a paper in ‘The Economist’ (2004) stated that

> `If cancer is ever to be understood properly, mathematical models such as these will surely play a prominent role.`

1.2. MATHEMATICAL MODELING

1.2.1. MATHEMATICAL MODELING ON VARIOUS SCALES

Mathematical models have been developed for a broad spectrum of length-scales, ranging from a molecular level (from a few atoms to multitudes of biomolecules) to a tissue level. Fearon and Vogelstein [8] described a conceptual model showing cancer evolution as a series of genetic mutation mainly in tumor oncogenes and suppressor genes. With a further rigorous verification, Gatenby and Vincent [9, 10] found that environmental selection forces are dominated by competition for limited substrate in the era of carcinogenesis. Next to genes, due to a large amount of proteins involved in cancer development and progression, where some of them even become the targets of new drugs, molecular modeling is important and is able to provide details that would not be accessible if solely experiments on the molecular dynamics were carried out [11]. For example, Im ta al. [12] proposed Brownian dynamics for modeling the movement of ions in membrane channels. Binding of proteins and DNA have been described by Chen and Pettitt [13]. Furthermore, molecular mechanics have been described in [14, 15], and other molecular models refer to a review paper by Friedman et al. [11].

Cells constitue the fundamental, independent functional unit of organisms. Cancerous cells display many different features compared to the characteristics of normal constitutive cells, which have been incorporated in various mathematical formalisms. In a cell-based modeling framework, the geometry of one cell can be fixed, see for instance [16, 17]; whereas the cell morphology is also changeable in reality. Rejniak et al. [18] utilized an immersed boundary approach with distributed sources to model the deformable boundary of cells at early stages with application to ductal tumor. Moreover, deformation of cells can also be realized through the simulation of cytoskeleton [19]. Furthermore, the studies in [20, 21] treated the evolving geometry of the cell membrane by combining a moving boundary problem with a system of coupled surface partial differential equations, which are solved by the use of surface finite element methods.

For the study of cancer progression and disease pathology, the modeling of large ensembles of interacting cells in biological tissue is needed. A literature study by Murray [22] proposed several partial differential equation-based models to simulate various biological phenomena like wound healing, cancer development, immune system response on the macro tissue scale. In the context of cancer dissemination and metastasis, clusters of cells have much higher metastatic potentials than singular migrating cancer cells [23, 24]. Based on this, Dudaie et al. described a model on the collective movement of cancer cells on a cell colony level [25] and Jolly et al. developed a model for investigating cluster-based dissemination of breast cancer cells [24]. Taking the CPU time into consideration, parallel computing platforms are feasible for tissue simulation involving large numbers of interacting cells [26].

1.2.2. MATHEMATICAL MODELING FROM A VIEW OF CANCER PROGRESSION

Cancer development involves a chain of biophysical processes including initiation, angiogenesis, metastasis and colonization, of which some of them are sketched in Figure 1.1.

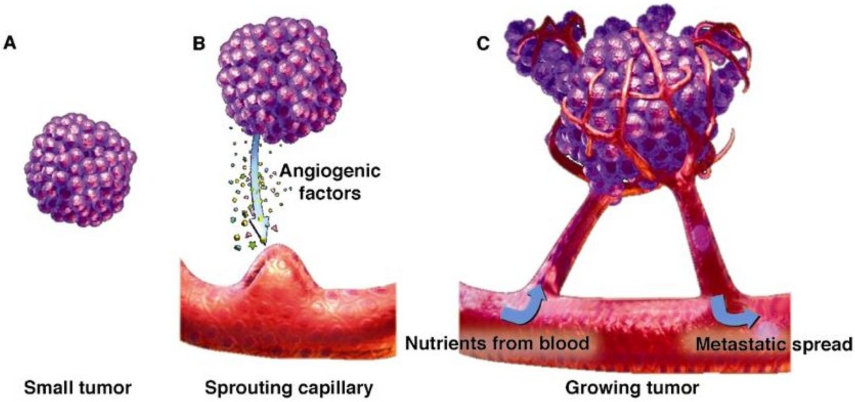

Figure 1.1: The transition from a benign tumor, see left, to a malignant tumor, see right. The interaction of tumor growth and angiogenesis. Taken from Siemann DW, Vascular targeting agents. Horizons in Cancer Therapeutics: From Bench to Bedside. 2002; 3 (2): 4-15 [27].

With a series of gene mutations, normal cells mutate into cancer cells and obtain abnormal properties (i.e. dysfunctional excessive proliferation) [28]. According to the studies by NHS (National Cancer Intelligence Network), early diagnosis of cancer can increase the likelihood for survival significantly. However, during this period cancer is usually difficult to detect. A literature review on cell-based models in which the initial stages of cancer have been modeled is provided in [29]. The importance of early diagnosis motivates the need of strengthening scientific research on the early stages of cancer development both from clinical and in-silico studies. To simulate cancer initiation, Vermolen et al. [30] developed various cell-based models and Enderling et al. [31] developed a model on radiotherapy strategies targeting cancer during its early stages.

Angiogenesis triggers a key transition for tumors from being a dormant avascular phase to reaching a soaring vascular phase [32], see Figure 1.1. Based on this phenomenon, many experimental studies aim at preventing angiogenesis or at cutting off oxygen sources to prevent further development and more importantly metastasis of a tumor. For example, a drug named Avastin is regarded as a powerful means for cutting off the tumor's oxygen supply, however, tumors become more aggressive as a result of further hypoxia [33]. To aid the experiments, mathematical modeling has yielded several contributions such as a 3D angiogenesis model [34], a cellular automata model of growth of blood vessels by Rens et al. [35] and other relevant works [36, 37]. An excellent review about tumor-induced angiogenesis was written by Stephanou et al. [38].

Metastasis is responsible for as much as 90% of cancer-caused mortality [39]. In this case, the migration of cells often proceeds through mechanotaxis, which can be classified into tensotaxis (movement according to mechanical tensions) and durotaxis (migration towards a stiffness gradient). In tensotaxis migration, cells exert forces on their ECM environment, and in turn the stresses, displacements and strains due to cell-induced deformation of the microenvironment can be sensed by neighbouring cells. Those neighbouring cells are then able to migrate according to the mechanical signals. This was experimentally evidenced and modeled in [40–42]. For durotaxis migration, cells tend to move in the direction of a stiffness gradient, and especially cancerous cells show a preference for a stiffer substrate or ECM [42, 43]. The works by Weihs et al. have also shown that the stiffness of the substrate effects the ability of cancer cells to exert forces related to adherence [44] and to mechanical invasiveness [45]. Regarding cancer metastasis, some existing mathematical models can be found in the works [46–48].

The existence of the complexity and heterogeneity in various cancers poses a big challenge to adequate treatments. For many decades, many studies have been devoted to finding a breakthrough for cancer treatment. With the bound of ethics as well as the increasingly loud voice of anti-animal experiments, biological experiments and clinical trials need to be closely integrated with mathematics and high-speed development of computer technology. In this fast pace of life, more and more people are suffering from chronic or emerging diseases and a majority of cancers develop as a result of chronic inflammation [49]. Mathematical models provide an avenue to explore possible improved and alternative therapies against cancer [50]. For instance the works [51, 52] modeled radiotherapy of breast cancer and their work shows the possibility of investigating clinically verifiable hypotheses for the influence of radiotherapy on cancer progression through numerical simulation. Furthermore, Tanaka et al. [53] proposed a model for prostate cancer which is helpful to scrutinize the application of hormone therapy. Another modeling work, treating the influence of chemotherapy on cancer cells, was reported in [54]. Next to the traditional treatment approaches like surgery, chemotherapy, radiotherapy, cancer immunotherapy has shown some prospects [55, 56]. Therefore, the numerical simulation of immunotherapy has become a research direction. Through boosting the immune system of individuals to fight cancers, a model in terms of tumor-immune interaction was developed in [57]. A survey of several mathematical models and methods dealing with the tumor-immune interaction was provided in [58]. Moreover, any process of cancer progression could be a therapeutic target and several therapy-related models were introduced by Abbott and Michor [59]. Furthermore, smart healthcare has drawn a lot of attention, which is able to monitor a patient's vital organs and to guide doctors to perform surgery as well as to apply medications more accurately. However, smart healthcare is non-separable from computer technology with numerical simulation and it faces many mathematical challenges that need to be solved. Therefore, mathematical modeling is a promising means to reduce the cost and ethical burden of experimental tests for cancer research [50] and will even contribute to quantify the impact of therapies against cancer. This quantification will be used to improve and, even better, to optimize certain therapies by computing the impact of new therapies against cancer.

1.2.3. MATHEMATICAL MODELING FROM A VIEW OF IDENTIFIED CANCER TYPES

There are currently more than a hundred distinctly types of identified cancers [60]. According to the global cancer statistics given in [61], the cancer with the highest mortality rate, as high as 19.4% in adults, is lung cancer. Regarding the models on lung cancer, Chmielecki et al. [62] used an evolutionary model to optimize the dosing of drug treatment. Wang et al. [63] and Bianconi et al. [64] proposed further mathematical models to simulate lung cancer by multi-scale agent based and systems biology inspired formalisms for large tumors. Furthermore, other types of cancers were simulated mathematically like liver cancer [65], breast cancer [24, 51], brain cancer [66, 67], avascular cancer [68], prostate cancer [53, 69], etc. Some tumors develop in distinct architectural forms, e.g., preinvasive intraductal tumors in the breast or prostate, which were simulated by Rejniak and Dillon [70]. Pancreatic cancer is notorious for its profuse stroma with less than 4% 5-years survival rate [71], which was modeled in Chapter 2 and Chapter 3.

1.2.4. MATHEMATICAL MODELING FROM A VIEW OF MODEL TYPES

Modeling mechanics of cancer cells and tissue is an emerging field with a broad spectrum of patterns. Agent-based models are developed to understand the mutual interplay of an individual cell and its surroundings on the micro-scale. These models have a completely different nature compared to the macro-scale off-agent models. The macro-scale models consider cell densities rather than an individual cell, which have a merit is their applicability to larger physical. The agent-based models can be divided into several classes:

- Lattice-based models, which include cellular automata, lattice gas cellular automata and cellular Potts models, which are described in the review [72]. In cellular automata, cells may occupy a single lattice site, herewith one is able to simulate a large population of cells [73, 74]. In comparison, lattice gas cellular automata models include velocity channels next to their positions [75]. Furthermore, the cellular Potts models are characterized by energy functionals that determine the probability of a change of state at a lattice point. More information can be found in the works by Merks and Koolwijk [76], van Oers *et al.* [77] and the pioneering work by Glazier and Graner [78];

- Particle models are formalisms where each cell is treated as an individual particle with a fixed geometry (circles or spheres in the two- and three-dimensional cases), and where the cells are allowed to migrate throughout the region according to several chemical, mechanical or electrical signals. For an overview, we refer the interested reader to consult Vermolen [79], while for specific implementations, we refer to Kim *et al.* [80] and Ribeiro *et al.* [81] in the modeling of filopodia. In particular, Ribeiro *et al.* [81] report on how the filopodia contribute to cell migration. Furthermore, Drasdo and Hoehme [82], Byrne and Drasdo [83], Vermolen and Gefen [84, 85], and Vermolen *et al.* [30] elaborate on the context of the immune system to fight cancer;

- Cell-shape evolving models are representations where the geometry of the cell changes during its migration. This migration may result from various signals. Here one should mention the approach by Madzvamuse and George [86], which deals with the migration and movement of the cells with a visco-elastic inner cell structure, the model by Borau *et al.* [87], which is based on a voxel approach, as well as the approach by Vermolen and Gefen [19] which is based on a division of the cell surface into mesh points that are connected to each other and to the center of the cell. Vermolen *et al.* [88] extend the approach to a multicell and multi-physics environment to simulate the immune system;

- Hybrid discrete-continuum models, which are feasible models for large multicellular systems [72]. This class, based on treating cells as individual entities and other signals through continuum-scale approaches, is explained further in [89]. Furthermore, the hybrid approach has been used for simulation of would healing [90] and angiogenesis [91], etc.

1.3. OUTLINE

Due to the overwhelming complexity in cancer research, the joint-effort has to be accelerated. This thesis focuses on the mathematical modeling of pancreatic cancer with its treatment and uncertainty quantification. Albeit cancer differs even between patients, some underlying mechanisms are comparable and therefore we generalize the similarities and simulate the biophysical processes by using analogous mathematical frameworks and numerical methods.

This thesis is organized as follows. In Chapter 2, we set up a cell-based model with an application to pancreatic tumor islets, where the influence of the collagen orientation of desmoplastic stroma on T-lymphocytes migration is investigated. As expected, the tumor-associated desmoplastic stroma, acting as a physical barrier, inhibits anti-tumor responses and drug treatments so that cancer cells can survive and further proliferate at early stages. To investigate the desmoplastic stroma-targeted treatment, Chapter 3 introduces a model to mimic the pancreatic cancer progression under a combined drug intervention PEGPH20 + gemcitabine. With comparing the time of administration, the likelihood of cure is predicted using a Monte Carlo simulations framework. To compare different methods, an agent-based model cellular automata is introduced in Chapter 4, which is used to simulate a larger cell cluster level. We incorporate virotherapy in this study using a reaction-diffusion equation. As cancer progresses, partial cells will start to metastasis and undergo massive deformations. In Chapter 5, we develop a cell-based model for the evolution of cell morphology during cancer metastasis, where the likelihood of cancer cell metastasis is predicted based on Monte Carlo simulations. Finally, several conclusions as well as prospects are given in Chapter 6.

2

A MODEL FOR CELL MIGRATION IN NON-ISOTROPIC FIBRIN NETWORKS WITH AN APPLICATION TO PANCREATIC TUMRO ISLETS

Cell migration, known as an orchestrated movement of cells, is crucially important for wound healing, tumor growth, immune response as well as other biomedical processes. This chapter presents a cell-based model to describe cell migration in non-isotropic fibrin networks around pancreatic tumor islets. This migration is determined by the mechanical strain energy density as well as cytokines-driven chemotaxis. Cell displacement is modeled by solving a large system of ordinary stochastic differential equations where the stochastic parts result from a random walk. The stochastic differential equations are solved by the use of the classical Euler-Maruyama method. In this chapter, the influence of anisotropic stromal extracellular matrix in pancreatic tumor islets on T-lymphocytes migration in different immune systems are investigated. As a result, tumor peripheral stromal extracellular matrix impedes the immune response of T-lymphocytes through changing the direction of their migration.

The contents of this chapter have been published in paper [92]: Jiao Chen, Daphne Weihs and Fred Vermolen. "A model for cell migration in non-isotropic fibrin networks with an application to pancreatic tumor islets." Biomechanics and modeling in mechanobiology 17, no. 2 (2018): 367-386.

2.1. INTRODUCTION

Cell migration is a directed movement of cells which typically includes amoeboid and mesenchymal movement. Cell migration is driven by (combinations of) several mechanisms: chemical cues (chemotaxis or haptotaxis where the cues are in the fluid phase or extracellular matrix (ECM), respectively), mechanical cues (mechanotaxis, being tensotaxis or durotaxis), electrical cues (electrotaxis), by light activation and by random walk. Cell migration is an integral part of many different biomedical processes, such as wound healing, organ development, tumor growth and cancer metastasis. Moreover, it is critical in the framework of the immune system responses which are indispensable for clearing the body from hazardous chemicals, pathogens and mutated cells, such as cancer cells. Therefore understanding cell migration is crucially important for finding ways to improve therapies.

The immune response is essential for all living organisms. In antitumor immune responses, tumor-specific T-lymphocytes, in particular CD8$^+$, play an indispensable role. However, some cancer cells are able to escape the engulfment by T-lymphocytes through various mechanisms. One possibility could be that the tumors build stromal barriers against immune cells. Pancreatic ductal adenocarcinoma (PDAC) is known for its profuse desmoplastic stroma which is composed of activated fibroblasts, collagen and ECM [93]. The desmoplastic stroma plays an important role in the tumor progression, however its function is likely to be dynamic over time since its cellular and noncellular constituents change over time [94, 95]. In the literature, there is some controversy about whether stromal constituents support or inhibit tumor progression. Rhim *et al.* [93] demonstrate that at least some stromal constituents can act to physically restrain rather than promote tumor progression. Whereas, according to Salmon and Donnadieu [96], the stroma may support tumor progression by preventing the immune system from reaching and destroying the tumor. They observe that tumor islets (T-islets), which are surrounded by rich stromal networks, can form a major obstacle for T-lymphocytes mediated antitumor activities. Moreover, Hanahan and Weinberg [97] state that some stromal cells cause immune suppression and hence promote tumor survival and growth. Therefore the effects of the tumor microenvironment, and specifically the stroma, on tumor progression are still unclear. This could lay the foundation for the improvement of cancer therapy.

Much experimental work has been done on cancer and cancer cells. However, the tumor microenvironment and its immune mechanisms have only recently become an important focus, and thus the availability of experimental data and results are still limited. Therefore, there is an urgent need to strengthen multidisciplinary tumor research including input from medicine, biology, engineering and mathematics. Developing new insights into tumor behavior and response in connection with its environment as well as immune system interactions requires a strong link between available experimental results and the development of updated hypotheses. In order to facilitate this link and to be able to forecast tumor behavior under various experimental circumstances that lie beyond the currently available experimental results, a quantification of the hypotheses into mathematical relations is indispensable. Mathematical models can be developed on several scales ranging from continuum-based macro-models to cell-based micro-models. Since cell-based models often use measurable experiment-based quantities (like cell migration rates, etc.), they are very attractive though their implementation over large domains is possibly expensive. Since in this chapter, we are interested in the small spatial length scale of the order of millimeters, the model that we currently work with is cell-based.

This chapter focus on the simulation of cell migration in T-lymphocytes mediated antitumor response with an application to pancreatic tumors. The work by Salmon and Donnadieu [96] has shown that in many cases pancreatic carcinoma consists of T-islets which are surrounded by stromal regions where collagen is oriented parallel to the circumference of T-islets. Since T-lymphocytes migrate faster in the direction of the orientation of collagen fibers, T-lymphocytes merely circle around T-islets and thereby hardly enter them. Hence, T-lymphocytes are unable to function in neutralizing cancer cells. To be able to identify ways to change these circumstances, we have developed mathematical models that reproduce the experimental phenomenon as much as possible and allow to simply and rapidly develop and test hypotheses on the process mechanisms and predict experimental outcomes. Using simulations, we propose and evaluate a possible therapy, based on injecting or stimulating isolated endothelial cells that are not connected to the blood vessel network and letting them invade T-islets through the collagen network around them. The idea is to exploit endothelial cells ability to degrade the network such that T-lymphocytes are able to invade T-islets and be able to interact with and neutralize cancer cells. This idea has not been implemented as a therapy to fight cancer, however, our aim is to simulate this process to show its potential applicability.

In this chapter, we aim at a micro-scale phenomenological description that T-lymphocytes migrate in the vicinity of T-islets. We extend the formalism by Vermolen and Gefen [84] to non-isotropic fibrin networks where the formalism by Cumming *et al.* [98] will be used and extended such that we can model geometrically evolving cells in non-isotropic environments. Next to T-lymphocytes, we will take into account the migration, proliferation, apoptosis of all other cells as well as mutation of benign epithelial cells.

2.2. MATHEMATICAL MODEL

The model addresses several biological processes, which will allow simulation of the immune response to T-islets in different microenvironments. Specifically, we include the migration, division, apoptosis, mutation of cells, the chemical signaling as well as the immune reaction in a non-isotropic environment. In addition, contractile forces exerted by cells are accounted for by a simplified mechanical balance. To this extent, a domain of computation $\Omega \subset \mathbb{R}^2$ is introduced where $\Omega_\mathrm{T} \subset \Omega$ denotes T-islets. The islet Ω_T is surrounded by a stromal layer, which contains a high density fibrin network with orientation parallel to the circumference of Ω_T, this subdomain is denoted by $\Omega_\mathrm{F} \subset \Omega$ and it does not overlap with Ω_T.

To encode a mathematical model, the following procedures and assumptions are used in the development of present formalism: 1) to keep the computations short in CPU-time, we consider a 2D domain of computation; 2) all cells are hemispherical and the projection onto the 2D substrate is a circle; 3) each cell has two discrete states: viable or dead; 4) each viable epithelial cell exerts a traction force and is able to migrate or proliferate; 5) cells that collide repel each other by contact forces that they exert in the normal direction. In the following subsections, we provide the formalisms for each cell condition.

2.2.1. THE MIGRATION OF EPITHELIAL CELLS

Traction forces are crucial for adhesion and migration of cells and affect the intercellular communication and as well as for, among others, shape maintenance and mechanical signal generation, see experimental studies in [99, 100]. For the sake of completeness of the model described in this manuscript, we present the cell migration model that has been developed in [84]. The model formulation for cell migration is based on experimental observations by Reinhart-King *et al.* [100]. Firstly, we consider the distant communication of cells through traction force. Later, we will deal with the repulsive force that is induced by physical contact. Tensile forces are applied by cells to their microenvironment using the actomyosin machinery. Cells generate tensile forces internally as myosin motors induce lateral, relative motion of two actin filaments. An actin filament may connect to the microenvironment through trans-membrane integrins. The external part of the integrin may then connect to the substrate or ECM, thus transmitting the intracellular force [44]. Slight deformation of the substrate caused by stress gives strain energy U, which reads as:

$$U = \frac{1}{2} V \sigma \epsilon = \frac{1}{2} V E \epsilon^2 = \frac{1}{2} \frac{V}{E} \sigma^2, \tag{2.1}$$

where V denotes the deformation volume, σ denotes stress, ϵ denotes strain of the substrate at the center of cell and E is Young's modulus from Hooke's law, given by

$$E = \frac{\sigma}{\epsilon}. \tag{2.2}$$

We use M_i^0 to represent the strain energy density, that is the energy per unit of volume, which follows from the exertion force F_i at the position of cell i. Then the strain energy density is dictated by

$$M_i^0 = \frac{1}{2}\sigma\epsilon = \frac{1}{2}E_s(\mathbf{r}_i)\epsilon^2 = \frac{1}{2}\frac{\sigma^2}{E_s(\mathbf{r}_i)}, \quad \text{for } i \in \{1, ..., n\}, \tag{2.3}$$

where $E_s(\mathbf{r}_i)$ represents the local elastic modulus of the corresponding substrate. Furthermore, we neglect the compressibility of ECM. This is motivated by the experimentally observed Poisson ratio of 0.48 [44, 101]. The above relation is able to handle the non-uniformity of the substrate stiffness. Further, $\mathbf{r}_i$ denotes the position of cell i. If we use L and d for the thickness and vertical displacement of the deformed substrate, then ϵ is given by

$$\epsilon = \frac{d}{L}, \tag{2.4}$$

and hence the strain energy density can be calculated by

$$M_i^0 = \frac{1}{2}E_s(\mathbf{r}_i)(\frac{d}{L})^2, \quad \text{for } i \in \{1, ..., n\}. \tag{2.5}$$

Hooke's Law is used for a low strain by

$$\epsilon = \frac{1}{E_s(\mathbf{r}_i)}\frac{F_i}{\pi R^2}, \quad \text{for } i \in \{1, ..., n\}. \tag{2.6}$$

From the above equation and Hooke's Law, we get

$$M_i^0 = \frac{1}{2\pi^2}\frac{F_i^2}{E_s(\mathbf{r}_i)R^4}, \quad \text{for } i \in \{1, ..., n\}, \tag{2.7}$$

where R represents the cell radius. The finding by Merkel *et al.* [102] shows that the strain energy density decays exponentially approximately with the decay factor given by

$$\lambda_i = \frac{E_s(\mathbf{r_i})}{E_c}, \quad \text{for } i \in \{1, ..., n\}. \tag{2.8}$$

Here λ_i is used to represent the signal attenuation ratio of elasticity modulus of substrate $E_s(\mathbf{r}_i)$ and elasticity modulus of cell E_c. We calculate the strain energy density $M_i(\mathbf{r})$ due to the cell position $\mathbf{r}$ with center position $\mathbf{r}_i$ by

$$M_i(\mathbf{r}) = M_i^0 \exp\{-\lambda_i \frac{\parallel \mathbf{r} - \mathbf{r}_i \parallel}{R}\}, \quad \text{for } i \in \{1, ..., n\}. \tag{2.9}$$

As outlined in [84], the energy density is a scalar number, hence it can be summed to obtain a total strain energy density $M(\mathbf{r})$ due to all cells at position $\mathbf{r}$ as follows,

$$M(\mathbf{r}) = \sum_{j=1}^{n} M_j(\mathbf{r}) = \sum_{j=1}^{n} M_j^0 \exp\{-\lambda_j \frac{\| \mathbf{r} - \mathbf{r}_j \|}{R}\}, \quad \text{for } j \in \{1, ..., n\}. \tag{2.10}$$

Thence for cell i at time t, its own sensed mechanical stimulus $M(\mathbf{r}_i)$ is represented by

$$\begin{aligned} M(\mathbf{r}_i) &= \sum_{j=1}^{n} M_j^0 \exp\{-\lambda_j \frac{\| \mathbf{r}_i - \mathbf{r}_j \|}{R}\} \\ &= M_i^0 + \sum_{j=1_{j\neq i}}^{n} M_j^0 \exp\{-\lambda_j \frac{\| \mathbf{r}_i - \mathbf{r}_j \|}{R}\}, \quad \text{for } i, j \in \{1, ..., n\}. \end{aligned} \tag{2.11}$$

Where $\mathbf{r}_i$ and $\mathbf{r}_j$ denote the position of cell i and cell j, respectively. According to Vermolen and Gefen [84], the displacement direction of a cell is a linear combination of all the unit vectors between this cell i and others caused by their mechanical signals. For cell i and cell j, the unit vector is $\mathbf{e}_{ij} = \frac{\mathbf{r}_i - \mathbf{r}_j}{\|\mathbf{r}_i - \mathbf{r}_j\|}$, and the total displacement of cell i during a time step Δt is parallel to

$$\mathbf{z}_i = \sum_{j=1_{j\neq i}}^{n} M_j(\mathbf{r}_i(t))\mathbf{e}_{ij}, \quad \text{for} \quad i, j \in \{1, ..., n\}, \tag{2.12}$$

where $\mathbf{r}_i(t)$ is the cell i position at time t, and $\mathbf{z}_i$ is a vector to guide the direction of cell movement and hence the corresponding total unit vector is $\hat{\mathbf{z}}_i = \frac{\mathbf{z}_i}{\|\mathbf{z}_i\|}$. Taking the mechanical stimulus into consideration, total displacement over a time is calculated by

$$\mathrm{d}\mathbf{r}_i(t) = \alpha_i M(\mathbf{r}_i(t))\hat{\mathbf{z}}_i \mathrm{d}t, \quad \text{for } i \in \{1, ..., n\}, \tag{2.13}$$

where α_i is a parameter with dimension $[\frac{m^3}{Ns}]$ and the shear force is directed along the substrate, which acts perpendicularly to the exertion force. For viable cells, Gefen [103] achieves an expression for α_i

$$\alpha_i = \frac{\beta_i R^3}{\mu F_i}, \quad \text{for } i \in \{1, ..., n\}, \tag{2.14}$$

where β_i quantifies the mobility of the portion of the cell surface that is in physical contact with the substrate of a viable cell and μ is the cell-substrate friction coefficient, which equals 0.2 according to Gefen [103]. Viable cells move according to the mechanical stimulus that they sense, however they are also observed to move (partly) according to a random walk and hence the magnitude of movement should be revised to

$$\mathrm{d}\mathbf{r}_i(t) = \alpha_i M(\mathbf{r}_i(t))\hat{\mathbf{z}}_i dt + \sqrt{2D}\mathrm{d}\mathbf{W}(t), \quad \text{for } i \in \{1, ..., n\}, \tag{2.15}$$

where $d\mathbf{W}(t)$ is a vector-Wiener process and D is cell diffusivity.

Epithelial cells move under the influence of strain energy as well as a random walk in the circle islet. The detection threshold ε is introduced as a minimum strain energy signal for remote cells to detect each other. Therefore, the total signal strength a cell senses should satisfy

$$M_i(\mathbf{r}) = M_i^0 \exp\{-\lambda_i \frac{\| \mathbf{r} - \mathbf{r}_i \|}{R}\} \geq \varepsilon, \quad \text{for } i \in \{1, ..., n\}. \tag{2.16}$$

Reinhart-King *et al.* [100] find that the largest distance for a cell to detect is around $\hat{d} = 30$ μm with different elasticity moduli of substrate (approximately 5 kPa) and cell (approximately 0.5 kPa). This distance may depend on the phenotype of the cell [104]. Hence the threshold ε is defined by

$$\varepsilon = M_i^0 \exp\{-\lambda_i \frac{\hat{d}}{R}\} \approx 1.99 \times 10^{-54}, \quad \text{for } i \in \{1, ..., n\}. \tag{2.17}$$

Here $\varepsilon = 0$ kg$\cdot\mu$m/min^2 is used taking the rounding error of the computer into account. Once cells come into physical contact with each other, the force reacting against invagination pushes cells away from one another. This is treated in the next subsection.

2.2.2. THE REPULSION OF CONTACTING CELLS

Cells will not occupy the same space under normal circumstances. However, cells can have direct mechanical and physical contact with their neighbors, which is associated with shape changes in general. In this model, cells are allowed to migrate towards each other and to prevent them from occupying too much common space, a repulsive force is added to our model with cells that remain circular at all times.

Gefen [103] introduces a repulsive invagination force into the cell contact force, which is also incorporated in the computational framework. The elastically impinging cells will generate a repulsive force to repel each other, which is determined by the invagination distance and contact radius. This invagination force will translate to the concept of energy through the computation of the amount of work. This has been worked out in [84]. Then the strain energy density as a result of intercellular contact between cell i and cell j is given by

$$M^{ij} = \frac{4}{15\sqrt{2}} \frac{E_c}{\pi} (\frac{h}{R})^{\frac{5}{2}}, \quad \text{for } i, j \in \{1, ..., n\}, \tag{2.18}$$

where M^{ij} and h, respectively, denote the strain energy density produced by the elastic interaction and indentation distance between the two neighboring cells.

We calculate h by

$$h = \max(2R - \| \mathbf{r}_{ij} \|, 0), \quad \text{for } i, j \in \{1, ..., n\}, \tag{2.19}$$

where the $\mathbf{r}_{ij}$ represents the distance between cell i and cell j, and total strain energy density $\hat{M}_i$ between cell i and cell j by

$$\hat{M}_i = M(\mathbf{r}_i) - M^{ij}, \quad \text{for } i, j \in \{1, ..., n\}. \tag{2.20}$$

We phenomenologically assume that the repulsive motion is proportional to the strain energy density that the cell experiences. Note that this phenomenological treatment does not incorporate Newton's Law. Note that the migration of the cells contains two components. The first component follows from long-distance communication. The second component, which only sets in if $h > 0$, results from repulsive motion due to physical contact between the cells. Having two cells, this will imply that an equilibrium is reached if $\hat{M}_i = 0$. This results in an equilibrium distance between the positions of the cells. This also means that the cells mechanically touch over a certain area, and herewith one can phenomenologically consider this as a measure of cell-cell adhesion. In the case of multiple cells that are in mechanical contact, the M^{ij} term has to be summed over all the cells that are in mechanical contact with cell i. Imagine that cell i is in mechanical contact with cells $\{i_1, ..., i_k\} \subseteq \{1, ..., n\}$, then the above equation is written as,

$$\hat{M}_i(\mathbf{r}) = M(\mathbf{r}_i) - M_i^{mc}(\mathbf{r}_i), \quad \text{for } i \in \{1, ..., n\}, \tag{2.21}$$

where $M_i^{mc}(\mathbf{r}_i) = \sum_{j \in \{i_1, ..., i_k\}} M^{ij}$, which is the mechanical contact term of the strain energy density. Note that the repulsive forces can be balanced with attracting forces and hence the cells can partly overlap and be in physical contact. Therewith the model allows treatment of collective cell migration.

2.2.3. THE DIVISION, APOPTOSIS AND MUTATION OF CELLS

Each cell has a life cycle that affects its ability to migrate, and is characterized by the following stages: 1) G1, an increase of RNA and ribosome during this phase the cell does not move actively; 2) S, synthesis of DNA. Furthermore, the cell is mobile during this phase; 3) G2, synthesis of RNA and protein. During this phase, the cell volume increases and the cell is mobile; 4) M, cell mitosis and during this phase the cell does not move actively. We will incorporate this cell proliferation process in our simulation in the future. We model cell division, apoptosis as well as mutation fully using stochastic principles. Using the same principles given in [30] and [79], we assume that the probability of cell division, apoptosis or mutation obeys a simple memoryless exponential distribution and that it is only affected by the total strain energy density a cell endures, which is given by $f_{t_n}(\lambda, t)\Delta t$ during the interval $(t_n, t_n + \Delta t)$. Here λ ($\lambda > 0$) is the probability per unit of time (here per minute) of cell division, apoptosis or mutation after t_n, and $f_{t_n}(\lambda, t)$ is defined as,

$$f_{t_n}(\lambda, t) = \lambda \exp(-\lambda(t - t_n)), \tag{2.22}$$

and hence,

$$\begin{aligned} P(t \in (t_n, t_n + \Delta t)) &= \int_{t_n}^{t_n+\Delta t} f_{t_n}(\lambda, t)\, dt \\ &\simeq 1 - \exp(-\lambda \Delta t). \end{aligned} \tag{2.23}$$

Note that if $\lambda \Delta t \ll 1$, then

$$P(t \in (t_n, t_n + \Delta t)) = \lambda \Delta t + O(\lambda \Delta t)^2, \tag{2.24}$$

where O is Landau order-symbol to describe the limiting behavior of a function.

To realize it in the code, we let the system randomly generate a number $\xi \sim u[0, 1]$ taken from an uniform distributution. The cell, respectively, divides, dies or mutates if and only if

$$0 \leqslant \xi \leqslant 1 - \exp(-\lambda \Delta t), \tag{2.25}$$

where, as mentioned earlier, λ stands for the probability rate parameter for cell division, apoptosis or mutation.

In this model, cell proliferation, apoptosis as well as mutation happen under the premise of satisfying two kinds of conditions:

- Firstly, we simulate cell proliferation, apoptosis as well as mutation using the probability rates λ_d, λ_a and λ_m, respectively, which depend on the total strain energy density that the cell senses as a result of physical contact with its neighbors. We hypothesize that when a cell in a monolayer is in mechanical contact with six cells in 2D then it reaches a steady state. By Equation (2.21), we calculate the value of $\hat{M}_i(\mathbf{r}) = M(\mathbf{r}_i) - M_i^{mc}(\mathbf{r}_i)$ that corresponding with a cell being surrounded and just being in physical contact with six other cells such that the cell boundaries of each pair of cells coincide at one point has a value of approximately 0.0125 $\text{kg} \cdot \mu\text{m}/\text{min}^2$. We find that the equilibrium value of the strain energy density for one cell in contact with one other cell is approximately 0.03 $\text{kg} \cdot \mu\text{m}/\text{min}^2$ (see Figure 2.2). Herewith, we assume that one epithelial cell has sufficient space to divide if $\| \hat{M}_i(\mathbf{r}) \| < 0.03\ \text{kg} \cdot \mu\text{m}/\text{min}^2$ and in the same way, a cancer cell can divide if $\| \hat{M}_i(\mathbf{r}) \| < 0.04\ \text{kg} \cdot \mu\text{m}/\text{min}^2$. Furthermore, a cell is able to mutate or die with a bigger $\parallel \hat{M}_i(\mathbf{r}) \parallel$ if it is squeezed by other surrounding cells. Followed by a preliminary study of parameters, we set,

$$\lambda_d = \begin{cases} 10\ \text{min}^{-1}, & \text{if} \parallel \hat{M}_i(\mathbf{r}) \parallel < 0.03 \quad \frac{\text{kg}\cdot\mu\text{m}}{\text{min}^2} \\ 0\ \text{min}^{-1}, & \text{if} \parallel \hat{M}_i(\mathbf{r}) \parallel \geqslant 0.03 \quad \frac{\text{kg}\cdot\mu\text{m}}{\text{min}^2} \\ & \text{for epithelial cells} \end{cases}$$

$$\lambda_d = \begin{cases} 10\ \text{min}^{-1}, & \text{if} \parallel \hat{M}_i(\mathbf{r}) \parallel < 0.04 \quad \frac{\text{kg}\cdot\mu\text{m}}{\text{min}^2} \\ 0\ \text{min}^{-1}, & \text{if} \parallel \hat{M}_i(\mathbf{r}) \parallel \geqslant 0.04 \quad \frac{\text{kg}\cdot\mu\text{m}}{\text{min}^2} \\ & \text{for cancer cells} \end{cases}$$

$$\lambda_a = \begin{cases} 10\ \text{min}^{-1}, & \text{if} \parallel \hat{M}_i(\mathbf{r}) \parallel \geqslant 0.1 \quad \frac{\text{kg}\cdot\mu\text{m}}{\text{min}^2} \\ 0\ \text{min}^{-1}, & \text{if} \parallel \hat{M}_i(\mathbf{r}) \parallel < 0.1 \quad \frac{\text{kg}\cdot\mu\text{m}}{\text{min}^2} \\ & \text{for epithelial cells} \end{cases}$$

$$\lambda_m = \begin{cases} 10\ \text{min}^{-1}, & \text{if} \parallel \hat{M}_i(\mathbf{r}) \parallel \geqslant 0.05 \quad \frac{\text{kg}\cdot\mu\text{m}}{\text{min}^2} \\ 0\ \text{min}^{-1}, & \text{if}s \parallel \hat{M}_i(\mathbf{r}) \parallel < 0.05 \quad \frac{\text{kg}\cdot\mu\text{m}}{\text{min}^2} \\ & \text{for epithelial cells} \end{cases} \tag{2.26}$$

Here the corresponding probability is around 0.6321 by Equation (2.23) within a time interval of $\Delta t = 0.1$ min if the probability rate is 10 min^{-1}.

- Secondly, we assume that there is a period of time, in which a new cell grows. The length of this period is referred to as the growth time. After growth, the cell is able to
    - divide, if its growth time τ_d exceeds 5 minutes, that is $\tau_d \geq 5$ min;
    - mutate, if its growth time τ_m exceeds 10 minutes, $\tau_m \geq 10$ min;
    - apoptosis, if its growth time τ_a exceeds 10 minutes, $\tau_a \geq 10$ min.

Cells are allowed to slightly overlap other cells obtaining a repelling force and then repel each other and move away. Moreover, the repelling force increases significantly as the overlap distance goes up. In other words, cell contact inhibition impedes the cell division probability rate. This is also demonstrated by Nelson and Chen [105] and Chen *et al.* [106] who show that inhibition of cell division follows the reduction in cell area by mechanical constraint. To make the problem tractable, we only consider the change in mitotic probability rate rather than the change of cell area. The λ_d equals 10 min^{-1} after a time interval $\tau_d = 5$ min and drops from 10 min^{-1} to 0 min^{-1} if the mechanical force is sufficiently large which is $\parallel \hat{M}_i(\mathbf{r}) \parallel \geqslant 0.03\ \mathrm{kg}\cdot\mu\mathrm{m}/\mathrm{min}^2$. Malumbres and Barbacid [107] report that tumor cells have a proliferative advantage due to increased mitogenic signaling and/or the lower threshold required for cell-cycle commitment. Therefore, the threshold of strain energy density for λ_d of cancer cells is slightly changed to $0.04\ \mathrm{kg}\cdot\mu\mathrm{m}/\mathrm{min}^2$ based on the findings by Malumbres and Barbacid [107]. One cell can divide into two cells and the daughter cell moves away from the mother cell gradually because of the invagination force, to reach an equilibrium state for their separation distance. Moreover, normal cells exhibit aging, with a limited maximum time of division; such as a human somatic cell can divide approximately 50 to 100 times in culture [108]. In contrast, most cancer cells do not possess a maximum number of division times, which leads to 'immortal' cells with 'infinite' division chains.

Many epithelial cells are subject to cell-substrate contact-dependent proliferation and a loss of cell-substrate contact is able to trigger a kind of selective programmed cell apoptosis, called *anoikis* [109–112]. In the 2D simulation, we impose that the epithelial cell starts to die with the probability rate of $\lambda_a = 10$ min^{-1} when it senses the value of contact force $\parallel \hat{M}_i(\mathbf{r}) \parallel \geqslant 0.1\ \mathrm{kg}\cdot\mu\mathrm{m}/\mathrm{min}^2$ after a growth period of $\tau_a = 10$ min. In this case, one epithelial cell has been surrounded by more than one layer of six cells in a large cell density over a considerable interval of time. For cancer cells, Delarue *et al.* [113] find that compressive stress could decrease the division of carcinoma cells rather than increase apoptosis. Therefore, cancer cells are assumed to die as a result of engulfment by T-lymphocytes instead of mechanical stimuli.

We also consider the condition where at times an error occurs in the copying of the genes during cell division and a mutation is formed. In that case, a gene has been damaged, lost or copied twice. The changes in genes could be a result of one or more reasons from physical, chemical or biological factors that are mentioned in the introduction. According to [114], many developmental genes of embryo cells are regulated by mechanical force. Kumar and Weaver [115] report that the balance of mechanical forces, which originate from neighboring cells or the ECM, can regulate a surprisingly wide range of cellular properties that are all critical to tumorigenesis, including structure, motility, proliferation and differentiation. For the principles of how the cell senses mechanical signals and convert them into changes in cellular biochemistry, one can refer to [116] which unites cellular mechanotransduction with oncogenic signaling. Regarding breast cancer research in the work by Paszek and Weaver [117], tensional force plays a potentially important role in mammary gland development and tumorigenesis. On a molecular level, compression stress is able to alter the behavior of normal cells by influencing the impact of some chemokines. Furthermore, compression stress is able to alter the behavior of transformed mammary epithelial cells by changing gene and protein expression. Hence the mechanical signal implicitly influences the mutation rate of epithelial cells to cancer cells. Since the mechanical signals are dealt with using the strain energy density, we hypothesize that the cell mutation with the probability rate of $\lambda_m = 10\ \text{min}^{-1}$ is only affected by a large strain energy density, hence cells are allowed to mutate to cancer cells if $\parallel \hat{M}_i(\mathbf{r}) \parallel \geqslant 0.05\ \text{kg} \cdot \mu\text{m}/\text{min}^2$ after the time interval $\tau_m = 10$ min.

2.2.4. THE MIGRATION OF T-LYMPHOCYTES IN THE NON-ISOTROPY COLLAGEN NETWORK

In this study, the formalism by Cumming *et al.* [98] is used to describe the structure of the collagen and fibrin. To this extent, an orientation tensor $\Psi(t,\mathbf{x})$ is introduced, where t and $\mathbf{x}$, respectively, denote time and position in space. In the 2D setting, the entries of the symmetric tensor Ψ are arranged by its spectral decomposition:

$$\Psi(t,\mathbf{x}) = \begin{pmatrix} \Psi_{xx} & \Psi_{xy} \\ \Psi_{xy} & \Psi_{yy} \end{pmatrix}. \tag{2.27}$$

Stroma prevents T-lymphocytes and drug delivery entering T-islets, which causes their migration around the islets oriented parallel to the stromal ECM. On the other hand, the movement of T-lymphocytes is also affected by the concentration of chemokines [96]. Therefore, we suppose that T-lymphocytes are able to enter the islets eventually with a high concentration of a chemokine secreted by cancer cells. The orientation tensor is composed as the sum of its orthogonal and tangential products, which are coming from the chemokine and stromal components part, respectively. Thus the orientation tensor Ψ can be represented by

$$\Psi = \lambda_1 \mathbf{w_1} \mathbf{w_1}^T + \lambda_2 \mathbf{w_2} \mathbf{w_2}^T, \tag{2.28}$$

where the eigenvalues λ_1 and λ_2 represent the corresponding weights and the eigenvectors $\mathbf{w_1}$ and $\mathbf{w_2}$ are orthogonal and tangential components.

The research from Bougherara *et al.* [118] reveals that the density and orientation of collagen fibers control the distribution and migration of T-lymphocytes as well as their ability to infiltrate T-islets. Furthermore, their experiments illustrate that CD8$^+$ T-lymphocytes migrate faster in a loose-collagen area and reduce its velocity once encountering an obstacle with densely distributed collagen fibers. At present, we assume that the tumor peripheral collagen fibrin has a uniform density and introduce a constant k that represents a measure for the amount that anisotropy contributed to migration which is also a fixed attenuation faction for the orthogonal velocity of a cell, which reads as

$$\frac{\partial v}{\partial s} = -kv, \tag{2.29}$$

where s is the penetration depth with respect to outer peripheral region and v is given by

$$v = v^0 e^{-ks}, \tag{2.30}$$

here v^0 denotes the instantaneous velocity at which cells enter the outer boundary. This approach is in line with the formalism by Cumming *et al.* [98]. Therefore, the orientation tensor Ψ is improved slightly to,

$$\Psi = v^0 e^{-ks} \lambda_1 \mathbf{w_1} \mathbf{w_1}^T + v^0 \lambda_2 \mathbf{w_2} \mathbf{w_2}^T. \tag{2.31}$$

The k value is investigated in relation to the different density gradient of collagen and fiber in the computational framework. As the density gradient gets higher, the faster the radial velocity decays. The real ‘peritumoral zone’ contains a complicated mixture of neoplastic cells and tumor stroma which distribute in irregular strands or septa [119]. In this case, the density of fibers is not uniform where the Wiener process should be taken into the account.

2.2.5. CHEMOKINE MODEL

Chemokines are a class of cytokines that guide cells through chemotactic movement. They are involved in many physiological and pathological processes through combining with their corresponding receptors in cells, such as cell growth, differentiation, tumor progression and immune activities, etc.

Tumors have been observed to produce a variety of chemokines and the tumor-derived chemokines make an attractive target for tumor-reactive T-lymphocytes to fight against them [120, 121]. Colombo and Trinchieri [122] report that chemokine interleulin-12 (IL-12) acts on T-lymphocytes and NK-cells in anti-tumor immunity and immunotherapy. Furthermore, Kershaw *et al.* [121] verify their hypothesis that T-lymphocytes with receptor CXCR2 move towards a source of tumor-derived chemokine, Gro-α. Therefore, it is assumed that only one kind of chemokine, which is a cytokine secreted by cancer cells, is able to attract T-lymphocytes to move towards cancer cells. As the number of cancer cells increases, T-lymphocytes migrate in the direction of the gradient of the chemokine. The reaction-diffusion Equation (2.32) is used to describe the rate of change in the concentration of the chemokine as follows,

$$\frac{\partial c}{\partial t} - D_c \nabla c = \sum_{j \in \mathbb{K}(t)} \gamma_j(t) \delta(\mathbf{r} - \mathbf{r}_j(t)), \quad j \in \mathbb{K}(t), \tag{2.32}$$

where c and D_c represent the concentration and diffusion coefficient of chemokine. The $\delta(\mathbf{r})$ is Dirac Delta function for each cancer cell j at time t and $\gamma_j(t)$ is the corresponding chemokine secretion rate by cancer cells. Furthermore, $\mathbb{K}(t)$ denotes the set of active cancer cells at time t. By solving the steady-state counterpart of the partial differential equation, we get,

$$c(\mathbf{r}) = -\sum_{j\in\mathbb{K}(t)} \frac{\gamma_j(t)}{2\pi D_c} \log \| \mathbf{r} - \mathbf{r}_j(t) \|, \quad \text{if} \| \mathbf{r} - \mathbf{r}_j(t) \| \leq 1, \quad j \in \mathbb{K}(t). \tag{2.33}$$

This expression is used to model chemotaxis of T-lymphocytes towards cancer cells. Note that we only use the gradient of the above expression and that the relation is only phenomenological. Using a full time-dependent solution of Equation (2.32) requires the storage of positions at all times. This makes the scheme expensive.

2.2.6. THE MIGRATION OF T-LYMPHOCYTES

We describe the migration of epithelial and cancer cells based on the traction force as well as on random walk. T-lymphocyte cells migrate according to the gradient of the concentration of chemokines [96] and collagen orientation [118] instead of according to traction force. Here the displacement of T-lymphocytes is expressed by

$$\mathrm{d}\mathbf{r}_j(t) = \Psi[\beta\nabla c(t, \mathbf{r}_j(t))\mathrm{d}t + \sqrt{2D}\mathrm{d}\mathbf{W}(t)] - \sum_{l\in\{j_1,\ldots,j_k\}} M^{jl}\mathrm{d}t, \quad j \in \mathbb{T}(t), \tag{2.34}$$

where, the set $\{j_1, \ldots, j_k\}$ defines the set of cells that are in mechanical contact with cell j. Once again, $\mathrm{d}\mathbf{W}(\mathbf{t})$ is a vector-Wiener process and β and D, respectively, represent the chemotactic constant and diffusivity of the T-lymphocytes. The set of T-lymphocytes is represented by $\mathbb{T}(t)$.

Similarly, T-lymphocytes are not allowed to overlap too much under cell repulsive force described by the second part in Equation (2.34), which describes the contribution to T-lymphocytes migration as a result of invagination.

For an overview of the cross-talk among epithelial cells, cancer cells and immune cells in the microenvironment of pancreatic T-islets, a pictorial diagram is presented in Figure 2.1 which also includes the mathematical variables and the direction of the mathematical relations.

2.3. NUMERICAL METHOD

2.3.1. EPITHELIAL AND CANCER CELLS

If cells just come into mechanical contact, then the higher-order derivatives of strain energy density with respect to the intercellular distance are subject to a discontinuity. Therefore we use the Euler-Maruyama method for time integration, which is a generalization of the ordinary Forward Euler method for initial value problems to stochastic differential equations. Higher-order methods for

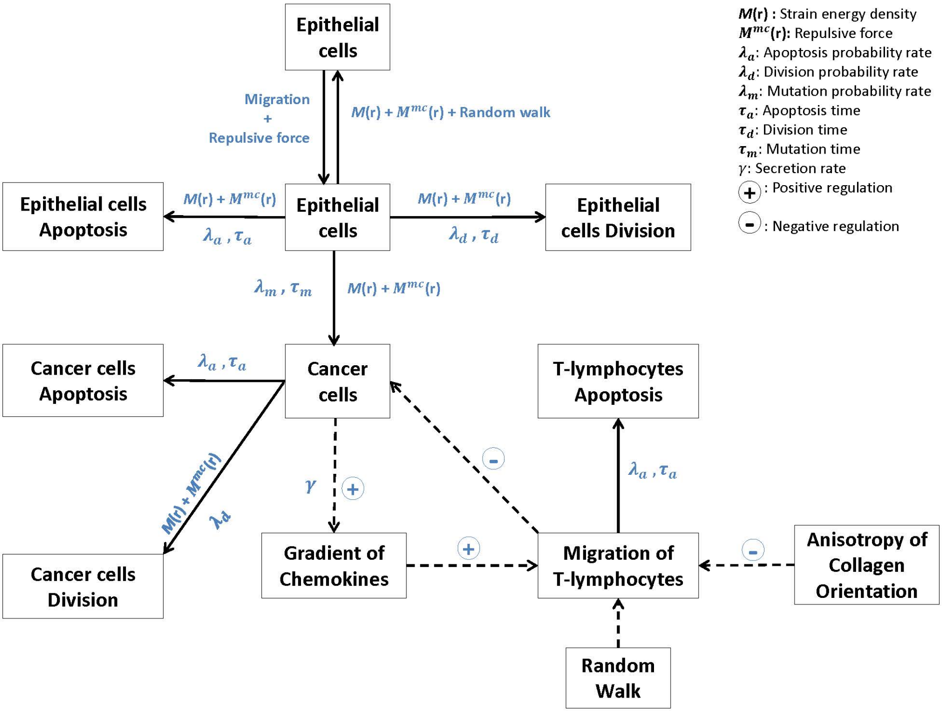

Figure 2.1: Schematic representation of the cross-talk among epithelial cells, cancer cells and immune cells in the microenvironment of pancreatic T-islets. The solid arrows represent the influence of a cell phenotype, where the corresponding mathematical variables have been indicated. Dotted arrows indicate positive or negative regulations.

the time-integration do not seem to improve the accuracy because of the dependence between M_{ij} and h. We evaluate the nonlinear parts at the previous time step. In this way, we circumvent the need for solving a nonlinear problem at each time step. Of course, this will induce some numerical stability criteria so that the time step cannot be chosen arbitrarily large to avoid numerical instability. The differential equation of the displacement is generally given by

$$\mathrm{d}\mathbf{r}_i(t) = \alpha_i \hat{M}_i(\mathbf{r})\hat{\mathbf{z}}_i \mathrm{d}t + \sqrt{2D}\mathrm{d}\mathbf{W}(\mathbf{t}), \quad i \in \mathbb{W}(t), \tag{2.35}$$

where α_i denotes the rate parameter mentioned in the model section, D denotes the cell diffusion coefficient and the random variable $\mathrm{d}\mathbf{W}(\mathbf{t})$ denotes a vector-Wiener process whose entries are identically distributed normal random variables with variance $\mathrm{d}t$ and expected value zero. Further, $\mathbb{W}(t)$ represents the set of epithelial cells and cancer cells. Therefore the actual position of cell i at time t

can be obtained from,

$$\mathbf{r}_i^t = \mathbf{r}_i^{t-1} + \Delta t \alpha_i \hat{M}_i(\mathbf{r}^t) + \sqrt{2D}\Delta\mathbf{W}. \tag{2.36}$$

Here $\Delta\mathbf{W}$ represents a 2D vector with independent stochastic variables from a normal distribution with zero mean and variance Δt.

Since the cells may collide into one another, they should not overlap each other totally. Therefore, we require their displacement to be less than one-fourth of their diameter. This criterion is quantified by

$$\| \mathbf{r}_i^t - \mathbf{r}_i^{t-1} \| = \max \| \mathbf{v}_i \| \Delta t \leq \frac{R}{2}, \tag{2.37}$$

where R is the radius of epithelial or cancer cells and $\mathbf{v}_i$ is the equilibrium velocity of cell i. From Equation (2.37), the time step is determined by

$$\Delta t = \min(0.1, \frac{R}{2\max \| \mathbf{v}_i \|}), \tag{2.38}$$

here we use a default value 0.1 min for the time step. Whereas, if the migration speed of the cells is large, then the time step is adjusted to $\Delta t = \frac{R}{2\max\|\mathbf{v}_i\|}$. This limitation of the time step guarantees that the cells do not move too much over a time interval and do not entirely coincide with each other. Furthermore, numerical experiments indicate that numerical stability is also guaranteed if the above criterion in Equation (2.38) is satisfied. This issue deserves some further numerical consideration in mathematical rigor.

2.3.2. T-LYMPHOCYTES

We use the same Euler-Maruyama method for T-lymphocytes migration. The displacement of T-lymphocytes is chemotaxis and we also incorporate the random walk to form stochastic differential equations. With the explained parameters in the former section, we calculate the actual positon of T-lymphocytes j at time t by

$$\mathbf{r}_j^t = \mathbf{r}_j^{t-1} + \Psi[\nabla c(t, \mathbf{x}_j^{t-1})\Delta t + \sqrt{2D}\Delta\mathbf{W}] - \sum_{l \in \{l_1, \ldots, l_k\}} M^{jl}\Delta t \quad j \in \mathbb{T}(t), \tag{2.39}$$

here the M^{jl} represents repulsive force between T-lymphocytes j and a cancer cell l.

With cell contact inhibition, T-lymphocytes will be bounced once they collide with each other. Therefore we suppose that the fourth of their diameter is the maximum overlapping distance. We use the same criterion in Equation (2.38). Furthermore, the same method is used to deal with the collision of T-lymphocytes

Table 2.1: Parameter values

Parameter	Meaning	Value and unit	Source
R	Radius of cells	2.5 μm	[25]
R_t	Radius of T-lymphocytes	2 μm	[25]
F	Cell traction force	$(10 - 25)\cdot 10^2$ kg $\cdot$ μm/min^2	[123, 124]
E_s	Substrate elasticity	$5\cdot 10^{-5}$ kg/(μm $\cdot$ min^2)	[25]
E_c	Cell elasticity	$0.5\cdot 10^{-5}$ kg/(μm $\cdot$ min^2)	[25]
β	Cell mobility coefficient	1 min^{-1}	[84]
μ	Friction coefficient	0.2	[25]
D	Cell diffusivity	0.005 μm/min	-
D_c	Chemokine diffusivity	0.001 μm/min	-
γ	Secretion rate of chemokine	10 min^{-1}	-

and epithelial as well as cancer cells. Since T-lymphocytes are smaller than the other cells, we suppose that the maximum overlapping distance of them depends on the radius of T-lymphocytes.

2.4. NUMERICAL SIMULATIONS

2.4.1. PARAMETER VALUES

To mimic tumor initiation and T-lymphocytes mediated immune response in pancreatic T-islets as well as possible, we chose the parameter values based on available sources in literature as much as possible. For those cases where literature values are not readily available, we make educational guesses based on the expected behavior. Table 2.1 lists all parameters values.

2.4.2. RESULTS

For the 2D simulation, the projection of each cell is defined as a circle on the substrate and a large circular domain with a radius of 35 μm is used to simulate T-islets. Regarding cancerous mutation, in the simulations, we highlight the mutation by a change of color from blue to red in the figures. In order to predict the impact of the non-isotropic fibrin network in different immune responses mediated by T-lymphocytes, we simulate T-islets under different conditions for immunity with stromal ECM orientation and without stromal ECM orientation.

First of all, we investigate the changes in strain energy density as well as mechanical contact force in different situations with respect to the overlap distance in Figure 2.2. The result in Figure 2.2(a) shows that the equilibrium overlap distance coming from strain energy density and mechanical repulsive force for two

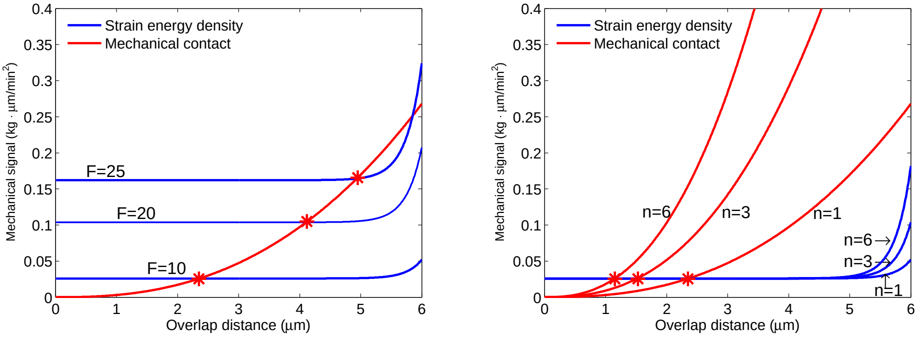

(a) (b)

Figure 2.2: The red and blue lines represent mechanical contact force and strain energy density, respectively. (a) compares the strain energy density with different cell traction force F values. (b) compares the mechanical contact force and strain energy density of one cell when it is surrounded by other one, three and six cells, respectively, for $F = 10$ kg$\cdot\mu$m/min^2.

cells increases as the F value arises and the best reasonable choice for F is 10 kg$\cdot\mu$m/min^2 considering the cell radius. Moreover, in Figure 2.2(b), the curves of mechanical contact force vary a lot when one cell is surrounded by another one, three and six cells and the maximum equilibrium overlap distance is approximately 2.35 μm when one cell is contacted by another one. This amount of overlap is deemed acceptable.

T-ISLETS WITHOUT STROMAL ECM ORIENTATION

Firstly, we consider the simulation of T-islets without any anisotropic collagen orientation, which means $k = 0$ in Equation (2.31), hence the migration of T-lymphocytes is determined by the concentration gradient of chemokine.

With a large mechanical stimulus, an epithelial cell mutates to a tumor cell in Figure 2.3(b) and it starts to divide subsequently. Since the tumor cells release a chemokine, T-lymphocytes move to the islet from different directions according to the chemokine signal. Cancer cells may be engulfed by T-lymphocytes when they are in contact for some time, concurrently T-lymphocytes also have a certain probability of death. In this model, T-lymphocytes and epithelial cells are not allowed to physically overlap as a result of mechanical interaction. Here, we simulate two kinds of results with different immune responses as follows: 1) Figure 2.3 shows T-islets with a strong immune response in which T-lymphocytes win eventually; 2) Figure 2.4 describes T-islets with a weak immune response so that the tumor colony occupies the entire region in the course of time. Note that

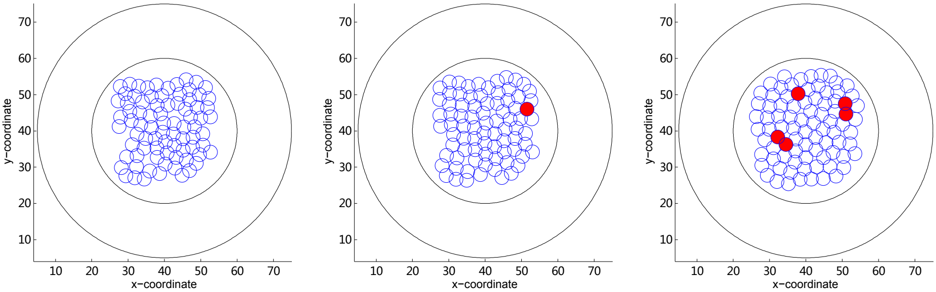

(a) t = 0 min (b) t = 10 min (c) t = 60 min

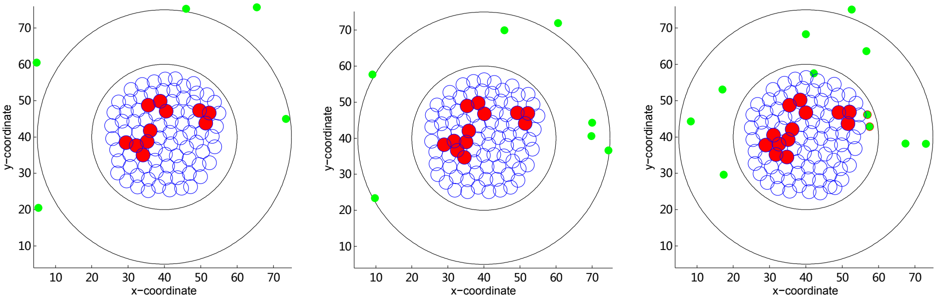

(d) t = 120 min (e) t = 150 min (f) t = 180 min

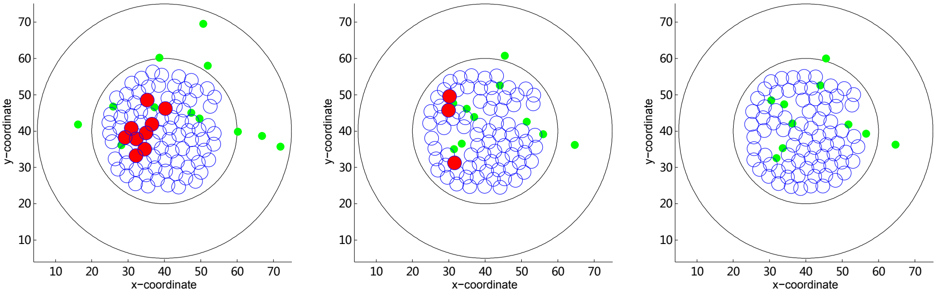

(g) t = 200 min (h) t = 300 min (i) t = 400 min

Figure 2.3: Snapshots of T-islets without anisotropic collagen orientation ($k = 0$) under a strong immune reaction. The blue, red and green circles denote the epithelial, cancer and T-lymphocytes, respectively.

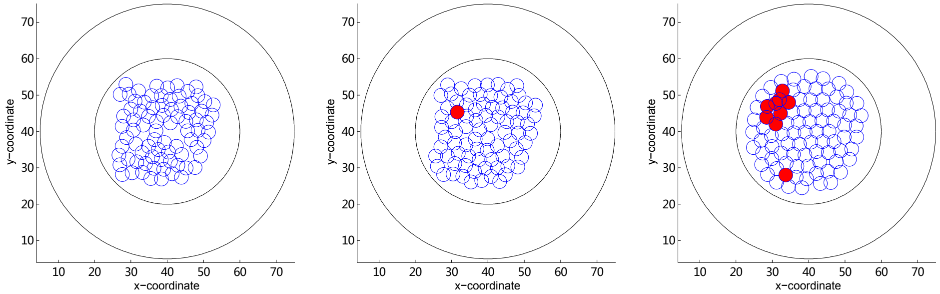

(a) t = 0 min (b) t = 10 min (c) t = 60 min

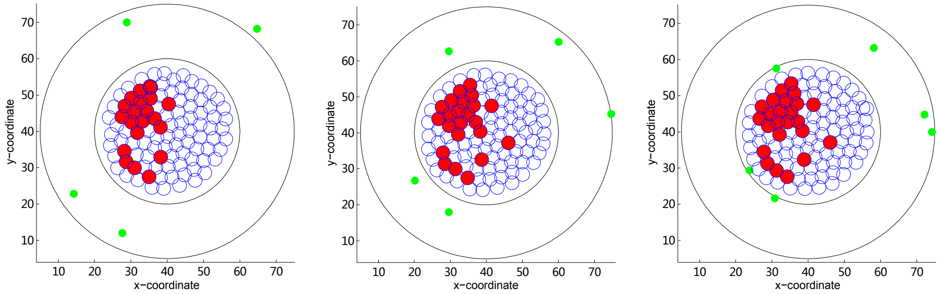

(d) t = 120 min (e) t = 150 min (f) t = 180 min

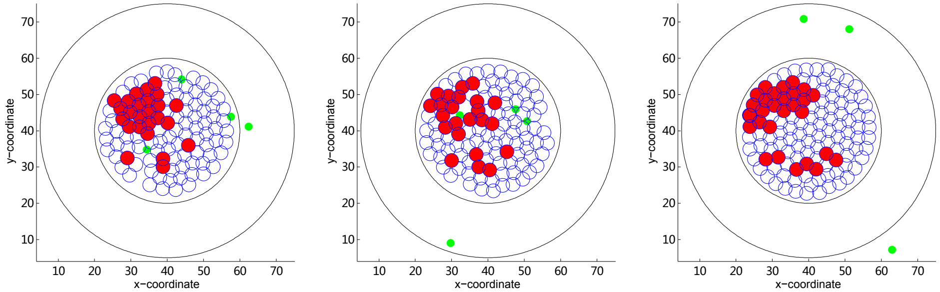

(g) t = 200 min (h) t = 300 min (i) t = 400 min

Figure 2.4: Snapshots of T-islets without anisotropic collagen orientation ($k = 0$) under a weak immune reaction. The blue, red and green circles denote the epithelial, cancer and T-lymphocytes, respectively.

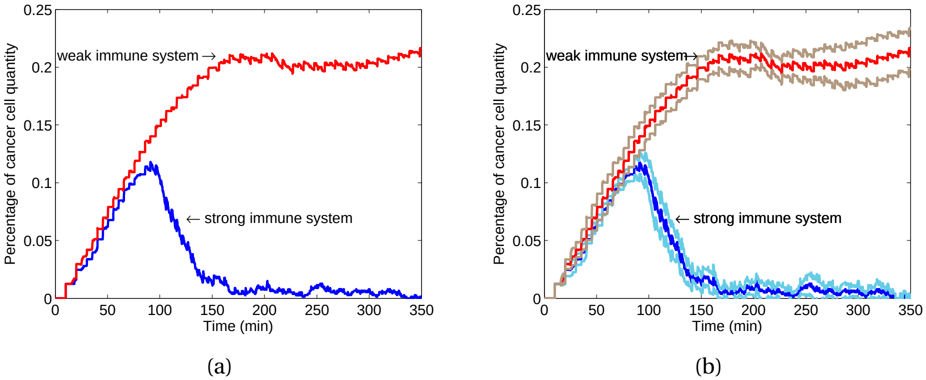

(a)

(b)

Figure 2.5: Comparison for change of the percentage of cancer cells in total cells in two situations. The red and blue lines represent the evolution of the percentage of cancer cells in a weak immune system and a strong immune system, respectively (see (a)). Furthermore, the corresponding confidence intervals are showed in (b). The brown and light blue lines denote the confidence intervals of a weak immune system as well as a strong immune system in T-islets without anisotropic collagen orientation ($k = 0$), respectively.

for the differences between strong and weak immune systems, we describe the strong and weak immune systems as follows

- $N_s = 2N_w$, here N_s and N_w denote the number of T-lymphocytes in the strong immune system and weak immune system, respectively.
- T-lymphocytes have a probability rate $\lambda_d = 10$ to die if the distance between T-lymphocytes and cancerous cell satisfies $\| \mathbf{r}_t - \mathbf{r}_c \| \leq 2.5$ μm over a time interval $\tau = 10$ min in weak immune system. Whereas, death of T-lymphocytes with the same probability rate $\lambda_d = 10$ sets in if $\| \mathbf{r}_t - \mathbf{r}_c \| \leq 3.5$ μm over a time interval $\tau = 5$ min in the strong immune system.

Figure 2.5 compares the evolution of the percentage of the cancer cells in total cells as a function of time in two situations. The number percent of cancer cells accounts for a large advantage in a weak immune system compared with the strong immune system. In order to find a confidence interval with 95% confidence level, a sample for 10 runs has been chosen and results are shown in Figure 2.5. Figure 2.5(a) describes the average results and Figure 2.5(b) shows the average results with corresponding confidence intervals. The weak immune system fails to control the cancer cells although a small reduction appears around $\tau = 250$ min.

T-ISLETS WITH STROMAL ECM ORIENTATION

Subsequently, we incorporate the anisotropic collagen orientation into this model and the 15 μm thick annular grey region visualizes the ECM with rich fibers of collagen and myofibroblasts. The function contribution of the desmoplastic stroma is unknown and controversial, however, it is reported to have a suppressive role for the immune response [93, 96]. Herein we model this phenomenon in order to provide some ideas for further research.

With the same parameters, epithelial cells are allowed to mutate to cancer cells (Figure 2.6(b)), which can arouse the immune T-lymphocytes chemotaxis (Figure 2.6(d)). After T-lymphocytes enter into the stroma, they sense the local orientation as well as chemokine signal and move to the place where normally gathered many cancer cells, see Figure 2.6(e). The reason why T-lymphocytes move along the collagen is because the anisotropic fibers are positioned parallel to the T-islets boundary. Normally tissue has isotropic fibers which have a ‘basket weave’ pattern with a fairly random orientation, whereas this stromal layer is described with more aligned collagen fibers. By experiment observation, Bougherara *et al.* [118] report that T-lymphocytes follow precisely the pre-defined collagen scaffold and move between two fibers. Furthermore, compared with the dense region, the loose-collagen areas have more CD8$^+$ T-lymphocytes. Therefore, T-lymphocytes migration is guided by collagen orientation and affected by collagen density, however, here we suppose T-lymphocytes suffer some impediment in parallel collagen fibers with uniform density and get through the barrier eventually with the increase of the number of cancer cells.

In this part, we also simulate two kinds of results. T-lymphocytes eliminate cancer cells and reach a dynamic equilibrium with a strong immune reaction in Figure 2.6 while cancer cells proliferate out of control in a weak immune system in Figure 2.7.

Similarly, the percentage of cancer cells quantity in both situations is compared over time in Figure 2.8 by using average data coming from a sample of 10 runs with 95% confidence level. This amounts to running ten simulations where the parameters are taken randomly using the normal distribution. The 95% interval of confidence is subsequently computed via $(\overline{x} - 1.96 \times \frac{\sigma}{\sqrt{n}}, \overline{x} + 1.96 \times \frac{\sigma}{\sqrt{n}})$. After a while, the fraction number of cancer cells is apparently bigger in a weak immune system. Furthermore, we compare the time responses with corresponding 95% confidence intervals in both strong immune system with collagen and without collagen (see Figure 2.9(b)). The figure shows that the anisotropic collagen contributes a lot with $k > 0$ for migration of T-lymphocytes in the blue line, which describes the strong immune response. Therefore, T-lymphocytes need more time t_2 to get the cancer cells in T-islets with collagen, and the corresponding number of cancer cells reaches a higher level. Therefore, stromal collagen

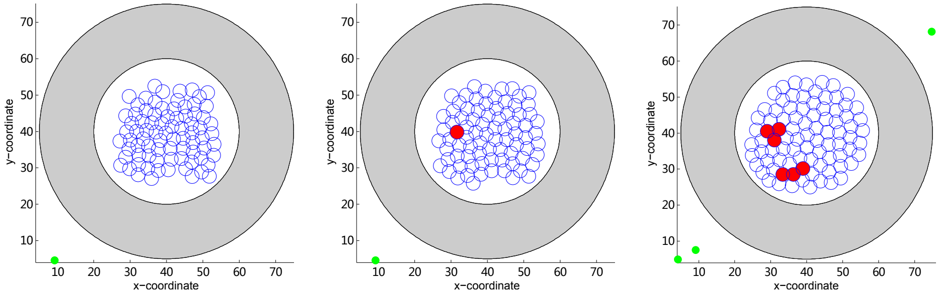

(a) t = 0 min (b) t = 10 min (c) t = 60 min

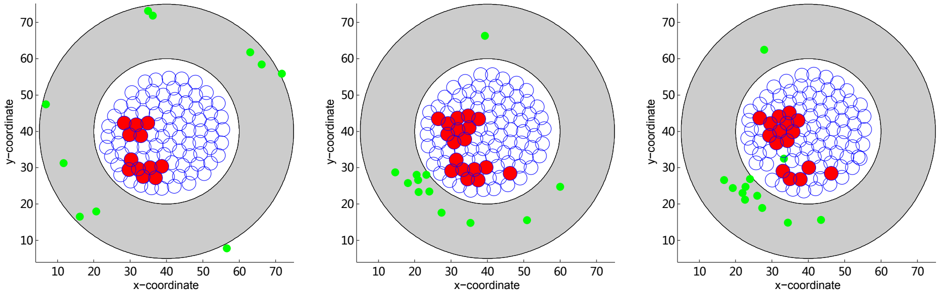

(d) t = 120 min (e) t = 150 min (f) t = 180 min

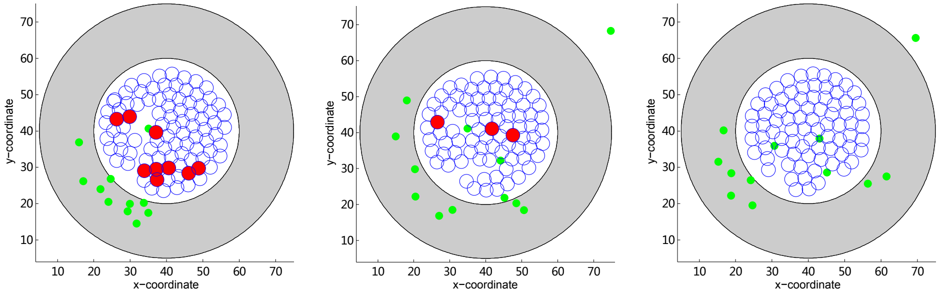

(g) t = 200 min (h) t = 300 min (i) t = 400 min

Figure 2.6: Snapshots of T-islets with anisotropic collagen orientation ($k = 0.3$) under a strong immune reaction. The blue, red and green circles denote the epithelial, cancer and T-lymphocytes, respectively.

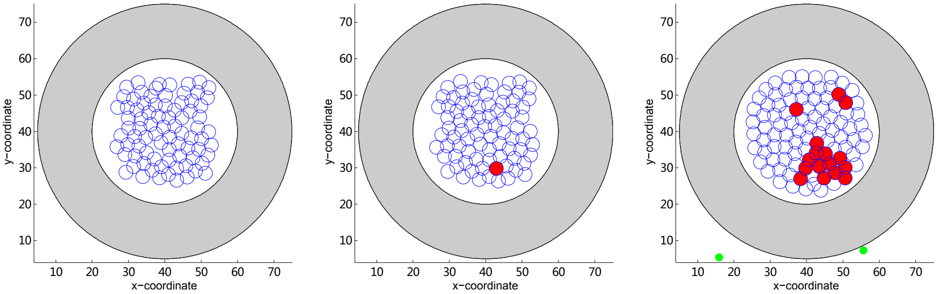

(a) t = 0 min (b) t = 10 min (c) t = 60 min

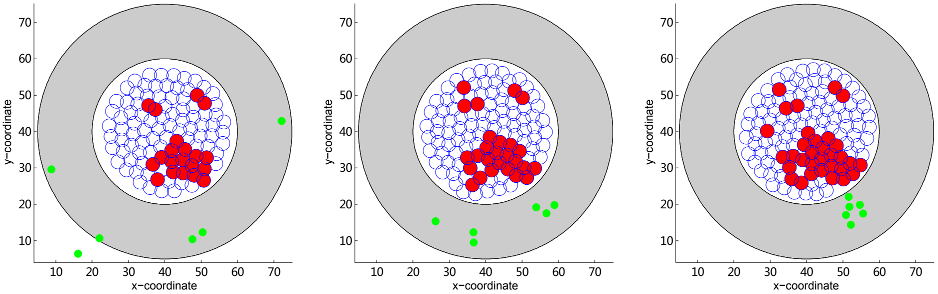

(d) t =120 min (e) t = 150 min (f) t = 180 min

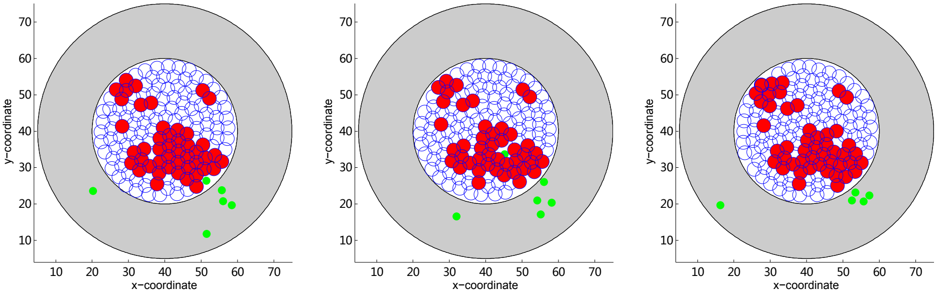

(g) t = 200 min (h) t = 300 min (i) t = 400 min

Figure 2.7: Snapshots of T-islets with anisotropic collagen orientation ($k = 0.3$) under a weak immune reaction. The blue, red and green circles denote the epithelial, cancer and T-lymphocytes, respectively.

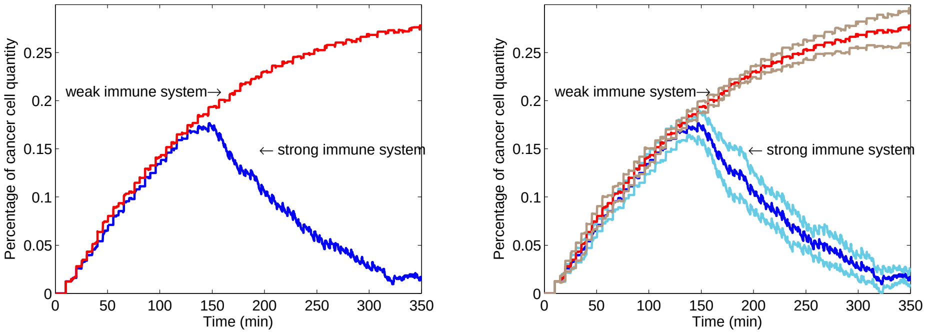

(a) (b)

Figure 2.8: (a) comparison for change of the percentage of cancer cells in total cells in two situations. The red and blue line represent the cancer cell percentage change in a weak immune system and a strong immune system, respectively. Furthermore, the corresponding confidence intervals are showed in (b). The brown and light blue lines denote the confidence intervals of a weak immune system as well as a strong immune system in T-islets with anisotropic collagen orientation ($k = 0.3$), respectively.

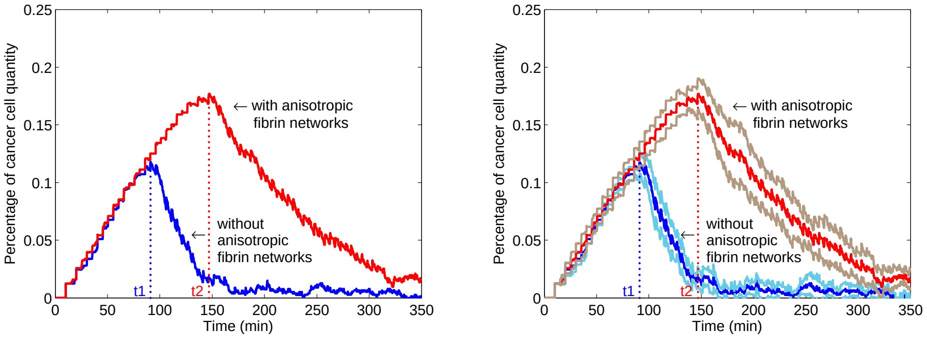

(a) (b)

Figure 2.9: (a) comparison for time to fight the cancer cells. The blue and red lines represent the strong immune system without anisotropic collagen orientation (with the response time t_1) and with anisotropic collagen orientation (with the response time t_2), respectively. Furthermore, the corresponding confidence intervals are showed in (b). The light blue and brown lines denote the confidence intervals of strong immune systems in T-islets without anisotropic collagen orientation ($k = 0$) as well as with anisotropic collagen orientation ($k = 0.3$), respectively.

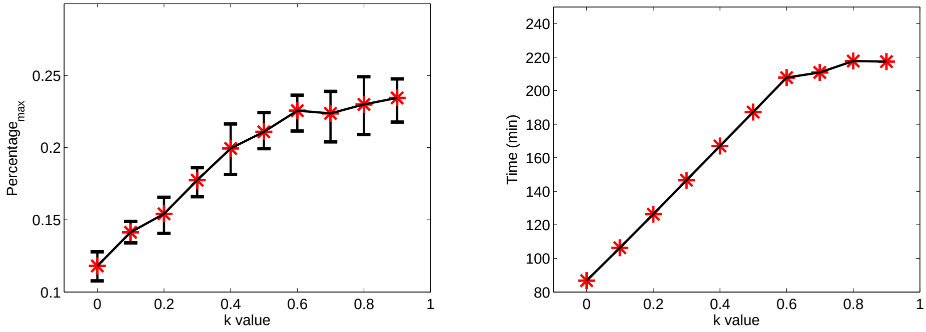

(a) (b)

Figure 2.10: (a) the relation between the maximum percentage of number of cancer cells and the k value in T-islets with anisotropic collagen orientation. The red asterisks and black lines represent average date and 95% confidence intervals. (b) the relation between the time of T-lymphocytes to fight the cancer cells with and the k value.

impedes the immune response of T-lymphocytes.

Differences in collagen fiber density lead to different orientation effects. To further investigate the effect of tumor surrounding collagen on T-lymphocytes movement in varying degrees, we give ten different values to k from 0 to 0.9. As we expected, the inhibitory effect of collagen increases with an increase of k value. This inhibitory is presented mainly by the parallel aligned fiber barrier on the attenuation of the cell radial velocity and orientation on the tangential direction. Correspondingly, the immune response time of T-lymphocytes and the maximum percentage of a number of cancer cells are two important criteria for judging the inhibitory effect, which are compared in Figure 2.10. The mean of the data for different k values is represented by red asterisks coming from a sample of 10 runs. Both the immune time and maximum number monotonically increase significantly at the beginning and then they gradually stabilize. Figure 2.11 shows the evolution of the number of cancer cells with respect to time for $k = 0, 0.3, 0.6$, respectively.

In conclusion, specific T-lymphocytes mediated immunity plays an essential role in T-islets progression. Pathologists have found that almost each individual has cancer cells after a large number of autopsy and pathological examination. However, most individuals only have very few cancer cells in vivo without any symptoms, which are not able to form cancer. Few cancer cells only can be seen under a microscope by a biopsy so that it is difficult to be diagnosed. Therefore the immune-related theoretical principles and tumor microenvironment need to be further simulated and researched.

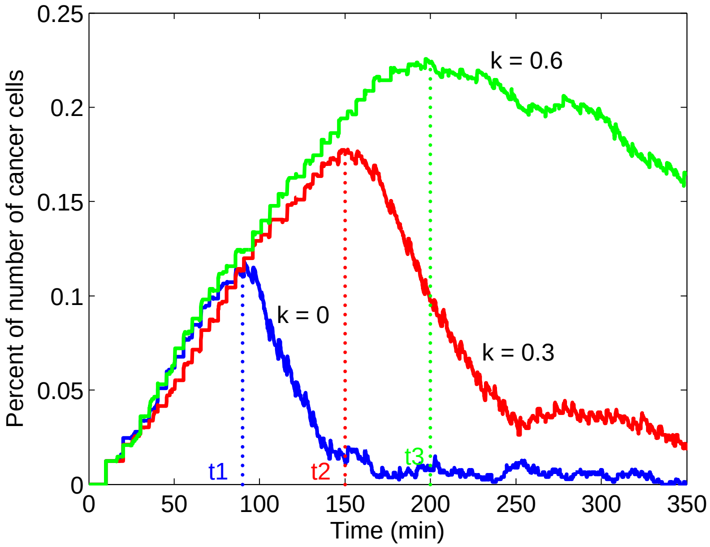

Figure 2.11: Evolution of percentage of number of cancer cells and immune time of T-lymphocytes with respect to $k = 0, 0.3, 0.6$, respectively.

2.5. DISCUSSION

Cancer cells differ from normal cells with some characteristics, such as unlimited growth, conversion as well as metastasis. Most individuals have a good balance of proto-oncogene and anti-oncogene. However, this balance can be disturbed by some carcinogens. Usually abnormal cells will be eliminated by the immune system before they become cancerous. Therefore the immune response is very important to fight cancer. However, tumors have many strategies to suppress or escape the tumor-specific immunity.

In this chapter, we phenomenologically model T-islets in pancreatic cancer, which uses the stroma to impede the immunity to some extent. As far as we know, this is the first mathematical modeling study devoted to the simulation of pancreatic cancer that takes into account the orientation of the surrounding collagen. In order to predict this influence, we have three characteristics for the comparative simulation study: 1) T-lymphocytes migrate to cancer cells without stromal ECM orientation in a strong as well as a weak immune response. It means T-lymphocytes sense the chemokine signal only and move according to the concentration gradient; 2) stromal ECM orientation combined with chemokine factor guide the movement of T-lymphocytes in two kinds of situations; 3) a parameter study of k value. Currently, we have three results listed as follows:

- The model quantifies the delay of invasion of T-lymphocytes into the cancer-affected area as a result of anisotropic collagen orientation, and hence it quantifies the increase in time to battle the cancer cells;

- The model predicts the unlimited proliferation of carcinoma cells if the immune system is weak, and a state of equilibrium where cancer cells are eliminated if the immune system is sufficiently strong;

- As we expected, the obstructing effect of stromal ECM increases with the increase of k value which is used to denote a measure for the amount that anisotropy contributed to T-lymphocytes migration. Hence the number of cancer cells is allowed to grow to larger values if the stromal ECM around T-islets gets more woven parallel to the circumference of the islet.

Although this model presents the first description of cancer development in the pancreatic under the influence of the orientation of the surrounding collagen, and although the modeling looks sensible and meaningful in a qualitative context, many details of cancer cells are ignored in order to get a simple, well-tractable model for this preliminary study. The following items regarding the improvement of the model can be discussed:

- Developing 3D model
  The computational framework that we currently present is in a 2D framework. This large simplification has been carried out to save CPU-time. The main objective of this chapter is to set up a formalism for the inhibition of the immune system as a consequence of the orientation of the stromal layer. However, a 3D model is more physiological to simulate the real biomedical phenomenon. Although, our work is only in 2D, the main conclusions remain the same. That is, the orientation of the stromal layer poses a delay to T-lymphocytes to entering T-islets. Therewith, the organism will have some difficulty in fighting cancer. Furthermore, the conclusions regarding the impact of the strength of the immune system on fighting cancer will be the same regardless of the dimensionality of the model. From a qualitative point, no significant changes are expected regarding dimensionality. However, if it comes to quantitative claims, then the dimensionality will have considerable impact. Therefore, in the future, we plan to develop a 3D model in a parallel computing environment.

- Improving the probability for cell division and death
  In some studies, it has been found that the length of telomere DNA of cells gradually shortens as the number of divisions of a cell increases. Lindsey *et al.* [125] report that the telomere length of skin cells becomes shorter

causing cell aging and lower division rates. This phenomenon is also observed for epithelial cells, T-lymphocytes and hematopoietic stem cells later. Allsopp *et al.* [126] observe that different individuals' fibroblasts have different abilities to proliferate and that the maximum number of divisions increases with increasing telomere length. Therefore a dynamic probability for cell division or death could be incorporated into the modeling to simulate initiation of cancer through an enhanced mutation rate of individual cells. In the current model, cells divide or die depending on the strain energy density as well as fixed probability rates after some time periods, however in future work we plan to incorporate this feature of the dynamic probability rates, which will be innovation with respect to the existing literature. A way to do this could be the following: let N be the number of cell divisions, then we may set,

$$\lambda_N - \lambda_{N-1} = C\lambda_N(1 - \lambda_N/\lambda_\infty), \tag{2.40}$$

where C is a positive constant and λ_N is the probability rate of cell division after N divisions per unit. Furthermore, λ_∞ stands for the probability rate for cell division after an 'infinite' number of cell divisions. If $C > 0$, then the number of cell divisions increases, the probability rates of mutation, proliferation and death will gradually converge to λ_∞, else convergence towards zero will be obtained.

- Incorporating more chemical factors
  In this study, the strain energy density as well as one chemokine are assumed to be the only factors for cell proliferation, apoptosis, mutation, etc. In reality, hormones, endostatin and other substances collectively influence the cell activity. Hence, one could incorporate oxygen content, nutrients, more chemokines, etc. This, however, would make the model less tractable.

- Coupling with angiogenesis
  Since the process of tumor growth is really complicated, it is not yet fully understood how the tumor grows. Modeling is still in its early stage without a unified theoretical basis. Angiogenesis plays a crucial role in tumor growth and its spreading over different parts of the body; therefore, how to build a proper model describing the angiogenesis mechanism is going to be a complicated challenge. Innermost cancer cells of any colony are most likely to die first, since the concentrations of oxygen and nutrients are much lower than the concentrations on the rim of the tumor and furthermore, the mechanical contact force, they are exposed to, are much longer.

We will take the concentrations of oxygen and nutrients into account for apoptosis. Cancer cells releasing angiogenic factor activate vascular epithelial cells and promote proliferation and migration of epithelial cells. We will simulate this part combined with tumor cell dynamics and associated immune responses in future work. The reader is referred to [127], where the current cell-based model was extended and applied to angiogenesis.

- Collagen degradation
  With the growth of tumors, internal hypoxic cancer cells will die and dead cells could initiate the mechanisms of angiogenesis by secretion of cytokines. One of the first steps in neovascularization is degradation of membrane collagens by endothelial cells, which move along the chemotactic stimulus. Endothelial cells are able to degrade interstitial type I collagen by releasing MMPs [128]. Therefore, we plan to incorporate this into the model to explore the efficacy of degradation of collagen in immune response as well as angiogenesis.

- A parameter variation study
  Besides all these questions, all models need input parameters, which are hard to find and which vary from individual to individual. Therefore, it is also important to carry out a probabilistic parameter variation study and try to get values from in vivo and in vitro measurements. Afterward, we could quantify the probability of tumor initiation, growth and seeding to other organs in terms of biophysical parameters, genetics and lifestyle in realistic settings and geometries.

The techniques that we used here reside on continuum models solved by the use of analytic expressions in terms of Green's functions or approximations, as well as stochastic principles for cell proliferation, mutation, death and migration. Combination with finite element strategies could improve the description regarding mechanics as well as more complicated reaction-transport equations for the chemokines. For cancer therapy, traditional methods are chemotherapy and radiotherapy, which aim at cancer cells. However, they inevitably cause varying degrees of damage and toxicity for the human body. Nowadays, cancer immunotherapy has some new developments that enlists the immune system to attack targeting tumors directly [129]. Thus our original model and further mathematical simulation is very meaningful and important for cancer immunotherapy. Furthermore, it lays a foundation for cancer development and inhibition for smart health care.

3

COMPUTATIONAL MODELING OF THERAPY ON PANCREATIC CANCER IN ITS EARLY STAGES

More than eighty percent of pancreatic cancer involves ductal adenocarcinoma with an abundant desmoplastic extracellular matrix surrounding the solid tumor entity. This aberrant tumor-microenvironment facilitates a strong resistance of pancreatic cancer to medication. Although various therapeutic strategies have been reported to be effective in mice with pancreatic cancer, they still need to be tested quantitatively in wider animal-based experiments before being applied as therapies. To aid the design of experiments, we develop a cell-based mathematical model to describe cancer progression under therapy with a specific application to pancreatic cancer. The displacement of cells is simulated by solving a large system of stochastic differential equations with the Euler-Maruyama method. We consider treatment with the PEGylated drug PEGPH20 that breaks down hyaluronan in desmoplastic stroma followed by administration of the chemotherapy drug gemcitabine to inhibit the proliferation of cancer cells. Modeling the effects of PEGPH20 + gemcitabine concentrations is based on Green's fundamental solutions of the reaction-diffusion equation. Moreover, Monte Carlo simulations are performed to quantitatively investigate uncertainties in the input parameters as well as predictions for the likelihood of success of cancer therapy. Our simplified model is able to simulate cancer progression and evaluate treatments to inhibit

---

The contents of this chapter have been published in paper [130]: Jiao Chen, Daphne Weihs and Fred J. Vermolen. "Computational modeling of therapy on pancreatic cancer in its early stages." Biomechanics and modeling in mechanobiology (2019): 1-18.

the progression of cancer.

3.1. INTRODUCTION

Cancer involves abnormal cellular proliferation and the disease has the potential to spread to other parts of the body. There are over two hundred different types of cancers including lung cancer, breast cancer, brain cancer, pancreatic cancer, etc. Most cancers have the same progression pattern in the sense that they initiate from a series of gene mutations resulting in uncontrolled proliferation, angiogenesis and metastasis. However, differences exist between cancer types and individuals which necessitates that the treatment is patient-specific, which normally is a combination of surgical resection, radiation therapy and systemic therapy.

The main treatment for pancreatic cancer is surgical resection, yet there is only a small resection rate of 15-20%. In addition, the cumulative 5-years survival rate after the first detection is around 20% [131] and the median survival is under 6 months. That is because pancreatic cancer is typically diagnosed late, and because of insensitivity to chemotherapy drugs, immune escape and other characteristics. Salmon and Donnadieu [132] observe that solid tumors look like islets (T-islets) surrounded by anisotropic desmoplastic extracellular matrix (ECM) that can form a physical barrier to the antitumor immune system response. At the early stage, mutated cancer cells in T-islets trigger massive desmoplasia including a variety of cells and a dense ECM as a natural defense that leads to vascular dysfunction and hence radiotherapy and systemic therapy are significantly hindered. The desmoplasia causes high interstitial fluid pressures that prevents drug diffusion. The high ECM density in pancreatic desmoplasia has been correlated to high concentrations of megadalton glycosaminoglycan hyaluronan (HA) [133]. In pancreatic ductal adenocarcinoma, the HA accumulates in the ECM with a frequency as high as 87% [134]. Since the HA can be depleted by the enzyme PEGPH20, a possible therapy could be based on the administering of PEGPH20 with a gemcitabine drug for pancreatic cancer therapy. Jacobetz *et al.* [135] show that combined therapy of PEGPH20 and gemcitabine inhibits tumor growth and improves survival of mice. Moreover, Provenzano *et al.* [133] experimentally demonstrate that PEGPH20 + gemcitabine alters tumor biology and increases immune response as well as overall survival in mice. Nevertheless, extended testing is necessary before the combined therapy can be used or even tested in clinical practice.

Systemic toxicity, as a side effect of drug therapy, influences organs and normal tissues. Gemcitabine is used as the front-line drug for the treatment of non-small cell lung cancer and pancreatic cancer, however, gemcitabine is toxic and known to sometimes induce myelosuppression, liver dysfunction, nephrotoxicity, etc. Moreover, cancer recurrence and drug resistance of cancer cells have bottlenecked recurrent or long-term chemotherapy. Therefore, the usage of drugs has to be researched and tested massively on animals and even patients. While animal-based experiments have benefited drug development, there are many ethical concerns and preclinical drug restrictions when carrying out these experiments. Mathematical modeling combined with well-designed experiments provides an avenue for cancer therapy research that will allow reduction of the number of animal experiments.

Mathematical modeling enables us to reshape our view of cancer from different perspectives. The process of establishing a mathematical model briefly includes the following steps: choice of a real problem, simplification of a biological phenomenon, establishment of mathematical quantification, and performance of numerical simulations. Compared with animal-based experiments, a prominent advantage of mathematical modeling offers an ethical, fast and cost-effective way to test various drug combination strategies, as well as various assumptions and predictions for cancer therapy.

Computational modeling has been developed for a broad spectrum of scales ranging from a few atoms to tissue level with applications to various stages of cancer progression. As early as in 1981, Moolgavkar and Knudson [136] developed a model for carcinogenesis at a cellular level. Similarly, Beerenwinkel *et al.* [137] develop a model to explore cancer initiation, in particular the genetic progression with an application to colorectal cancer is considered. Regarding the larger scales, the possibilities to simulate the effects of radiotherapy and chemotherapy for brain tumors by using mathematical modeling are studied by Powathil *et al.* [66]. Other mathematical models on cancer therapy can be found in [54, 55]. In terms of mathematical modeling related to pancreatic cancer therapy, resources like [138, 139] are rare, and therefore we develop a computational model to investigate therapeutic combinational possibilities using a Bayesian parameter sensitivity analysis [140].

This chapter describes a mathematical model that is a continuation of Chapter 2. The innovations with respect to the aforementioned work are the following: 1) the model has been extended to the simulation of administering drugs that inhibit the proliferation of cancer cells and decay the densely packed, circumferentially oriented ECM around the cancer region; 2) an uncertainty quantification has been carried on the basis of the model parameters to predict the likelihood for successful therapy or further development of cancer. We expect that these principles can be transferred to cancers of different nature. We first consider the injection of enzyme PEGPH20 to degrade HA in the desmoplastic ECM such that T-lymphocytes infiltration is increased. We then study the effects of subsequent gemcitabine injection to inhibit the proliferation and growth of cancer cells. Injections of both enzyme and drug are modeled by using Green's functions as solutions of reaction-diffusion equations. Furthermore, the sensitivity of the model with respect to various input parameters is investigated using Monte Carlo simulations.

3.2. METHOD

In this chapter, we develop the mathematical formalism that is used in the current study. We present the way that various cell types are modeled, in terms of migration, cell death, proliferation and mutation. Next to various cell types, we explain how the treatments are incorporated in the model.

3.2.1. MOTIVATION FROM EXPERIMENTAL OBSERVATIONS

Cell culture. Regarding Figure 3.1(a) and (b), we have used two commercially-available human, pancreatic cell lines (ATCC, Manassas, VA): BxPC-3 (collected from primary site with no evidence for metastasis) and AsPc1 (from metastatic site, ascites). Cells were cultured in their appropriate media as recommended by manufacturer. RPMI-1640 Medium (Biological Industries, Kibbutz Beit Haemek, Israel) supplemented with 10 %vol. FBS (ThermoFisher Scientific, Waltham, MA), 1 %vol. of penicillin-streptomycin (Biological Industries, Kibbutz Beit Haemek, Israel), 0.46 %vol. D-Glucose solution, 1 %vol. HEPES solution, and 0.66 %vol. sodium bicarbonate solution (all from Sigma, St Louis, MO). Cells were maintained in a sterile incubator at 37 °C, 5 % CO_2, and high humidity. Cells were frozen at low passages from ATCC stock (i.e. 3-5), and for experiments cells were thawed and used in passages 7-30 from the ATCC stock.

Microscopy and imaging. Cells seeded on 10 cm tissue culture plastic plates were imaged using an inverted, epifluorescence Olympus IX81 microscope, with a 20x/0.5NA differential interference contrast (DIC, Nomarsky optics) air-immersion, objective lens. Cells at random locations were imaged while being maintained in 37 °C , 5 % CO_2, and high humidity (90 %), in an on-stage an on-microscope incubator (Life Imaging Services, Switzerland), to sustain their viability for prolonged periods of time.

Assumptions. Many of the fundamental biological assumptions in the current model are taken from Chapter 2, since the current chapter is an extension of Chapter 2 where therapy is taken into account. We summarise biological assumptions, which are needed to have a tractable model.

1. We only consider three phenotypes: epithelial cells, cancer cells and T-lymphocytes;

2. Each cell can be in the following two states: dead or viable;

3. Currently, we consider a two-dimensional (2D) domain of computation to avoid very large computation times. Further, cell deformation is not taken account for reasons of computational efficiency, and therefore all cells are assumed to be circular;

4. Because of the lack of information regarding the composition of the desmoplastic stroma, we assume its density to be uniform. We do take into account the variability of the orientation of the desmoplastic stroma by using the orientation tensor;

5. According to the experimental studies by Reinhart-King *et al.* [40], cells are able to communicate by mechanical forces exerted on the surrounding substrate. This mode of long-distance communication has been incorporated in the current chapter on the basis of the strain energy density. In the modeling, the strain energy density impacts the direction of migration of the cells;

6. Intercellular contact is simulated by modeling the cells as elastic, soft circles in the 2D framework. Here, Hertz contact mechanics has been used, which is also proposed in the mouse experimental paper by Gefen [141], which treats the invagination of viruses into cells;

7. Cells are subject to various modes of migration. In this chapter, we assume that chemotaxis of T-lymphocytes migration results from the secretion of a generic chemokine that is secreted by the cancer cells. Furthermore, since the extracellular matrix always contains inhomogeneities, of which the exact locations are unknown, we incorporate a random component to the migrational vectors of the cells. This randomness is modeled by a random walk, which is a very common approach in the literature [142];

8. Cumming *et al.* [143] model orientation effects of extracellular matrix in the context of wound healing in the skin. Since Salmon and Donnadieu [132] observe T-lymphocytes peripheral migration around T-islets in cancer, where the cells only exhibit very little movement in the direction perpendicular to the periphery, we follow the approach of [143] to incorporate orientational variations of the desmoplastic stroma;

9. According to the experimental studies by Kar *et al.* [144], homogeneous cultures of cell exhibit the same cell cycle if it comes to division and death. However, the rates on which the cell cycles proceed differs from cell to cell. Kar *et al.* [144] observe a random pattern which they catch in statistical

distributions. Therefore, we incorporate cell division, mutation and death as random processes.

Next, we incorporate the assumptions behind the therapy, which is based on the administering of the cocktail of PEGPH20 and gemcitabine. This therapy has been tested on mice, which results in an improvement of survival of mice subject to pancreatic cancer. We model the impact of therapy by the use of the following assumptions:

1. We consider a circular domain of computation, which is in line with the pancreatic experimental observations [145, 146]. Our Figure 3.1(b) also demonstrates this circular domain, where an early circular cluster of densely packed cancer cells is observed with edge-cells exhibiting a unique morphology. This is also found in the studies by Salmon and Donnadieu [132]. Therefore, a circular cancer domain with a circumferentially ring-shaped desmoplastic stroma is modeled and depicted in Figure 3.2(b);

2. Jacobetz *et al.* [135] indicate that PEGPH20 can possibly be used to degrade the desmoplastic stroma. Therefore, we assume that PEGPH20 makes the orientation of the desmoplastic stroma more isotropic, and hence the T-lymphocytes migration into T-islets is enhanced;

3. Gemcitabine is a very general drug for chemotherapy against pancreatic cancer. This chemical is known to inhibit DNA synthesis, and hence cell proliferation is frustrated [147]. Therefore, we assume that gemcitabine suppresses the proliferation of cancer cells;

4. Since it is hard to obtain constitutive relations for the diffusivities of the various chemicals (drugs and cancer cell-secreted chemokine), we assume that diffusion of all chemicals is based on Fick's law for linear diffusion. Furthermore, we are only interested in the qualitative behaviors of diffusion, and therefore we use Green's functions to describe the concentration fields. A further motivation for this approach is that the Green's functions easily provide explicit relations for concentrations and their gradients, which are needed for modeling chemotaxis, without the need of mapping from finite-element meshes (which possibly results into a loss of accuracy).

3.2.2. MIGRATION OF EPITHELIAL AND CANCER CELLS

Cancer initiates from genetic mutations, therefore we consider the normal epithelial cells, which can mutate to cancer cells, and cancerous cells in a bounded computational domain $\Omega \subset \mathbb{R}^2$. The set of epithelial and cancerous cells at time

t is denoted by $\mathbb{W}(t)$. Cells migrate in the domain Ω and interact with each other as well as with its microenvironment, e.g. substrate in 2D or ECM in 3D. Generally, cell migration is classified into amoeboid or mesenchymal movement. Cancer cells have the ability to change state between these two migrational modes in order to adapt to environmental changes. In this chapter, we assume that cells migrate according to mechanical signals as a result of substrate deformation caused by neighbor cells' adhesion and traction [148]. For completeness, we present some of the equations from [41]. Slight deformation of substrate gives strain energy U as

$$U = \frac{1}{2} V E \varepsilon^2, \tag{3.1}$$

where V and E denote the deformation volume and Young's modulus. Note that ε defines strain of the substrate given by $\varepsilon = \frac{d}{L}$ with d in deformed vertical displacement and L in the thickness of the substrate. Then the strain energy density (total energy per unit of volume) M_i^0 is calculated by

$$M_i^0 = \frac{1}{2} E_{\mathrm{s}}(\mathbf{r}_i)\varepsilon^2, \quad \text{for } i \in \mathbb{W}(t). \tag{3.2}$$

Here $E_{\mathrm{s}}(\mathbf{r}_i)$ denotes Young's modulus of substrate at the center of cell i and $\mathbf{r}_i = (x_i, y_i)$ is its corresponding position. If Equation (3.2) is combined with Hooke's Law $\varepsilon = \frac{1}{E_{\mathrm{s}}(\mathbf{r}_i)} \frac{F_i}{\pi R^2}$, then we get

$$M_i^0 = \frac{1}{2\pi^2} \frac{F_i^2}{E_{\mathrm{s}}(\mathbf{r}_i) R^4}, \quad \text{for } i \in \mathbb{W}(t). \tag{3.3}$$

For cell i with radius R, F_i represents the exerted force on the substrate. The total strain energy density that a cell detects, originates from itself as well as from the other neighboring cells. Cells are able to detect signals from other cells if a certain threshold is exceeded for the strain energy density [40, 92]. Since the mechanical signal decays with the distance, we compute the attenuation of the signal from another cell j by

$$M_i(\mathbf{r}_j) = M_i^0 \exp\{-\lambda_i \frac{\parallel \mathbf{r}_i - \mathbf{r}_j \parallel}{R}\}, \quad \text{for } i, j \in \mathbb{W}(t). \tag{3.4}$$

The attenuation factor λ_i can be approximated by $\lambda_i = \frac{E_s(\mathbf{r}_i)}{E_c}$ [149], where E_c is Young's modulus of the cell. Since the strain energy density is a scalar, the total value of one cell at position $\mathbf{r}_i$ can be obtained by summing, that is

$$M(\mathbf{r}_i) = \sum_{j \in \mathbb{W}(t)} M_j(\mathbf{r}_i) = M_i^0 + \sum_{i,j \in \mathbb{W}(t)_{j \neq i}} M_j^0 exp\{-\lambda_j \frac{\parallel \mathbf{r}_i - \mathbf{r}_j \parallel}{R}\}. \tag{3.5}$$

Based on the work by Vermolen and Gefen [41], the displacement direction of a cell is determined by the unit vector between itself and other cells, for example, $\mathbf{e}_{ij} = \frac{\mathbf{r}_i - \mathbf{r}_j}{\|\mathbf{r}_i - \mathbf{r}_j\|}$ for cell i and cell j. At time t, the final displacement direction $\mathbf{z}_i$ of cell i can be obtained by the following linear combination of unit vectors obtained through the interconnection vectors between the cells,

$$\mathbf{z}_i = \sum_{j=1_{j\neq i}}^{n} M_j(\mathbf{r}_i(t))\mathbf{e}_{ij}, \quad \text{for } i \in \mathbb{W}(t). \tag{3.6}$$

Under the mechanical stimulus, the total displacement of a cell per time step $\mathrm{d}t$ is given by

$$\mathrm{d}\mathbf{r}_i(t) = \alpha_i M(\mathbf{r}_i(t))\hat{\mathbf{z}}_i \mathrm{d}t, \quad \text{for } i \in \mathbb{W}(t). \tag{3.7}$$

In Equation (3.7), $\hat{\mathbf{z}}_i$ is a unit vector ($\hat{\mathbf{z}}_i = \frac{\mathbf{z}_i}{\|\mathbf{z}_i\|}$) and the velocity parameter α_i follows from [141] and is given by

$$\alpha_i = \frac{\beta_i R^3}{\mu F_i}, \quad \text{for } i \in \mathbb{W}(t), \tag{3.8}$$

where μ is the cell-substrate friction coefficient and β_i represents the mobility coefficient of the area of one cell that is in contact with the substrate.

Cell contact inhibition is a biological mechanism to inhibit cell proliferation and to decrease mobility. As a result, the migration speed can be dampened if two cells collide. Therefore, we incorporate a repulsive invagination force M^{ij} between cell i and cell j as introduced in [141], which increases with the impinging distance. The equation reads as

$$M^{ij} = \frac{4}{15\sqrt{2}} \frac{E_c}{\pi} (\frac{h}{R})^{\frac{5}{2}}, \quad \text{for } i, j \in \mathbb{W}(t). \tag{3.9}$$

The variable h is the distance of impingement given by $h = \max(2R - \| \mathbf{r}_{ij} \|, 0)$, where $\mathbf{r}_{ij}$ defines the distance between cell i and cell j. Note that this equation guarantees that any number of cells will not overlap too much during the collision.

Taking the unpredictability of cell migration into account, we extend the model with a temporal stochastic process in the form of a Wiener process ($W \sim \mathcal{N}(0, \mathrm{d}t)$). In summary, the displacement of epithelial and cancer cells is determined by the strain energy density, total repulsive force $M^{mc}(\mathbf{r}_i)$ and random walk, and thereby the revised equation is written as

$$\mathrm{d}\mathbf{r}_i(t) = \alpha_i \hat{M}_i(\mathbf{r})\hat{\mathbf{z}}_i \mathrm{d}t + \eta \mathrm{d}\mathbf{W}(t), \quad \text{for } i \in \mathbb{W}(t), \tag{3.10}$$

where $\hat{M}_i(\mathbf{r})$ is the total mechanical signal, which is given by $\hat{M}_i(\mathbf{r}) = M(\mathbf{r}_i) - M^{mc}(\mathbf{r}_i)$ and η represents a constant in this random walk. Further, $\mathrm{d}\mathbf{W}(t)$ represents a vector with independent samples from $\mathcal{N}(0, \mathrm{d}t)$. In $\mathbb{R}^2$ and $\mathbb{R}^3$, the number of components of $\mathrm{d}\mathbf{W}(t)$ is two and three, respectively. To solve the problem, we use the Euler-Maruyama method [150], which boils down to the ordinary forward Euler method combined with the Wiener process:

$$\mathbf{r}_i^n = \mathbf{r}_i^{n-1} + \Delta t \alpha_i \hat{M}_i(\mathbf{r}^n) + \eta \Delta \mathbf{W}(t), \quad \text{for } i \in \mathbb{W}(t). \tag{3.11}$$

Here, $\Delta\mathbf{W}(t)$ represents a vector with independent samples from $\mathcal{N}(0, \Delta t)$. The above equation contains a time-integration in which a part is random from the Wiener process. Using a higher-order method makes the numerical error smaller than the actual uncertainty. Therefore, we decided to use the ordinary Euler-Maruyama method in which the deterministic part is treated by a first-order forward Euler method. However, to ensure the numerical stability, the time step cannot be chosen arbitrarily large. If we restrict the displacement of a cell step to one-fourth of the cell diameter, then, the time step is bounded by $\Delta t \leq \frac{R}{2\max\|\mathbf{v}_i\|}$ with $\mathbf{v}_i$ denoting an equilibrium velocity of cell i.

3.2.3. MIGRATION OF T-LYMPHOCYTES

Migration of cells can be driven by several cues. Such cues can be chemicals, electricity, mechanical properties (such as stress or elasticity) and light. For the locomotion of T-lymphocytes, we take chemotaxis and small range impingement into account. According to [151, 152], immune cells like cytotoxic T-lymphocytes move towards the gradient of chemokines secreted by cancerous cells. We use $\mathbb{K}(t)$ and $\mathbb{T}(t)$ to represent the set of cancer cells and the T-lymphocytes at time t, respectively. Each cancer cell is modeled as a point source, therefore we consider the Dirac Delta distribution $\delta(\mathbf{r})$ to model the chemokine secreted by each cancer cell. Then, the concentration of the chemokine change is described as

$$\frac{\partial c}{\partial t} - D_c \Delta c = \sum_{j \in \mathbb{K}(t)} \gamma_j(t) \delta(\mathbf{r} - \mathbf{r}_j(t)), \quad \text{for } j \in \mathbb{K}(t). \tag{3.12}$$

In Equation (3.12), c, D_c and $\gamma_j(t)$ denote chemokine concentration, diffusivity and secretion rate by cancer cells at time t. For the sake of simplicity and applicability of the Green's functions and in order to avoid the enlargement of the parameter space in the model, we take all diffusion coefficients constant over the various subdomains in all the simulations. Regarding the time-dependent scheme, it takes computational time and memory to store all the positions of cancer cells at all times. Therefore we solve the steady-state part of Equation (3.12), which results into

$$
\begin{aligned}
\frac{\partial c}{\partial x}(x,y) &= -\sum_{j\in\mathbb{K}(t)} \frac{\gamma_j(t)}{2\pi D_c}\frac{x-x_j(t)}{\| \mathbf{r}-\mathbf{r}_j(t) \|^2},\\
\frac{\partial c}{\partial y}(x,y) &= -\sum_{j\in\mathbb{K}(t)} \frac{\gamma_j(t)}{2\pi D_c}\frac{y-y_j(t)}{\| \mathbf{r}-\mathbf{r}_j(t) \|^2}.
\end{aligned} \tag{3.13}
$$

Analogously, any two T-lymphocytes are not allowed to overlap too much, thus the contact inhibition is considered by using mechanical repulsion M^{mc} in Equation (3.9). Furthermore, the random walk is incorporated as well to mimic the unpredictable migratory behaviors of T-lymphocytes. However, the remote mechanical cues are disregarded for the migration of T-lymphocytes. Then the displacement of T-lymphocytes is written as

$$
\mathrm{d}\mathbf{r}_j(t) = \beta\nabla c(t,\mathbf{r}_j(t))\mathrm{d}t + \eta\mathrm{d}\mathbf{W}(t) - M^{\mathrm{mc}}(\mathbf{r}_j)\mathbf{z}_j\mathrm{d}t, \quad \text{for } j\in\mathbb{T}(t), \tag{3.14}
$$

where β defines the chemotactic constant. Similarly, $\mathrm{d}\mathbf{W}(t)$ is a vector Wiener process. The displacement of T-lymphocytes is dealt with by using the same Euler-Maruyama method expressed by

$$
\mathbf{r}_j^n = \mathbf{r}_j^{n-1} + \nabla c(t,\mathbf{r}_j^{n-1})\Delta t + \eta\Delta\mathbf{W} - M^{\mathrm{mc}}(\mathbf{r}_j^{n-1})\mathbf{z}_j^{n-1}\Delta t, \quad \text{for } j\in\mathbb{T}(t). \tag{3.15}
$$

For an overview of cross-talk between cells and microenvironment, the reader is referred to Figure 2.1 in Chapter 2.

3.2.4. STOCHASTIC PROCESSES: CELL DIVISION, MUTATION AND DEATH

Cell proliferation, mutation and death are some of the fundamental processes of cells regulated by genes, intracellular interaction and microenvironment. To simplify the model, stochastic processes are considered to simulate the probability of cell division, mutation and death [153]. We hypothesize that the probability of cell division, mutation and death is only influenced by the total strain energy density one cell endures. Then the probability density for $t > t_n$ is given by

$$
f_{t_n}(\lambda,t) = \lambda\exp(-\lambda(t-t_n)), \quad \text{for } t > t_n, \tag{3.16}
$$

where $\lambda > 0$ is the probability rate of cell division, mutation or death per hour. This probability density is common in modeling waiting times of discrete phenomena, see [154](page 95). Hence, the probability is achieved by time integration

$$
\begin{aligned}
P(t\in(t_n,t_n+\Delta t)) &= \int_{t_n}^{t_n+\Delta t} f_{t_n}(\lambda,t)\mathrm{d}t\\
&\simeq 1-\exp(-\lambda\Delta t).
\end{aligned} \tag{3.17}
$$

Note that the incidence of cell division, mutation or death is determined by ξ as

$$0 \leq \xi \leq 1 - \exp(-\lambda \Delta t), \tag{3.18}$$

where $\xi \sim u[0,1]$ is generated from an uniform distribution. Since most chemotherapy drugs target on DNA generation and thereby inhibit cell division, the probability rate λ of cancer cells division and mutation reads as

$$\lambda = \begin{cases} \lambda_0 \\ \lambda(c(t)) = \lambda_0 \exp(-A c_{\text{drug}}) \end{cases}, \tag{3.19}$$

where λ_0 denotes the initial probability rate and $\lambda(c(t))$ represents the probability rate for cancer cell proliferation under the influence of drug therapy.

3.2.5. DESMOPLASTIC ECM

Despite the enormous number of cellular studies, the interaction between cancer cells and the microenvironment is still poorly understood. In pancreatic cancer, the components of the desmoplastic ECM around T-islets are likely dynamic and thus its function is controversial. Some studies [132, 155] suggest that the desmoplastic ECM supports cancer progression, whereas some studies hint to the contrary [156]. However, there is a consensus that cancer cells in the pancreas are able to reshape the normal ECM to adapt to their survival needs. Some of the properties of the desmoplastic ECM can be generalized as, 1) profuse fibers that are arranged in parallel to the circumference of the T-islets that leads to an anisotropic environment; 2) abundant regeneration of HA results in local, stiff tissue; 3) the stiff desmoplastic ECM acts as a solid defense that hinders the entry of many agents, e.g. immune cells, blood vessel generation, drugs, etc.

Due to chemotaxis, T-lymphocytes tend to move towards the gradient of the concentration of chemokines secreted by cancer cells [132]. However, their migration is guided by the desmoplastic ECM orientation once T-lymphocytes enter the anisotropic desmoplastic ECM [157]. As a result, T-lymphocytes preferably migrate in the tangential direction and slow down in the radial direction, which results in the behavior that cells are migrating around the tumor, and hence the cells do not penetrate the tumor. To model the orientation in the 2D framework, we introduce an orientation tensor $\Psi(t, \mathbf{x})$ [143]

$$\Psi(t, \mathbf{x}) = \begin{pmatrix} \Psi_{xx} & \Psi_{xy} \\ \Psi_{xy} & \Psi_{yy} \end{pmatrix}. \tag{3.20}$$

The tensor is symmetric according to the tangential and radial directions. Thereby the orientation tentor is calculated by

$$\Psi = v^0 e^{-ks} \lambda_1 \mathbf{w_1} \mathbf{w_1}^T + v^0 \lambda_2 \mathbf{w_2} \mathbf{w_2}^T, \tag{3.21}$$

where $\mathbf{w_1}$ and $\mathbf{w_2}$ are orthogonal eigenvectors denoting the radial and tangential components [143]. The eigenvalues λ_1 and λ_2 are the corresponding weights. Furthermore, there is an attenuation in radial speed with rate constant k reading as $\frac{\partial v}{\partial s} = -kv$. Here s represents the penetration depth and finally v is given by $v = v^0 e^{-ks}$ with an initial velocity v^0 on the ECM external boundary, see Equation (3.21). Finally, the displacement of T-lymphocytes under the influence of collagen orientation is adjusted to

$$\mathbf{r}_j^n = \mathbf{r}_j^{n-1} + \mu_j \Psi(\nabla c(t, \mathbf{r}_j^{n-1})\Delta t + \eta \Delta \mathbf{W}) - M^{\mathrm{mc}}(\mathbf{r}_j^{n-1})\mathbf{z}_j^{n-1}\Delta t, \quad \text{for } j \in \mathbb{T}(t), \tag{3.22}$$

where μ_j denotes the chemotactic mobility rate.

At present, we have relevant experimental results shown in Figure 3.1 to support our simplified model. As above-mentioned, pancreatic cancer is typically diagnosed at late stages with a high metastasis risk. Highly metastatic pancreatic cancer cells, already in their invasive state, are more likely to remain as individuals especially during the invasion, see Figure 3.1(a). In contrast, non-invasive cancer cells accumulate into dense clusters on plates, likely emulating rapid proliferation in the early stages of tumor growth (see Figure 3.1(b)). We consider the structure of the cluster of cancer cells, with its highly dense cells, as already similar to a circular islet, which is surrounded by tangentially oriented desmoplastic ECM.

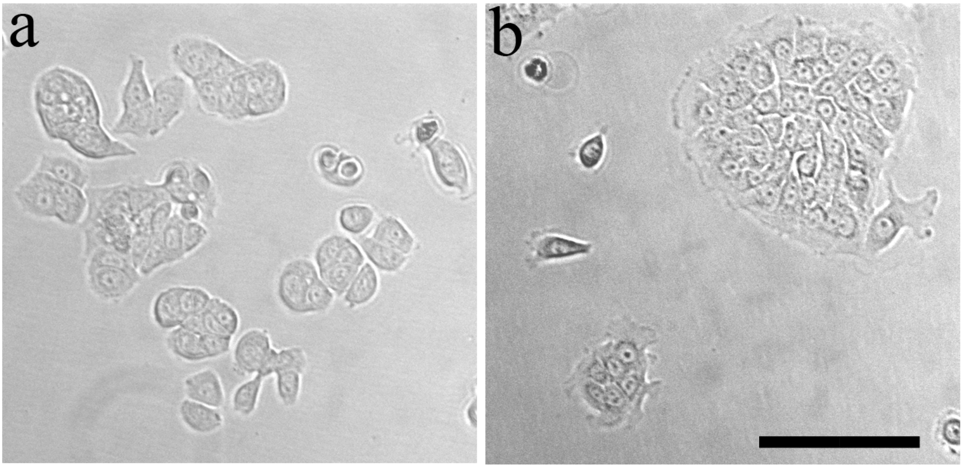

Figure 3.1: Pancreatic cancer cells on plastic tissue culture dishes. (a) high metastatic potential cell line (AsPC-1). (b) low metastatic potential or locally invasive cell line (BxPC-3). The periphery of the cluster is structured differently than its interior. Scale bar is 100mm.

3.2.6. ENZYME AND DRUG INJECTION

Pancreatic cancer frustrates the human immune system and builds a physiological barrier to protect itself [133, 158]. These two properties render chemotherapy pointless, since most chemotherapy drugs are given by intravenous injection and subsequently arrive at the tumor via the bloodstream [159]. Compared with other types of cancers, the regeneration of new blood vessels does not take place in the anisotropic ECM in pancreatic cancer, whereas cancer cells are capable of surviving under conditions with few nutrients due to insufficient blood supply [160]. Therefore, in our simulations, we initially mimic a treatment that in the first step aims at the degradation of the ECM that will then allow drug delivery to the cancer cells.

Jacobetz *et al.* [135] show that abundant HA impairs vascular function and hinders drug delivery, and hence degradation of HA combined with chemotherapy drugs could be an option for treatment. The enzyme PEGPH20 is considered here to degrade HA rapidly and efficiently and is administered by injections. The injection can be regarded as a source point when using the Dirac Delta distribution δ and the corresponding concentration c_{en} diffuses based on

$$\frac{\partial c_{\mathrm{en}}}{\partial t} - D_{\mathrm{en}} \Delta c_{\mathrm{en}} = \sum_{p \in \mathbb{P}(t)} \gamma_{\mathrm{en}}(t) \delta(\mathbf{r} - \mathbf{r}_p(t)), \tag{3.23}$$

where D_{en} and $\mathbb{P}(t)$ denote the enzyme diffusivity and the set of multiple injections. The injection rate $\gamma_{\mathrm{en}}(t)$ of each injection site is defined as

$$\gamma_{\mathrm{en}}(t) = \begin{cases} \gamma_0, & \text{if } t_0 < t \leq t_1 \\ 0, & \text{else} \end{cases}, \tag{3.24}$$

which means that PEGPH20 is injected at time t_0 until time t_1 and no more enzyme is given afterward. A schematic timeline of T-islet model in the domain Ω with important marks is shown in Figure 3.2(a), where the time of drug administration is referred to [135]. When the percentage of cancer cells amount in total cells amount exceeds 35%, the PEGPH20 starts to be injected and time is marked as t_0. To simplify the description of the process, we assume that the enzyme is injected once at position $\mathbf{r}_p$ nearby T-islets and thence the concentration of enzyme with respect of time t at location $\mathbf{r}$ is

$$c_{\mathrm{en}}(\mathbf{r}) = \int_0^t \frac{\gamma_{\mathrm{en}}(t)}{4\pi D_{\mathrm{en}}(t-s)} e^{\frac{\|\mathbf{r}-\mathbf{r}_p\|^2}{4D_{\mathrm{en}}(t-s)}} \,\mathrm{d}s = \int_{t_0}^{t_1} \frac{\gamma_0}{4\pi D_{\mathrm{en}}(t-s)} e^{\frac{\|\mathbf{r}-\mathbf{r}_p\|^2}{4D_{\mathrm{en}}(t-s)}} \,\mathrm{d}s. \tag{3.25}$$

The second equality sign results after applying Equation (3.24). Once the drug has been injected, it diffuses to its surroundings according to

$$\frac{\partial c_{\mathrm{drug}}}{\partial t} - D_{\mathrm{drug}} \Delta c_{\mathrm{drug}} = \sum_{q \in \mathbb{D}(t)} \gamma_{\mathrm{drug}}(t) \delta(\mathbf{r} - \mathbf{r}_q(t)), \tag{3.26}$$

where D_{drug} and $\mathbb{D}(t)$ denote the drug diffusivity and the set of multiple injections. Subsequently, the injection rate γ_{drug} of chemotherapy drug gemcitabine during time interval (t_2, t_3) as well as afterward is given by

$$\gamma_{\text{drug}}(t) = \begin{cases} \gamma_0, & \text{if } t_2 < t \leq t_3 \\ 0, & \text{else} \end{cases}, \tag{3.27}$$

and using Equation (3.27) its diffused concentration c_{drug} at position $\mathbf{r}$ with injected position $\mathbf{r}_d$ in desmoplastic ECM is expressed as,

$$c_{\text{drug}}(\mathbf{r}) = \int_0^t \frac{\gamma_{\text{drug}}(t)}{4\pi D_{\text{drug}}(t-s)} e^{\frac{\|\mathbf{r}-\mathbf{r}_d\|^2}{4D_{\text{drug}}(t-s)}} \mathrm{d}s = \int_{t_2}^{t_3} \frac{\gamma_0}{4\pi D_{\text{drug}}(t-s)} e^{\frac{\|\mathbf{r}-\mathbf{r}_d\|^2}{4D_{\text{drug}}(t-s)}} \mathrm{d}s. \tag{3.28}$$

In pancreatic cancer, gemcitabine targets on inhibiting the proliferation of cancer cells. Moreover, this model can be extended to immunotherapy in the form of an injection of antibodies to boost the immune system or by the use of immune checkpoint inhibitors, etc. Cancer cells enable the immune checkpoint protein (like CTLA-4, PD-1, PD-L1, etc.) of T-lymphocytes to be over-expressed which is not conducive to the activation of T-lymphocytes.

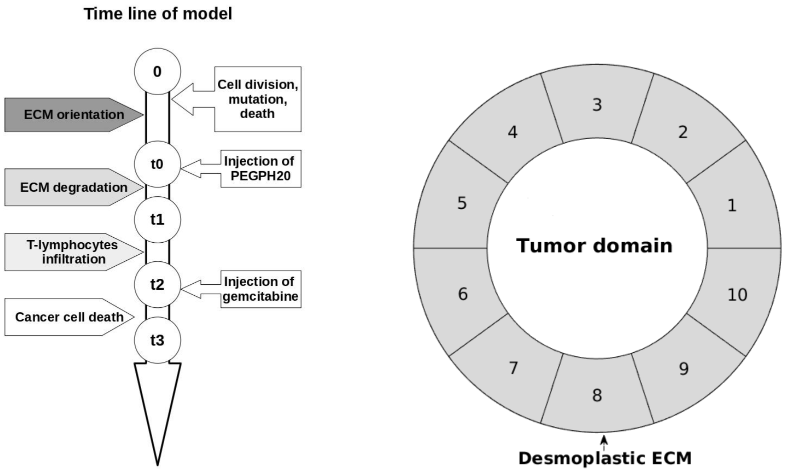

(a) (b)

Figure 3.2: Schematic figures. (a) the timeline of T-islets model in domain Ω. (b) a circular desmoplastic ECM, which is divided into ten subdomains (indexed from 1 to 10) for computation.

To consider the variation in concentration of enzyme or drug, the circular desmoplastic ECM (see Figure 3.1(b)) is divided into subdomains as shown in Figure 3.2(b). In each subdomain, the middle point is used to sense the enzyme/ drug concentration given by

$$\mathbf{x}_i = \left(\frac{R_1+R_2}{2}\cos\left(2\pi\frac{(i-1)}{\mathrm{N}}\right), \frac{R_1+R_2}{2}\sin\left(2\pi\frac{(i-1)}{\mathrm{N}}\right)\right), \quad \text{for } i \in \{1,\ldots,\mathrm{N}\}. \tag{3.29}$$

Here R_1 and R_2 are the radii of the inner and outer boundaries, respectively, which are divided by $\mathrm{N} = 10$ points. We only use the subdomains during the treatments since the enzyme and drug concentrations exhibit variations over the periphery of the ECM around the tumor.

In experiments [135], PEGPH20 treatment leads to a significant increase in fenestrae, interendothelial gaps and macromolecular permeability. Moreover, Shepard [134] demonstrates that PEGPH20 treatment stimulates immune NK cells and trastuzumab penetration. Thereby the antitumor response is boosted. The penetration of immune cells and macromolecular structure benefit from less HA in ECM, which additionally weakens the impact of desmoplastic ECM orientation on cell migration. In our previous chapter, we used constants for eigenvalues λ_1 and λ_2 in Equation (3.21) to calculate the desmoplastic ECM orientation. In the current work, $\lambda_2(t,\mathbf{r})$, denoting the tangential orientation component at position r in ECM, is adjusted over time by

$$\frac{\partial\lambda_2(t,\mathbf{r})}{\partial t} = \mathrm{L}(\lambda_1 - \lambda_2(t,\mathbf{r}))c_{\mathrm{en}}(t,\mathbf{r}), \tag{3.30}$$

where L is a rate constant. Let n be the time index, then subsequently $\lambda_2^{n+1}(\mathbf{r})$ can be approximated from the previous time step by

$$\lambda_2^{n+1}(\mathbf{r}) = \lambda_2^n(\mathbf{r}) + \mathrm{L}(\lambda_1 - \lambda_2^n(\mathbf{r}))c_{\mathrm{en}}^n(\mathbf{r})\Delta t. \tag{3.31}$$

Furthermore, the attenuation factor e^{-ks} of radial velocity in Equation (3.21) becomes time-dependent as well, where $k(t,\mathbf{r})$ is changed to

$$\frac{\partial k(t,\mathbf{r})}{\partial t} = -\mathrm{L}k(t,\mathbf{r})c_{\mathrm{en}}(t,\mathbf{r}). \tag{3.32}$$

Analogously, the $k^{n+1}(\mathbf{r})$ is updated by

$$k^{n+1}(\mathbf{r}) = k^n(\mathbf{r}) - \mathrm{L}k^n(\mathbf{r})c_{\mathrm{en}}^n(\mathbf{r})\Delta t. \tag{3.33}$$

To locate each T-lymphocyte and to determine where they are at time t if they are in the desmoplastic ECM region, we compute the angle of the line segment between cell position and the center $(0,0)$ and the horizontal axis by

$$\theta_j = \begin{cases} \operatorname{atan}(\frac{y_j}{x_j}), & \text{if } y_j \geq 0 \\ \pi + \operatorname{atan}(\frac{y_j}{x_j}), & \text{if } y_j < 0 \end{cases}, \quad \text{for } j \in \mathbb{T}(t), \quad \text{if } R_1 < \| \mathbf{r}_j \| < R_2. \tag{3.34}$$

For each subdomain, the angle is $\frac{2\pi}{N}$ and the j-th subdomain has a range of angles given by

$$\theta_j \in [(j-1)\cdot\frac{2\pi}{N}, \quad j\cdot\frac{2\pi}{N}], \quad \text{for } j \in \{1,\ldots,\mathrm{N}\}. \tag{3.35}$$

3.2.7. MONTE CARLO SIMULATIONS

One of the advantages in our model is the efficiency in computational time, therefore we carry out Monte Carlo simulations to quantitatively investigate the propagation of uncertainties in the parameters. Parameters are sampled from a normal distribution $N(\mu,\ \sigma^2)$, where μ and σ denote the mean value and the standard deviation. The investigated variable $X \in \{F, D, \beta, k\}$ is given by

$$X \sim \mu + \sigma N(0,1). \tag{3.36}$$

Each simulation is terminated at 80 h or 150 h, then we investigate the final fraction of cancer cells f_c as an evaluation criterion for cancer development. Afterward, the sample correlation coefficient ρ between variables and the final fraction of cancer cells f_c reads as

$$\rho = \frac{\sum\limits_{j=1}^{N_s} (X_j - \bar{X})(f_c^j - \bar{f}_c)}{[\sum\limits_{j=1}^{N_s} (X_j - \bar{X})^2 \sum\limits_{j=1}^{N_s} (f_c^j - \bar{f}_c)^2]^{\frac{1}{2}}}. \tag{3.37}$$

In Equation (3.37), $\bar{X}$ and $\bar{f}_c$ represent the average values. Note that the linear sample correlation coefficient ranges in $[-1,\ 1]$.

3.3. NUMERICAL RESULTS

Since we have not yet access to clinical data, we estimate the input parameters based on the range of data provided in the references, which are listed in Table 3.1. Furthermore, we use mathematical intuition to approximate some of the parameters not available in the literature, e.g. diffusivity of enzyme PEGPH20, which is a kind of protein and its value refers to a study with a range of diffusion coefficients of proteins [161]. Moreover, the elasticity of T-lymphocytes is much bigger than the elasticity of epithelial cells, which results in a larger repulsive force if T-lymphocytes mechanically collide with other cells. Since variations of some parameters may have a significant impact on the numerical results, Monte Carlo simulations are carried out to evaluate the uncertainties and correlations among variables, as well as the likelihood that cancer develops up to a prescribed extent. For a couple of parameters, we use sampling from a normal distribution, see Table 3.2 for details.

3.3.1. T-ISLETS WITH ANISOTROPIC DESMOPLASTIC ECM AND MONTE CARLO SIMULATIONS

Pancreatic ductal adenocarcinoma is notorious for the extensive and stiff desmoplasia surrounding the tumor, which is thought to be rare in other types of can-

Table 3.1: Input values

Parameter	Notation	Value and Units	Source
Radius of cells	R	8 μm	[162]
Radius of T-lymphocytes	R_t	5 μm	Estimated
Cell contraction force	F	30 kg $\cdot\,\mu$m/h^2	Estimated
Substrate elasticity	E_s	5 kg/μm $\cdot$ h^2	Estimated
Cell elasticity	E_c	0.5 kg/μm $\cdot$ h^2	Estimated
Elasticity of T-lymphocytes	E_t	250 kg/μm $\cdot$ h^2	Estimated
Cell mobility coefficient	β	60 h^{-1}	Estimated
Friction coefficient	μ	0.2	[41]
Cytokine diffusivity	D_c	5E3 μm^2/h	[163]
PEGPH20 diffusivity	D_{en}	1E1 μm^2/h	[161]
Drug diffusivity	D_{drug}	1E4 μm^2/h	[164]
Secretion rate	γ	5E6 mol/h $\cdot\,\mu$m^3	[165]
Injection rate	γ_0	5E6 mol/h $\cdot\,\mu$m^3	Estimated
Time step	dt	0.01 h	Estimated
Inner radius of T-islet	R_1	120 μm	Estimated
Outer radius of t-islet	R_2	200 μm	Estimated

Table 3.2: Mean and standard deviation in the Monte Carlo simulation sampling

Parameter	F	D	β	Inhibitor k
Value	$(30, 3^2)$	$(5E3, (5E2)^2)$	$(60, 6^2)$	$(0.3, 0.1^2)$

cers. Most studies have shown that this abnormal desmoplasia facilitates cancer initiation, survival and further metastasis [132, 166].

In our previous chapter [92], we develope a cell-based model to describe the influence of anisotropic desmoplasia on the locomotion of T-lymphocytes. Due to the stiffness and anisotropy of the desmoplastic ECM, T-lymphocytes likely become trapped in the desmoplasia area and then preferably move in the direction of the fiber arrangement. Bougherara *et al.* [157] demonstrate that the distribution and migration of T-lymphocytes rely on the density and orientation of collagen fibers.

Since a chemotherapeutic drug administration cycle is typically one week, we restrict each simulation to 150 h. To make the problem tractable, we assume that the density of the collagen is uniform everywhere and that initially its arrangement is parallel to the T-islets circumference. Several consecutive snapshots of the numerical simulation are shown in Figure 3.3, where epithelial cells, cancer cells, T-lymphocytes and anisotropic collagen are visualized by blue, red, black and grey colors, respectively. Due to the guide of the anisotropic orientation Ψ, T-lymphocytes tend to accumulate in a certain area where the cancer cells secrete chemokine is maximal in the stromal layer. The tangential oriented ECM makes T-lymphocytes unable to reach cancer cells. As a result, the proportion of cancer cells of the total cells increases significantly within T-islets. Our result is consistent with experimental observations in a study by Bougherara *et al.* [157] on non-small cell lung cancer and ovarian cancer, where T-lymphocytes preferentially accumulate in the stroma rather than infiltrating into the cancer nest.

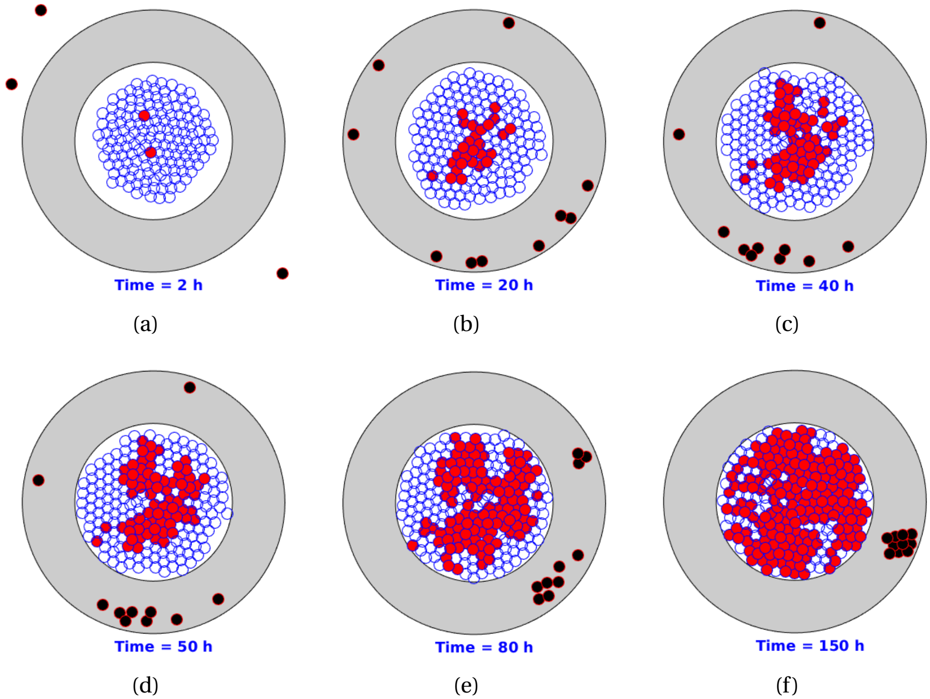

(a) (b) (c)

(d) (e) (f)

Figure 3.3: Snapshots of T-islets with desmoplastic ECM orientation. The epithelial cells, cancer cells, T-lymphocytes and anisotropic collagen are visualized by blue, red, black and grey colors, respectively.

To investigate the influence of input parameters on simulated results, Monte Carlo simulations are carried out, where input variables are sampled from statistical distributions, e.g. normal, uniform, Pareto, lognormal, exponential, etc.[167]. To guarantee an acceptably small error, 5000 samples are used for the cell contraction force F, cytokine diffusivity D_c, cell mobility coefficient β and desmoplastic ECM inhibitor k. For the sake of saving computational time while ensuring that the results are not affected, we consider 80 h.

In Figure 3.4, we plot a histogram of 5000 samples for the fraction of cancer cells at the final time of the simulation f_c and a cumulative distribution function (CDF) of the estimated probability that f_c is lower than a certain number on the horizontal axis. As an example, the proportion of the cases where f_c is no more than 50%, is approximately 51%. The probability rate of cell division, mutation and death in Equation (3.17) is 100/h such that mutation happens during the interval of a time step in each simulation with a probability 0.63. For smaller probability rates for the mutation, we observed several cases in which no mutation, that is, no cancer, occurred. Moreover, this figure shows that most cases end with a large number of cancer cells as a result of ineffective T-lymphocytes infiltration.

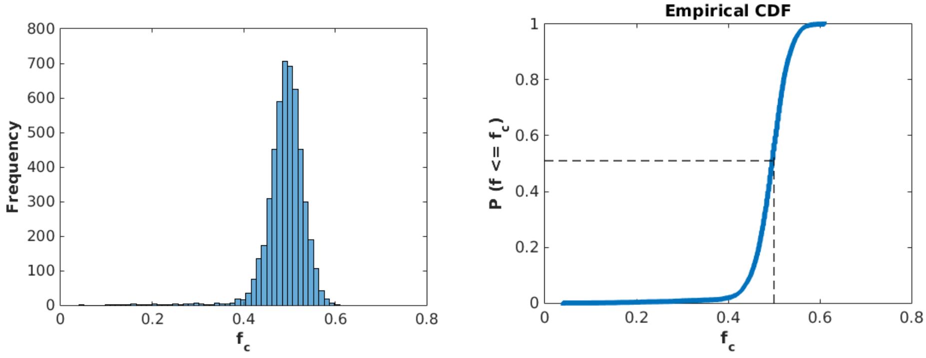

(a) (b)

Figure 3.4: Histogram and CDF plot of outcomes at time of Monte Carlo simulations with 5000 samples. (a) there is no drug intervention. The x-axis shows the final fraction of cancer cells in total cells f_c and the y-axis is its corresponding frequency of occurrence. (b) cumulative probability $f < f_c$ based on the histogram in Figure 3.4(a), where f is the dynamic fraction of cancer cells at time.

Subsequently, several scatter plots are listed in Figure 3.5 showing the sample correlations between each input parameter with the estimated fraction of cancer cells f_c. In comparison, significant impacts of the desmoplastic ECM inhibition k (in particular for small values) and cell contraction force F on f_c, cannot be excluded, where other two variables, i.e. cytokine diffusivity D_c and cell mobility β, have no obvious correlations with f_c. As expected, cancer cells grow and divide within T-islets protected by the anisotropic desmoplastic ECM with influence from input parameters. The radical inhibition of the desmoplastic ECM becomes stronger as the desmoplastic ECM inhibition factor k increases and thereby the fraction f_c becomes relatively large. Note that there is a dramatic increase between 0 and 0.15, which means that the migration of T-lymphocytes is highly sensitive to the accumulation of HA, collagen, fibroblast and etc. in the early stages.

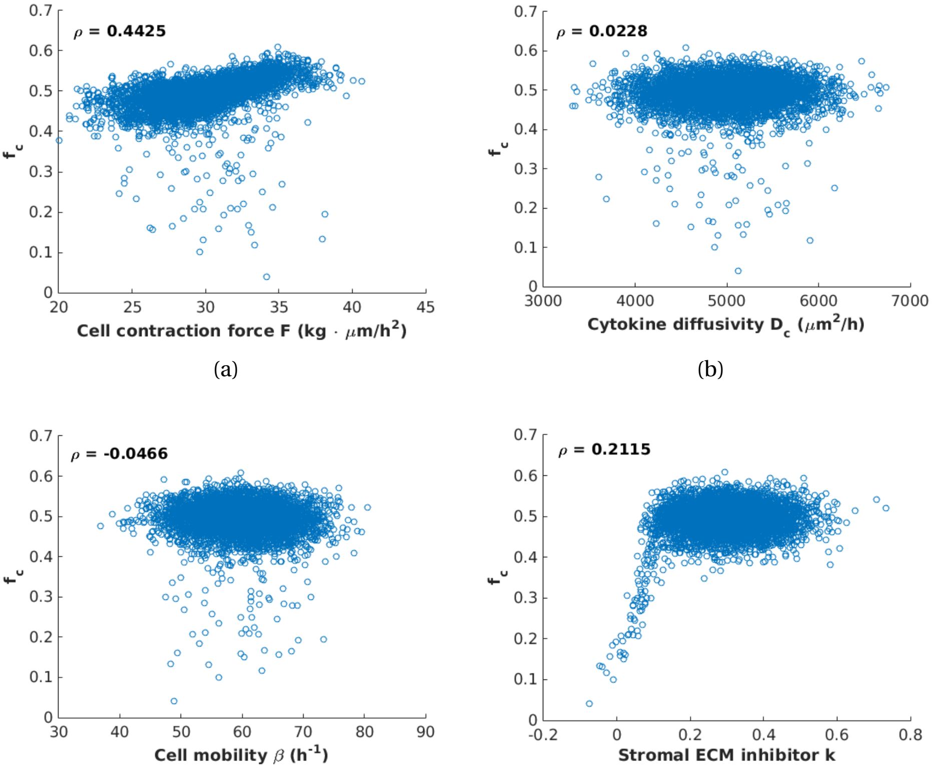

(a) (b)

(c) (d)

Figure 3.5: Scatter plots of the final fraction of cancer cells f_c at time = 80 h versus parameters F, D_c, β and k, respectively. The ρ in each subfigure corresponds to its correlation coefficient. In comparison, (d) exhibits a significant correlation between f_c and the desmoplastic ECM inhibition faction k from 0 to 0.15.

3.3.2. PEGPH20 INJECTION

Accumulated HA functions as a core polymer of the cancer-associated ECM to provide a hydrated viscoelastic gel-like matrix in collagenous fibers, and forms the main barrier to chemotherapy delivery and vasculature [168, 169]. PEGPH20 is a type of enzyme aiming at depleting abundant HA in the anisotropic desmoplastic ECM to improve vascular perfusion and to increase the effectiveness of anti-cancer therapeutics. Thompson *et al.* [168] describe their experiments showing that PEGPH20 has an ability to remove the accumulated HA as well as to remodel the tumor microenvironment. Thence we propose a simplified enzymatic depletion model of tumor stroma with PEGPH20 intervention to predict the interaction of cancer cells and its microenvironment.

To evaluate the variations of ECM orientation in different areas in Figure 3.1(b), the modeled anisotropic stroma is divided into 10 subdomains in Figure 3.2(b). Each center of subdomains acts as a point to monitor the concentration of PEGPH20 that results in ten different concentration signals. Typically, PEGPH20 is given by intravenous injection in clinical trials while experimentally cell lines in vitro are fed with PEGPH20 in culture cell media. To develop a simplified model, we suppose that the injection site is just outside T-islets near subdomain 5. Normally when patients have any symptoms, the pancreatic cancer is already in advanced or late stages, which poses a challenge for the improvement of the prognosis. Since the model is developed for the early stage, we suppose that a high concentration of PEGPH20 is given when the number of cancer cells accounts for 35% of the total number marked as time t_0. The injection lasts 1 h to time t_1 and attenuation of ECM orientation on T-lymphocytes migration within 10 subdomains is shown in Figure 3.6. The orientation degree λ_2 of subdomains is set to ten initially and subsequently decays during the time interval $(t_0,\ t_1)$, respectively, where the area near the injection site decays faster. Thereby the T-lymphocytes in the PEGPH20-treated subdomains move faster in the radial direction at the beginning compared with in the rest subdomains. Note that eventually the orientation of the ECM has no significant influence on T-lymphocytes migration.

Some consecutive snapshots are shown in Figure 3.7 in which pancreatic cancer starts with epithelial cell mutation and triggers an immune response afterward. With ECM orientation, T-lymphocytes are trapped in peripheral ECM. After PEGPH20 is injected, T-lymphocytes are no longer hindered by the anisotropic desmoplastic ECM orientation in the solid stromal region, and finally invade into the interior of the T-islets. However, the fraction of cancer cells remains stable in Figure 3.7 when t = 150 h despite that the immune responses are boosted, since the cancer cells keep dividing without drug intervention. Therefore, drugs or antibodies are crucially important to fight uncontrolled cell division or to enhance the efficiency of the immune responses.

3.3.3. PEGPH20 + GEMCITABINE INJECTION

The aberrant desmoplasia is a result of activated pancreatic stellate cells which lead to the production of collagen, laminin and fibronection [170]. As a conse-

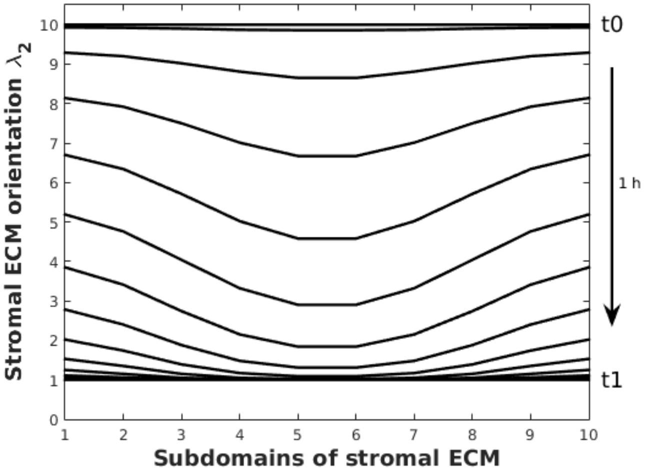

Figure 3.6: Variation of λ_2, which is the tangential component of desmoplastic ECM orientation, in ten subdomains (see Figure 3.2(b)) during time interval (t_0, t_1). Since the injection site of PEGPH20 is chosen at the middle of subdomain 5 and 6, but outside of the desmoplastic ECM, the orientation λ_2 of subdomain 5 and 6 decrease faster as a result of sensing a higher PEGPH20 concentration.

quence, cancer stroma exhibits abundant HA, increased stiffness and elevated hydrostatic pressure which collaborate to suppress the intratumoral drug delivery [133]. With the enzymatic depletion of HA in the stromal region, the interstitial fluid pressure, which restores the vessel appearance and drug delivery into the carcinoma, decreases. Provenzano *et al.* [133] experimentally study the combinations of enzyme PEGPH20 and drug gemcitabine for the treatment of pancreatic cancer in the mice. To provide more predictions and possibilities, we develop a PEGPH20 + gemcitabine model for the treatment of pancreatic cancer.

Gemcitabine is the first-line drug for pancreatic cancer, which inhibits processes required for DNA synthesis and causes cell death [147]. In our earlier chapter, the probabilistic division of cancer cells can happen under the following conditions: 1) sufficient time interval for growth; 2) suitable strain energy density. We assume that the probability rate during a time interval remains unchanged for cell mutation, division and death. Since the drug impedes cancer cell proliferation, we hypothesize that the probability rate λ of cell mutation and cancer division depends on the concentration of gemcitabine $\lambda = \lambda(c(t))$. In the simulations, drug injection (indicated by a red filled square) lasts 1 h such that the concentration of gemcitabine increases during an hour and subsequently goes down. Consequently, the probability of mutation and division of cancer decreases and then the T-lymphocytes are more likely to eliminate cancer cells. The

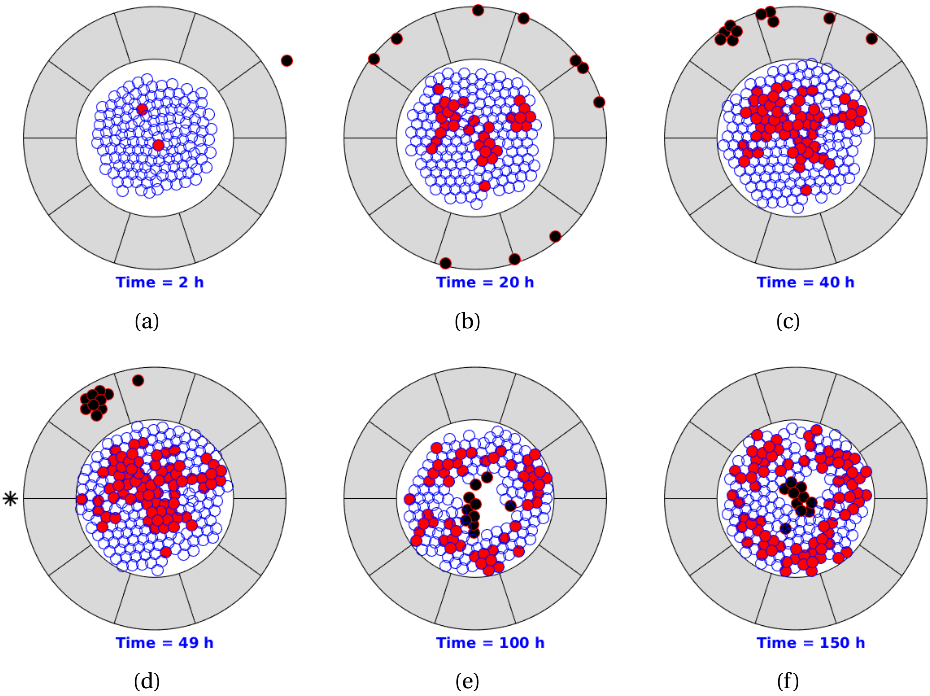

(a) (b) (c)

(d) (e) (f)

Figure 3.7: Snapshots of T-islets with PEGPH20 intervention. The epithelial cells, cancer cells, T-lymphocytes and anisotropic ECM are visualized by blue, red, black and grey colors, respectively. Moreover, the black asterisk is visualized as an injection site. Before PEGPH20 intervention, T-lymphocytes are trapped in peripheral ECM and accumulate in a certain area as a result of cancer-mediated chemotaxis and ECM orientation.

resulting behaviors are shown by some snapshots in Figure 3.8, where PEGPH20 is injected around t = 45 h. Due to the stochastic nature of the model, each simulation varies from others and thereby the injection time changes with t = 49 h in Figure 3.7 and t = 45 h in Figure 3.8. Therefore we vary the fraction of cancer cells when injecting PEGPH20/ PEGPH20 + gemcitabine. The injection point is visualized as a black asterisk and 10 h later [135], gemcitabine is administered. Compared to Figure 3.8, the final fraction of cancer cells f_c is much smaller in Figure 3.8 at t = 150 h, which means that the combination of PEGPH20 + gemcitabine is more effective than the use of PEGPH20 only in order to facilitate concurrent immune response and chemotherapy.

In animal-based experiments, the size of a solid pancreatic tumor has been compared before and after the combined treatment, respectively [133]. We alternatively compare the fraction of cancer cells f_c in T-islets before and after treatment, for simplicity of calculation. Figure 3.9 shows the comparison of f_c

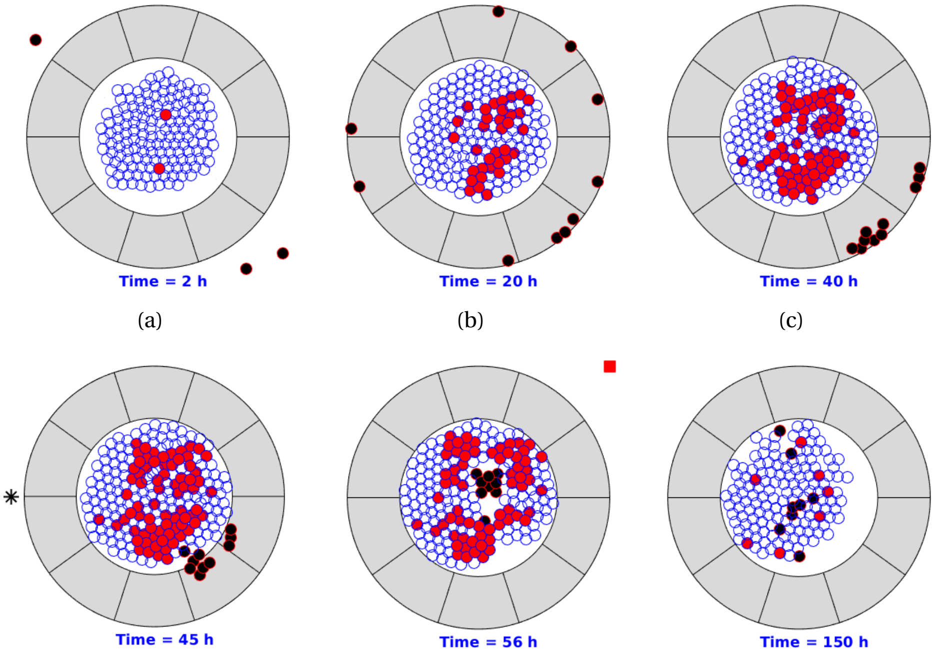

(a) (b) (c)

(d) (e) (f)

Figure 3.8: Snapshots of T-islets with intervention of PEGPH20 + gemcitabine. The epithelial cells, cancer cells, T-lymphocytes and anisotropic collagen are visualized by blue, red, black and grey colors, respectively. Moreover, the black asterisk is visualized as PEGPH20 injection site and the red filled square denotes gemcitabine injection site. Before PEGPH20 intervention, T-lymphocytes are trapped in peripheral ECM and accumulate in a certain area as a result of cancer-mediated chemotaxis and ECM orientation.

in T-islets with PEGPH20 intervention only and with combined PEGPH20 + gemcitabine, respectively. Each simulation is restricted to 150 h, where PEGPH20 is given once, the initial cancer cell proportion is 35% and gemcitabine is injected 10 h later in the combined treatment referring to [135]. In Figure 3.9(a), the number of cancer cells increases to the maximum capacity of the modeled T-islets (approximately 250 in the current simulation domain) because T-lymphocytes are trapped in the desmoplastic ECM area. With early PEGPH20 intervention, T-lymphocytes are capable of penetrating the enzyme-depleted ECM to engulf cancer cells and thereby the fraction of cancer cells slightly drops firstly and then gradually rebounds into a growing trend towards roughly 42% in the end. Next, the combined PEGPH20 + gemcitabine is considered, as we expected, only a few cancer cells are finally left with a fraction of 11% after 150 h.

Aside from physical barriers, the influence of the injection time of PEGPH20/

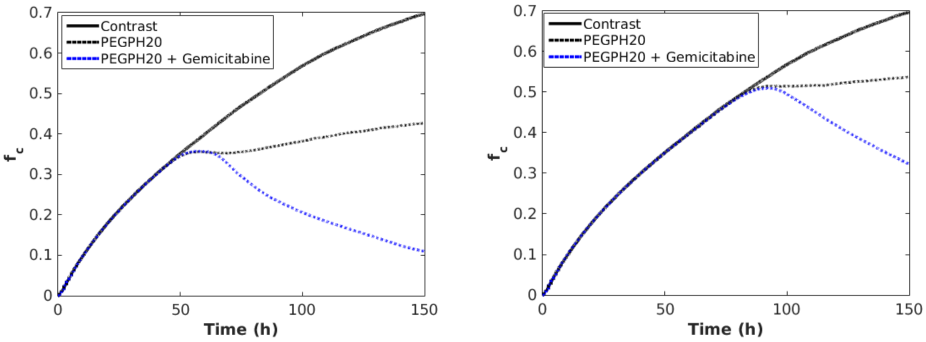

(a) (b)

Figure 3.9: Comparisons of the final fraction of cancer cells f_c during 150 h evolution in T-islets for three cases. Three cases are: without treatment, with PEGPH20 alone and with PEGPH20 + gemcitabine, respectively. (a) treatment starts as soon as the fraction of cancer cells is 35%. (b) treatment starts as soon as the fraction of cancer cells is 50%.

PEGPH20 + gemcitabine on the progression of cancer is crucially important. If the injection time is delayed until the cancer cells have accounted for 50% of the total cells, the corresponding result is shown in Figure 3.9(b). In terms of the final proportion of cancer cells f_c, the PEGPH20 alone could restrict the fraction of cancer cells with a dynamic equilibrium for a short period. Furthermore, the follow-up progression of cancer depends on the patient's own immune response. Whereas, PEGPH20 + gemcitabine could control the fraction of cancer cells to some extent due to the functions of the drug. The model predicts roughly a fraction of 31% when t = 150 h, see Figure 3.9(b), where probably more PEGPH20 + gemcitabine is needed for further treatment. During the cancer progression and therapy, the likelihood of cancer metastasis increases over time and thereby personalized therapeutic strategies are necessary, which can benefit from computational modeling.

To investigate the fraction of cancer cells on which the combined treatment starts and the dose of the drug on the final fraction of cancer cells, Monte Carlo simulations are incorporated with 5000 samples. Note that a dose of the drug is calculated by $\gamma_{\text{drug}} \times \tau$, where γ_{drug} is a constant injection rate and τ is a time interval. Therefore, the initial fraction of cancer cells when starting treatment as well as the time interval τ are sampled from a normal distribution with $(0.5, 0.1^2)$ and $(2, 1^2)$ h, respectively. The result in Figure 3.10 shows a three dimensional scatter plot of the initial fraction of cancer cells when starting treatment, injection time interval and the final fraction of cancer cells f_c, where a horizontal color bar specifies the final fraction of cancer cells. If we aim that f_c does not exceed

20% in the pancreatic T-islets, the fraction of cancer cells at which the treatment is started when injection PEGPH20 + gemcitabine should never be larger than 40%. Hence if this fraction exceeds 40%, then f_c will never be lower than 20% after 150 h. By applying Equation (3.37), the sample correlation coefficient of fraction at which the treatment is started and f_c equals $\rho = 0.8785$. This result gives the prediction about the likelihood of a cure for specific patients after combining these two drugs. Probably other therapies should be incorporated in if a patient is diagnosed at very late stages, or treatments should last longer.

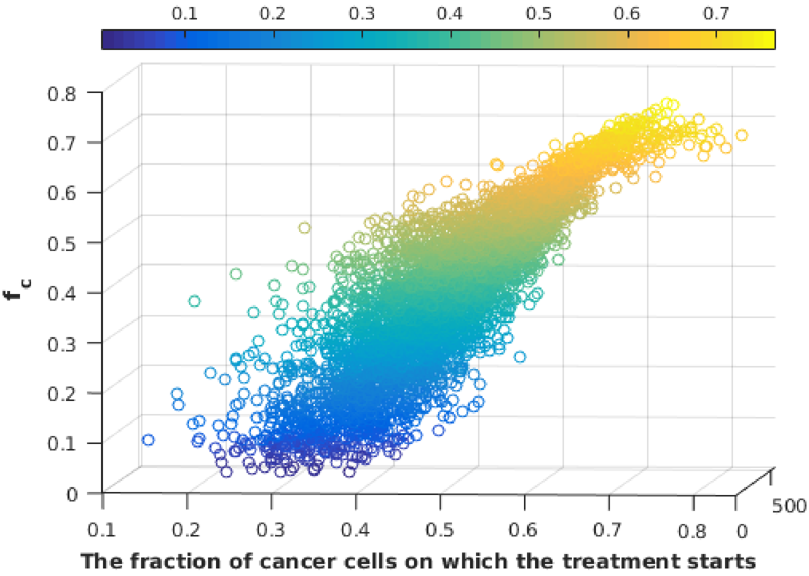

Figure 3.10: A three dimensional scatter plot of fraction of cancer cells f_c at which the treatment is started, injection time interval and final fraction of cancer cells. The color bar indicates the final fraction of cancer cells. Blue colors indicate low final fractions of cancer cells, whereas yellow colors indicate high fractions of cancer cells. Hence blue colors are favorable, whereas yellow colors are not.

Subsequently, Figure 3.11 shows correlations between the injection time interval and the final fraction of cancer cells f_c under various treatment times. It hints that within our chosen range there is an obvious influence with a correlation coefficient $\rho = -0.2753$ of doses of the drug on the final results. In other words, big doses of drugs are necessary if the treatment starts when the fraction of cancer cells exceeds 40%. Furthermore, the potential consequences are divided into two parts by a dashed line, where the likelihood of cure in the left side is higher, whereas the right side means a high risk of malignant cancer and probably metastasis. Taking the toxicity of the drug into consideration, large drug doses could be problematic for other parts of the body, and we think that this model is good for making choices of drug dosage.

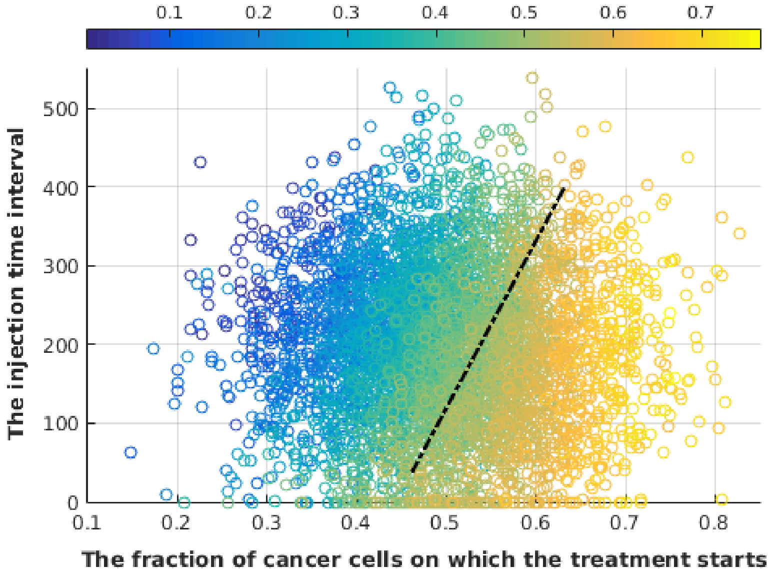

Figure 3.11: Scatter plot of the fraction of cancer cells on which the treatment starts, injection time interval and final fraction of cancer cells. Blue colors indicate low final fractions of cancer cells, whereas yellow colors indicate high fractions of cancer cells (see color bar). Hence blue colors are favorable, whereas yellow colors are not. A dashed black line is used to divide the potential consequences into two parts, where the likelihood of cure in the left side is higher, whereas the right side part hints a high risk of malignant cancer and even metastasis.

3.4. CONCLUSION AND DISCUSSION

Pancreatic cancer is a lethal disease mainly due to late diagnosis, low resection rate, high recurrence, metastasis and chemotherapy resistance. Unfortunately, there is currently no standard program for screening patients who have a high risk [171]. Combined with surgical resection, cytotoxic therapy plays an essential role in the standard treatment and in the prolongation of survival of pancreatic cancer. The front-line therapies normally involve the administering of gemcitabine combined with other drugs like cisplatin, epirubicin, 5-FU, etc. For a review of therapeutic strategies we refer to [172]. However, the increased toxicity and various ethical concerns hinder the investigation and clinical administering of single and combined drugs. Mathematical modeling can shed light on the quantitative effects of drug combinations as well as provide reliable predictions.

We have developed a model for drug-oriented therapy of pancreatic cancer based on the simplification of the phenomenon and assumptions mentioned in Section 3.2. On the cellular level, our model is able to show the initial cancer progression and its interactions with the micro-environment. The normal epithelial cells are able to mutate to cancer cells under certain circumstances, which subsequently remodels the peripheral ECM and triggers T-lymphocytes-mediated immune response by secreting cytokines. In normal situations, the migration of the T-lymphocytes is guided by the desmoplastic ECM such that cancer cells in the T-islets can proliferate out of control because of lacking T-lymphocytes infiltration. After a PEGPH20 intervention, the enzyme-mediated degradation of ECM enhances T-lymphocytes penetration and thereby the cancer cells that are exposed to be T-lymphocytes are eliminated, however, this enzyme-mediated therapy is suitable for patients with an early diagnosis without immunodeficiency. For patients with advanced diagnosis, it is necessary to combine PEGPH20 with the drug gemcitabine, which is much more efficient for clearing the cancer cells. Additionally, this cell-based model could be upscaled to a large cell colony or even an organ scale, while the time at which the treatment starts, as well as the length of the time period of administration of different therapies can be personalized.

Furthermore, Monte Carlo simulations facilitate our model to investigate the uncertainties of input parameters and to predict the likelihood of a cure with various diagnosis stages. As a conclusion, the initial fraction of cancer cells when injecting the PEGPH20 has a significant sample correlation coefficient as high as 0.8785 with the final fraction of cancer cells. In contrast, sufficient doses of drugs could reduce the final fraction of cancer cells in the current model with a sample correlation coefficient -0.2753. In summary, this therapy model is able to aid design the drug administering in the experiments. Further, the model can be extended to other therapy strategies like PEGPH20 + antibodies, PEGPH20 + cancer-targeted virus, PEGPH20 + cancer-targeted drugs, etc.

Albeit the computational models have their drawbacks like being too simplified, the mathematical modeling can be very helpful for the sake of prediction. For instance, Enderling *et al.* [31, 52] develop models of breast cancer that are beneficial for radiotherapy. Moreover, [53] propose a mathematical model which is helpful to prostate cancer therapy. On the other hand, animal-based experiments have moral concerns and systemic drugs normally have toxicity and strict restrictions regarding administering. Therefore, mathematical models can be used to optimize drug therapies and further perform pre-validation studies before testing in animals or humans.

4

A CELLULAR AUTOMATA MODEL OF ONCOLYTIC VIROTHERAPY IN PANCREATIC CANCER

Oncolytic virotherapy is known as a new treatment to employ less virulent viruses to specifically target and damage cancer cells. This chapter presents a cellular automata model of oncolytic virotherapy with an application to pancreatic cancer. The fundamental biomedical processes (like cell proliferation, mutation, apoptosis) are modeled by the use of probabilistic principles. The migration of injected viruses (as therapy) is modeled by diffusion through the tissue. The resulting diffusion-reaction equation with smoothed point viral sources is discretized by the finite difference method and integrated by the IMEX approach. Furthermore, Monte Carlo simulations are done to assess the correlations between the various input process parameters and the extent of inhibition of cancer and the amount of residual viral particles shortly after the viral treatment.

4.1. INTRODUCTION

Oncolytic virotherapy is a novel cancer treatment where natural or genetically modified viruses infect cancer cells and then self-replicate until host cancer cell lyses (see Figure 4.1). Ruptured cancer cells release chemicals like tumor antigens, which make cancer cells easily recognizable by the immune system. Moreover, the released viruses can infect more cancer cells to trigger a chain reaction and effectively acting as a follow-up treatment. As early as in 1912, De Pace [173]

The contents of this chapter have been submitted.

identified a tumor regression after inoculation of an attenuated rabies vaccine in a patient with uterine cervical carcinoma. Later on, an animal-based test [174] and a human trial [175] were conducted in 1920 and 1940, respectively, where both experiments yielded an obvious partial remission [176]. In the subsequent decades, more works [177–179] demonstrated that oncolytic virotherapy lead to tumor attenuation. Some milestones in the development of oncolytic virotherapy are shown in Figure 5.2 [173, 180–182].

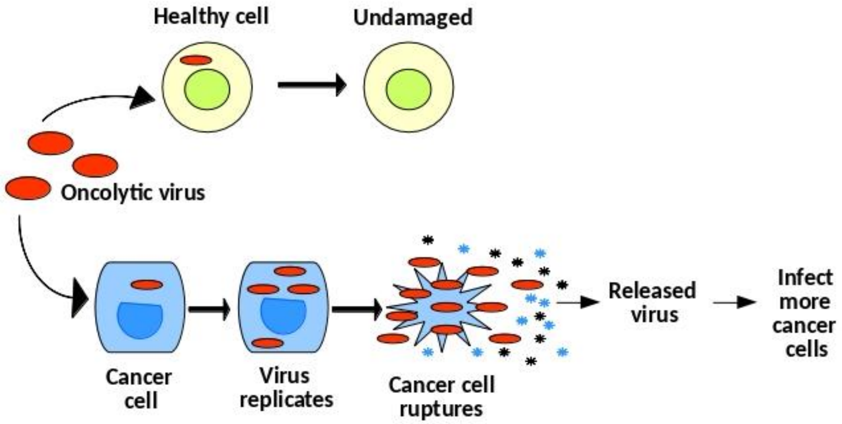

Figure 4.1: A schematical figure of oncolytic virotherapy. The viruses can specifically infect cancer cells and then replicate themselves until cancer cells rupture. Subsequently, the newborn viruses are released to infect more cancer cells.

Pancreatic ductal adenocarcinoma (PDA), recognized as the most common pancreatic cancer, is a lethal disease due to late detection, a low resectability rate, medication resistance and poor prognosis [169, 183]. Currently, pancreatic cancer is the seventh leading cause of cancer death worldwide and its 5-year survival rate is less than 5 % [158, 184]. Compared with other types of cancer, PDA has more cancer-associated fibroblasts (CAFs) resulting in abundantly desmoplasitic stroma that constitutes up to 90 % of a solid tumor volume [146, 185]. The profuse desmoplasia in the stroma produced by CAFs acts as a physical barrier to drug delivery and leads to medication resistance [133, 186]. However, CAFs make cancer cells more susceptible to be infected by oncolytic viruses. Ilkow *et al.* [187] experimentally demonstrated that the cross-talk between cancer cells and CAFs facilitates the oncolytic virus-based therapies. Therefore, oncolytic virotherapy offers an avenue for the cure of pancreatic cancer.

The ideal oncolytic virus for pancreatic cancer should be able to selectively replicate in cancer cells without damaging normal somatic cells (see Figure 4.1).

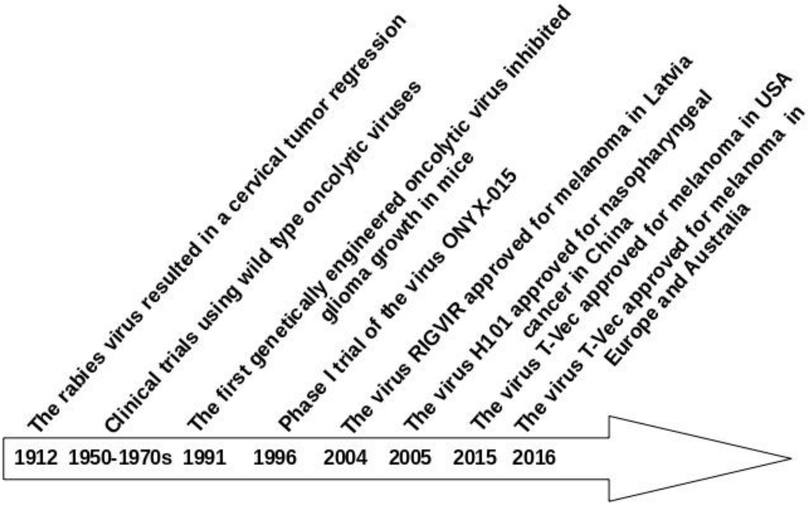

Figure 4.2: Historical milestones in the development of oncolytic virotherapy.

A couple of studies [176, 188, 189] summarised advantages and disadvantages of various replication-competent oncolytic viruses proposed for pancreatic cancer therapies, e.g. adenoviruses, herpesviruses, poxviruses, parvoviruses, reoviruses and paramyxoviruses. Many types of viruses have been tested in animal-based xenograft models, however, only a few kinds of viruses have reached clinical trials. In particular for pancreatic cancer, relevant studies are rare, among which Fu *et al.* [190] observed that an oncolytic virus produced antitumor effects in human pancreatic cancer xenografts. Moreover, Sunamura *et al.* [188] carried out adenovirus therapy in immunodeficient mice with human pancreatic cancer xenografts that resulted in a remarkable inhibition of tumor growth under consecutive injections of the virus. Typically, if animal testing is successful, the new drug will reach clinical trials that are classified into four phases: 1) phase I determines on healthy subjects if a new drug is safe to check the efficacy; 2) phase II demonstrates whether a drug can have any efficacy against the disease; 3) phase III checks in a randomized multi center tests if a drug has the right therapeutic effect; 4) phase IV post-marketing surveillances long-term effects of a drug. Regarding the clinical applicability, Kasuya *et al.* [176] stated that a clinical trial of viruses adenovirus ONYX-015 (phase I and II) has been conducted in pancreatic cancer patients, where half of the patients (phase II) exhibited either tumor reduction or stabilization. In contrast, a phase I trial of the efficacy of several oncolytic herpes viruses (such as G207, 1716 and OncoVEX GM-CSF) have tested against various tumors and the herpesvirus exhibited a good tolerance at all dosages. Although oncolytic virotherapy has been proposed for decades, a thorough understanding of the interactions of virus, tumor and microenvironment in vivo is still needed to be further researched, like a proper viral dose for a specific virus, how to control of virulence and etc. Therefore we develop a three-dimensional (3D) mathematical Markov Chain cellular automata model to mimic pancreatic tumor (pancreatic cancer at early stages) progression and corresponding oncolytic virotherapy. The model presents the cancer progression and the subsequent recession under the interference of oncolytic viruses. In additon, the model can be used to quantify the impact of virotherapy with different viral doses, viral infectivity and levels of immunity in patients with pancreatic cancer.

Cellular automata models are lattice-based models that facilitate analysis of the spatio-temporal dynamics based on the interplay between cells and their microenvironment. The cellular automata model has been introduced as a computer model of self-reproduction by John von Neumann and Stanislaw Ulam [191]. In the past decades, cellular automata, in addition to self-reproduction, have been extended to other model applications successfully with a wide spectrum of biology, physics, chemistry and other sciences [192]. Regarding the cancer modeling in cellular automata, Reis *et al.* [193] proposed a model that could capture the Gompertzian behavior of tumor growth. Hatzikirou and Deutsch [194] developed a model of tumor invasion dynamics. In addition, a couple of studies demonstrated applications of cellular automata in cancer therapy, e.g. radiotherapy [195], and chemotherapy [196]. However, the computational models for virotherapy are rare. Presently, no virotherapy model with an application to pancreatic cancer has been reported yet.

Therefore, we develop a cellular automata model to phenomenologically show cancer initiation and its subsequent recession under oncolytic virotherapy. Furthermore, the 3D model of pancreatic cancer is combined with Monte Carlo simulations to quantitatively investigate the sensitivity and uncertainties of input values.

4.2. MATHEMATICAL FORMALISM

Cellular automata models consist of a class of lattice-based models, where lattice approaches are classified as: 1) a single lattice site is occupied by one cell only; 2) a single lattice site is occupied by a cluster of cells; 3) one cell takes many lattice sites. They are all capable of investigating biological processes with single cell or multiple cells, where division, death or other biomedical phenomenons are modeled by stochastic processes [72]. In contrast, the first two categories are typically used to describe volume effects, whereas the last category is able to capture the morphological evolution of cells.

In our simulations, each lattice represents a volume element filled with multiple cells in a 3D computational domain $\Omega \subset \mathbb{R}^3$, which is divided into a set of lattice points $N = \{1, \dots, n\}$. The lattice point i has a finite number of discrete states S_i that indicates the state of cells in the corresponding volume, which reads as

$$S_i = \begin{cases} 0, & \text{lattice point } i \text{ is in unoccupied state/ necrotic cancer cell state} \\ 1, & \text{lattice point } i \text{ is in epithelial cell state} \\ 2, & \text{lattice point } i \text{ is in cancer cell state} \\ 3, & \text{lattice point } i \text{ is in infected cancer state} \end{cases} . \tag{4.1}$$

Assigning an initial state for each lattice point, and subsequently adjusting the state of the specified lattice at position $\mathbf{x}_i = [x_i, y_i, z_i]$ at subsequent times is correlated with the states of its neighborhood marked in Figure 4.3. Subsequently, we consider fundamental biological processes like cell division, mutation, infection and death modeled as stochastic processes. The likelihood of changing a state of a lattice i to another state satisfies a memoryless exponential distribution which is given by $f(\lambda_i, t)\Delta t$ during a time period $(t_0, t_0 + \Delta t)$. Here λ_i is the probability rate per unit of time of changing state, which from a biological point is determined by mechanisms like cell division, mutation, infection and death, and $f(\lambda_i, t)$ reads as,

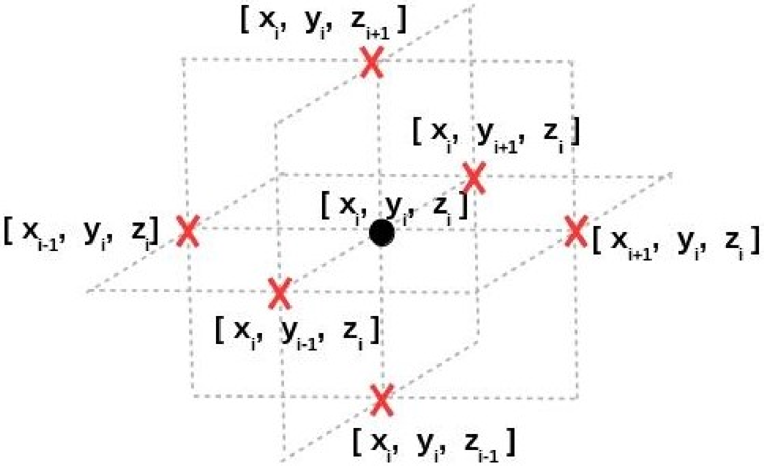

Figure 4.3: A specified lattice point i at position $\mathbf{x}_i = [x_i, y_i, z_i]$ with its neighborhood in the 3D simulations.

$$f(\lambda_i, t) = \lambda_i \exp(-\lambda_i(t - t_0)), \tag{4.2}$$

and hence the transition probability P within a time interval of length Δt is given by

$$P = \int_{t_0}^{t_0+\Delta t} f(\lambda_i, t)\mathrm{d}t \simeq 1 - \exp(-\lambda_i \Delta t). \tag{4.3}$$

In [197], it is proved that the likelihood of a change of state depends on the states of the neighbors for a simple binary case that has been applied to modeling the progression of skin cancer. All lattice points in the domain are initialized to the epithelial cell state $\{S_i = 1\}$ or unoccupied state $\{S_i = 0\}$. During the growth of epithelial cells, cancer mutation happens as a result of exposure to carcinogenic factors like genetic inheritance, chemical carcinogens, electromagnetic radiation, or viral infection. The very complicated biological process is simplified by the application of a transition probability from epithelial cells to cancer cells, that is from $\{S_i = 1\}$ to $\{S_i = 2\}$ (cancer cell) over a time interval Δt with a likelihood following

$$\begin{cases} P(S_i(t_0 + \Delta t) = 2 \mid S_i(t_0) = 1) \simeq 1 - \exp(-\lambda_{\mathrm{mu}} \Delta t) \\ P(S_i(t_0 + \Delta t) = 1 \mid S_i(t_0) = 2) = 0 \end{cases}. \tag{4.4}$$

Here λ_{mu} represents the mutation probability rate per unit of time and the second part of Equation (4.4) reflects that this transition is irreversible. Since both epithelial cells and cancer cells are able to proliferate and to migrate, lattice points are allowed to change their states from $\{S_i = 0\}$ to $\{S_i = 1, 2\}$. The likelihood for these transitions over a time interval Δt are given by

$$P(S_i(t_0 + \Delta t) \in \{1, 2\} \mid S_i(t_0) = 0) \simeq 1 - \exp(-\lambda_{\mathrm{pro}} \Delta t), \tag{4.5}$$

where λ_{pro} denotes the probability rate of transition from 'not occupied by any cells' to being 'occupied by either epithelial cells or cancer cells'. Note that the probability rate λ_{pro} is determined based on the number of neighbors that are in cancer/ epithelial cell state. That is $\lambda_{\mathrm{pro}} = \lambda_{\max} \frac{n_{12}}{h}$, where n_{12} denotes the number of lattice points that are either in state 1 or in state 2. The distance between two lattice points is represented by h and $\lambda_{\max}$ is a constant to regulate the overall growh rate of cells (including epithelial and cancer cells). Whether a free lattice point will be occupied by multiple epithelial cells or cancer cells depends on the states of the surrounding lattice points. Consider an unoccupied node i at time t, that is $S_i(t) = 0$. We denote the number of neighboring lattice points that are in state 1 by n_1. We further denote the likelihood that the lattice point i, given that it changes state to either state 1 or 2, changes state to state 1 by $\alpha = \alpha_0 \cdot \frac{n_1}{n_{12}}$, where $\alpha_0 \in [0, 1]$ is a constant. This fraction α is used to determine the transition probability of node i, which is given by

$$\begin{cases} P(S_i(t_0 + \Delta t) = 1 \mid S_i(t_0) = 0) = \alpha P(S_i(t_0 + \Delta t) \in \{1, 2\} \mid S_i(t_0) = 0) \\ P(S_i(t_0 + \Delta t) = 2 \mid S_i(t_0) = 0) = (1 - \alpha) P(S_i(t_0 + \Delta t) \in \{1, 2\} \mid S_i(t_0) = 0) \end{cases}. \tag{4.6}$$

Apoptosis is programmed death of cells, however, cancer cells are able to proliferate uncontrollably and to resist cell apoptosis. In the current model, oncolytic viruses are incorporated to infect and damage cancer cells. We let cancer cells jump from state $\{S_i = 2\}$ (cancer state) to state $\{S_i = 3\}$ (infected state) as soon as the virus concentration exceeds $\hat{c}$. Hence, we have

$$P(S_i(t_0 + \Delta t) = 3 \mid S_i(t_0) = 2) = 1, \quad \text{if } c_i > \hat{c}, \tag{4.7}$$

If the viral concentration does not exceed the threshold $\hat{c}$, then we disregard the release of viruses. Therefore, the likelihood of a lattice point i to be infected by viruses, which is the state transition from $\{S_i = 2\}$ to $\{S_i = 3\}$, depends on the released viruses from the neighborhood and the local concentration of viruses. Subsequently, infected cells are, like epithelial cells, subject to possible cell death. Hence a node i is allowed to change from a cell state $\{S_i = \{1,3\}\}$ to an unoccupied state $\{S_i = 0\}$, which is given by the following likelihood

$$P(S_i(t_0 + \Delta t) = 0 \mid S_i(t_0) \in \{1,3\}) \simeq 1 - \exp(-\lambda_{\mathrm{de}} \Delta t). \tag{4.8}$$

Here λ_{de} denotes the probability rate that an infected cancer or an epithelial cell dies.

Oncolytic virotherapy is initiated when the fraction of tumor constitutes up to 100 % of the computational domain (that is, the tissue). In animal-based experiments, the viruses are given by injections [188]. Therefore, we consider one or multiple injections, denoted by $\mathbb{V}(t)$, as source points at position $\mathbf{x}_p$ by using the Dirac delta function $\delta(\mathbf{x})$ at time t. Then the delivery of viruses is simulated by the reaction-diffusion equation written as

$$\begin{cases} \frac{\partial c(\mathbf{r})}{\partial t} - D\Delta c(\mathbf{r}) = \sum\limits_{p \in \mathbb{V}(t)} \gamma(t)\delta(\mathbf{x} - \mathbf{x}_p) + u(\mathbf{r}) \\ D\frac{\partial c(\mathbf{r})}{\partial n} + Tc(\mathbf{r}) = 0, \quad \text{on } \partial\Omega \end{cases}, \tag{4.9}$$

where $c(\mathbf{r})$, D and γ denote the concentration, diffusivity and injection rate of virus. Moreover, T represents the mass transfer rate coefficient between the computational domain and its environment. Since viruses infect cancer cells, copy themselves until host cells lysis, infected cancer cells act as sources where viruses originate. We define $\Omega_{ic}(t)$ to denote the portion of the computational domain that is occupied by virally infected cancer cells. The function $u(\mathbf{r})$ in Equation (4.10) is utilized to model an increase in production of viruses released by dead cancer cells. With respect to time evolution, $u(\mathbf{r})$ increases as

$$u(\mathbf{r}) = \begin{cases} \beta c(\mathbf{r})(1 - \frac{c(\mathbf{r})}{N_v}), & \text{if } \mathbf{r} \in \Omega_{ic}(t) \\ 0, & \text{else} \end{cases}, \tag{4.10}$$

where β and N_v denote the proliferation rate of virus and a burst size of viruses from a dead cancer cell.

4.3. NUMERICAL METHOD

4.3.1. DISCRETIZATION

We first consider a 2D or 3D domain that is occupied by cancer cells, where a dose of oncolytic viruses is injected into the computational domain as part of the therapy. Subsequently, viruses diffuse and thereby spread throughout the domain. At a lattice point **r**, the change in concentration of viruses is modeled by the reaction-diffusion equation

$$\begin{cases} \frac{\partial c(\mathbf{r})}{\partial t} = D\Delta c(\mathbf{r}) + \gamma(t)\delta(\mathbf{x}-\mathbf{x}_p) + \beta c(\mathbf{r})(1-\frac{c(\mathbf{r})}{N_v}) \\ D\frac{\partial c(\mathbf{r})}{\partial n} + Tc(\mathbf{r}) = 0, \quad \text{on } \partial\Gamma \end{cases}, \tag{4.11}$$

To solve the problem in 2D, the Laplace operator is discretized by the finite difference method (FDM) as,

$$\Delta c(x,y,t) \simeq \frac{c(x+h,y,t)+c(x-h,y,t)+c(x,y+h,t)+c(x,y-h,t)-4c(x,y,t)}{\mathrm{d}x^2}, \tag{4.12}$$

where h is the distance between adjacent lattice points. If the computational domain is extended to three dimensions, the above equation needs to be revised to

$$\begin{aligned} \Delta c(x,y,z,t) \simeq &\frac{1}{\mathrm{d}x^2}(c(x+h,y,z,t)+c(x-h,y,z,t)+c(x,y+h,z,t)+c(x,y-h,z,t) \\ &+c(x,y,z+h,t)+c(x,y,z-h,t)-6c(x,y,z,t)). \end{aligned} \tag{4.13}$$

If a lattice point on boundary $\Gamma_{x=0}$, then the point $(-h,y,z)$ is assumed as a virtual point out of the computational domain. The Robin boundary condition in Equation (4.11) is dealt with using the FDM as,

$$\frac{c(-h,y,z,t)-c(h,y,z,t)}{2h} = -\frac{T}{D}c(0,y,z), \tag{4.14}$$

and thereby the viral concentration at the virtual point is calculated by,

$$c(-h,y,z,t) = c(h,y,z,t) - c(0,y,z,t)(1-\frac{2T}{D}h). \tag{4.15}$$

Analogously, the viral concentration on the other virtural points can be obtained by

$$\begin{cases} c(x,-h,z,t) = c(x,h,z) - c(x,0,z,t)(1-\frac{2T}{D}h), \text{ on } \Gamma_{y=0} \\ c(x,y,-h,t) = c(x,y,h) - c(x,y,0,t)(1-\frac{2T}{D}h), \text{ on } \Gamma_{z=0} \end{cases}. \tag{4.16}$$

Similarly, if a lattice point is located on boundary $\Gamma_{x=x_n}$, $\Gamma_{y=y_n}$ or $\Gamma_{z=z_n}$, the viral concentration at the corresponding vitural point is estimated by

$$\begin{cases} c(x_n+h,y,z,t) = c(x_n-h,y,z,t) - c(x_n,y,z,t)(1-\frac{2T}{D}h), \text{ on } \Gamma_{x=x_n} \\ c(x,y_n+h,z,t) = c(x,y_n-h,z,t) - c(x,y_n,z,t)(1-\frac{2T}{D}h), \text{ on } \Gamma_{y=y_n} \\ c(x,y,z_n+h,t) = c(x,y,z_n-h,t) - c(x,y,z_n,t)(1-\frac{2T}{D}h), \text{ on } \Gamma_{z=z_n} \end{cases}. \quad (4.17)$$

Furthermore, the injection of viruses is simulated by a point source that is mathematically inspired by the Dirac Delta function $\delta(\mathbf{x})$, which is mollified by using the normal distribution,

$$\delta(\mathbf{x}\,|\,\mathbf{x}_p,\varepsilon^2) = (\frac{1}{2\pi\varepsilon^2})^{d/2}\exp(-\frac{\|\mathbf{x}-\mathbf{x}_p\|^2}{2\varepsilon^2}), \quad (4.18)$$

where ε and d, respectively, denote the source width and the dimensionality.

4.3.2. TIME INTEGRATION

To update the concentration of virus on each lattice at the next time step, an IMplicit-EXplicit(IMEX) time integration is utilized, where the linear parts and nonlinear parts are treated by a Euler backward method and a Euler forward method, respectively. Thereby the concentration of virus c is updated by

$$c^{n+1}(\mathbf{r}) = c^n(\mathbf{r}) + \Delta t(D\Delta c(\mathbf{r}) + \gamma(t)\delta(\mathbf{x}-\mathbf{x}_p) + \beta c^n(\mathbf{r})(1-\frac{c^{n+1}(\mathbf{r})}{N_v})). \quad (4.19)$$

Note that this IMEX approach avoids the need of inner iterations to solve a nonlinear problem at each time step.

4.3.3. MONTE CARLO SIMULATION

Monte Carlo simulations are widely used in many quantitative probabilistic and statistical investigations that permeates much of finance, engineering and contemporary sciences [198]. To obtain quantities of interest, such as (cumulative) probability distributions of output variables and correlations, Monte Carlo simulations enable random sampling of input parameters from predefined probability distributions and extensive repetitive experiments.

Due to the variety of viruses and variations from patient to patient, many variables can hardly be determined or measured. For instance, the dose of a virus γ may depend on its effectiveness and toxicity, which varies among viruses. In addition, some variables, such as the concentration threshold at the time of viral infection $\hat{c}$, the reproductive rate of the virus in cancer cells α and human immune strength β, may all depend on patient lifestyle, gender and genetic pattern, and hence vary from patient to patient. However, the above-mentioned variables may be quantitively correlated to viral treatment outcomes, and thereby Monte Carlo simulations are performed on $X \in \{\gamma, \hat{c}, \alpha, \beta\}$. We assume that X follows a normal distribution $X \sim N(\mu, \sigma^2)$ with the mean value μ and the standard deviation σ. Therefore, the stochastic variable X with a number of samples N_s follows

$$X \sim \mu + \sigma N(0,1). \tag{4.20}$$

Taking the computational time into account, Monte Carlo simulations are performed in 2D simulations. Furthermore, Monte Carlo algorithms tend to be scalable and rely less on computational dimensionality. Referring to our previous work in Chapter 5, the accuracy of Monte Carlo simulation is proportional to the reciprocal of the square of the number of samples N_s, therefore 5000 samples are chosen to guarantee a small error.

4.4. NUMERICAL RESULTS

Since most clinical data is not available and some parameters have even never been measured, we estimate a couple of input parameters. The values have been listed in Table 4.1.

Table 4.1: Input values

Parameter	Notation	Value and Units	Source
Computational domain	Ω	$15 \times 15 \times 15$ mm^3	-
Virus diffusivity	D	0.01 mm^2/h	[199]
Injection rate	γ	1E4 pfu/(mm$^3 \cdot$ h)	[200]
Time step	$\mathrm{d}t$	0.1 h	Estimated
Probability rate of cell mutation	λ_{mu}	5 h^{-1}	Estimated
Probability rate of cell death	λ_{de}	5 h^{-1}	Estimated
New burst size of viruses	N_v	100	-
Vival infection threshold	$\hat{c}$	10 pfu/mm^3	Estimated

4.4.1. CANCER PROGRESSION

We consider a cubic domain to represent the tissue in the pancreas. The 3D domain $\Omega = 15 \times 15 \times 15$ mm^3 has been divided into $N = 30 \times 30 \times 30$ lattice points. Each lattice point is occupied by multiple cells and the volume of the solid tumor $V(t)$ at time t can be easily calculated by

$$V(t) = \frac{N_c(t) \times \text{Vol}(\Omega)}{N^3} \ (\text{mm}^3), \tag{4.21}$$

where Vol(Ω) is the domain volume and $N_c(t)$ denotes the number of lattice points in cancer state $\{S_i = 2\}$ at time t. To model cancer mutation occurring at the edge of a tissue or organ and its competitive growth with epithelial cells, a small number of lattice points are generated randomly in one octant of the domain only (see Figure 4.4(a)). Those lattice points are initiated with epithelial cell state indicated by blue color. Due to mutation, several lattice points change their states from $\{S_i = 1\}$ to $\{S_i = 2\}$ that are visualized by the red dots (see Figure 4.4(a)). Typically, normal cells stop dividing once they contact with each other during division as a result of contact inhibition, which can prevent excessive proliferation. Contrarily, mutated cancer cells often show uninterrupted growth that is called 'autonomous growth'. Moreover, cancer cells disperse more easily and invade the neighborhood tissue. Therefore, they have a larger growth and division rate despite limited space and nutrient supply. In the current simulation, the probability of mutation, proliferation and death is based on Equation (4.3) and several consecutive snapshots are shown in Figure 4.4. After 1600

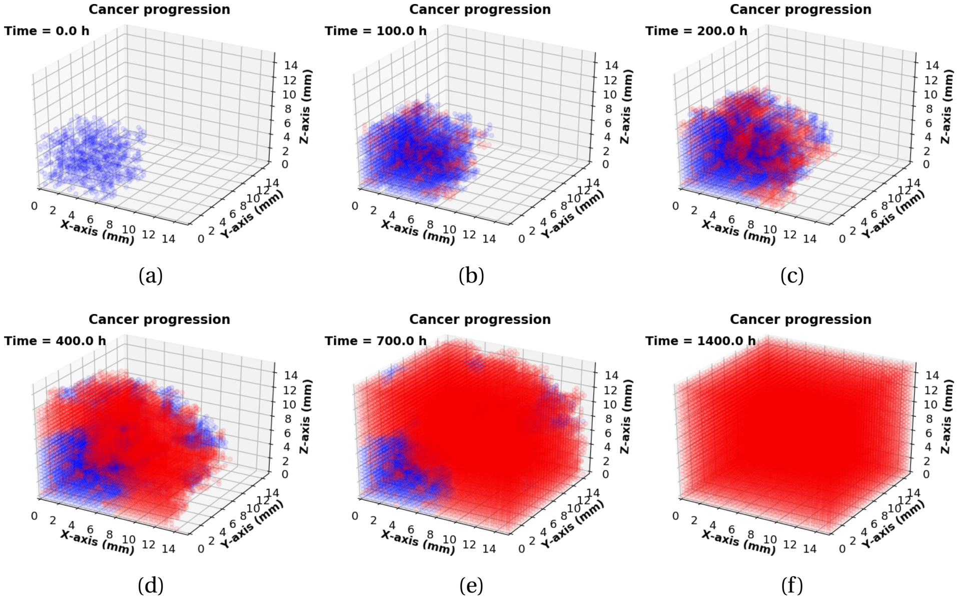

(a) (b) (c)

(d) (e) (f)

Figure 4.4: Consecutive snapshots of cancer progression, where blue color and red color are visualized as epithelial and cancer cells, respectively. The 3D domain 15 × 15 × 15 mm^3 meshes into 30×30×30 lattices. As a result, cancer cells occupy the entire computational domain when $t = 1600$ h.

hours (approximate 67 days), cancer cells occupy the entire computational domain and its corresponding growth curve with the respect of time indicated in red color is shown in Figure 4.5(a). According to Equation (4.6), the growth of cancer cells is influenced by α, which can be decided by $\alpha = \alpha_0 \cdot \frac{n_1}{n_{12}}$. To investigate the impact of α_0 on the tumor growth curve, multiple values (i.e. 0.75, 0.95, 0.98, 1) are used and the results show that growth of tumor volume slows down with the increase of α_0 value. Therefore, small variations of α_0 value facilitate our numerical model fitting experimental results.

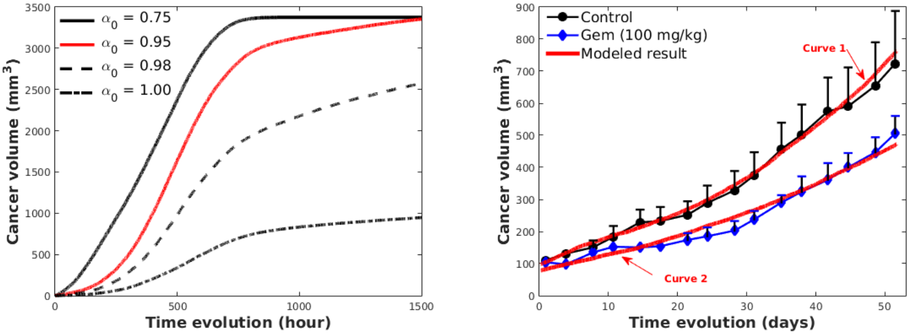

(a)

(b)

Figure 4.5: Growth curves of pancreatic tumor under different situations. (a) A comparison of growth curves of pancreatic tumors with various α_0 value (see Equation (4.6)), where $\lambda_{\max} = 5 \times 10^{-3}$; (b) A comparison of numerical results with experimental results refering to [201], where control and gem in the legend denote tumor growth without drug and with gemcitabine drug, respectively. In the simulation with curve 1, $\lambda_{\max}$ and α_0 are equal 1×10^{-3} and 0.94, respectively. However, to calibrate the model to curve 2, $\lambda_{\max}$ decreases to 5.5×10^{-4} and α falls to 0.85.

As an example, Figure 4.5(b) shows experimental results of tumor growth curve from the work by Durrant *et al.* [201], where pancreatic cancer cells are inoculated into immunodeficient mice, where the inoculation site is subcutaneous. Implanted cancer cells are allowed to grow during two weeks before the initiation of gemcitabine drug treatment (100µg/kg) and its growth curve is indicated by the blue curve in Figure 4.5(b). As a control experiment, the black curve in Figure 4.5(b) exhibits the growth of inoculated tumor without treatment. To mimic the tumor progression in this situation, we set up a model with a number of cancer cells initially in the domain. With minor variations of λ_i in Equation (4.4), our model is able to simulate various growth modes of pancreatic tumor (indicated by the red lines in Figure 4.5(b)), which fits the experimental results well. Over 50 days, our numerical results regarding the increase in tumor volume show a consistency with the experimental work [201].

4.4.2. ONCOLYTIC VIROTHERAPY

Oncolytic virotherapy has been recognized as a promising cancer treatment approach. We first develop a phenomenological model of oncolytic virotherapy in 3D, where the intratumoral injection of the virus is taken into consideration. The spread of viruses is simulated by the reaction-diffusion equation that is solved by using the FDM method. As a result, the diffusion of viruses in two different situations at time $t = 50$ h are compared in Figure 4.6. Due to the very different doses of virus administration [200, 202], we assume that the injection is carried out during a time span of 0.5 h with a total dose of approximate 3.6×10^5 pfu viral particles. Figure 4.6(a) shows viruses spread with the absence of cancer cells and new breeding viruses, whereas Figure 4.6(b) gives the distribution of viruses at time $t = 50$ h with the viral infection and newly generated viruses. A few isosurfaces are plotted with a color bar indicating the concentration of viruses. In contrast, viruses remain in the core of the computational domain and the highest concentration of viruses is up to 9.43×10^2 pfu/mm^3 in Figure 4.6(a). This is mainly due to a slow viral diffusivity [199] and insufficient viruses supply. The isosurface Figure 4.6(b) indicates that a small amount of viruses has spread near the boundary. Note that irregular isosurface in grey color has a concentration

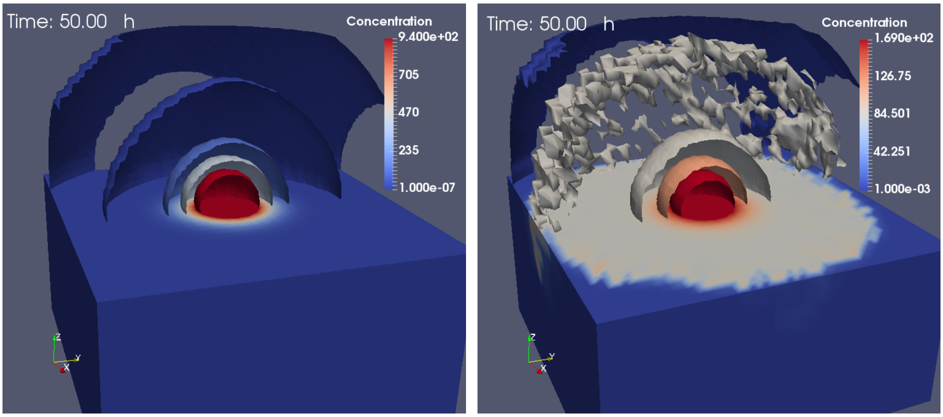

(a) (b)

Figure 4.6: A comparison of viruses diffusion by using the FDM method with a color bar indicating the concentration of viruses, where red color represents a high concentration of virus, dark blue hints a neglectable viral concentration and other colors denote values in between. (a) No cancer cells are present and viral infection is not simulated, which means no new proliferating viruses. Therefore, most viruses are mainly concentrated in the center ; (b) In the presence of cancer cells, viral infection ensues, viruses replicate leading to rupture of cancer cells, which then releases the viruses. The viruses are thus found also at distant locations. The isosurface in grey color has a concentration value of slightly less than 100 pfu/mm^3.

value of slightly less than 100 pfu/mm^3 since the new burst size of viruses when a cancer cell cracks is 100 pfu/mm^3 in the current model. Due to viral infection, the highest concentration of viruses in the core is 1.69×10^2 pfu/mm^3.

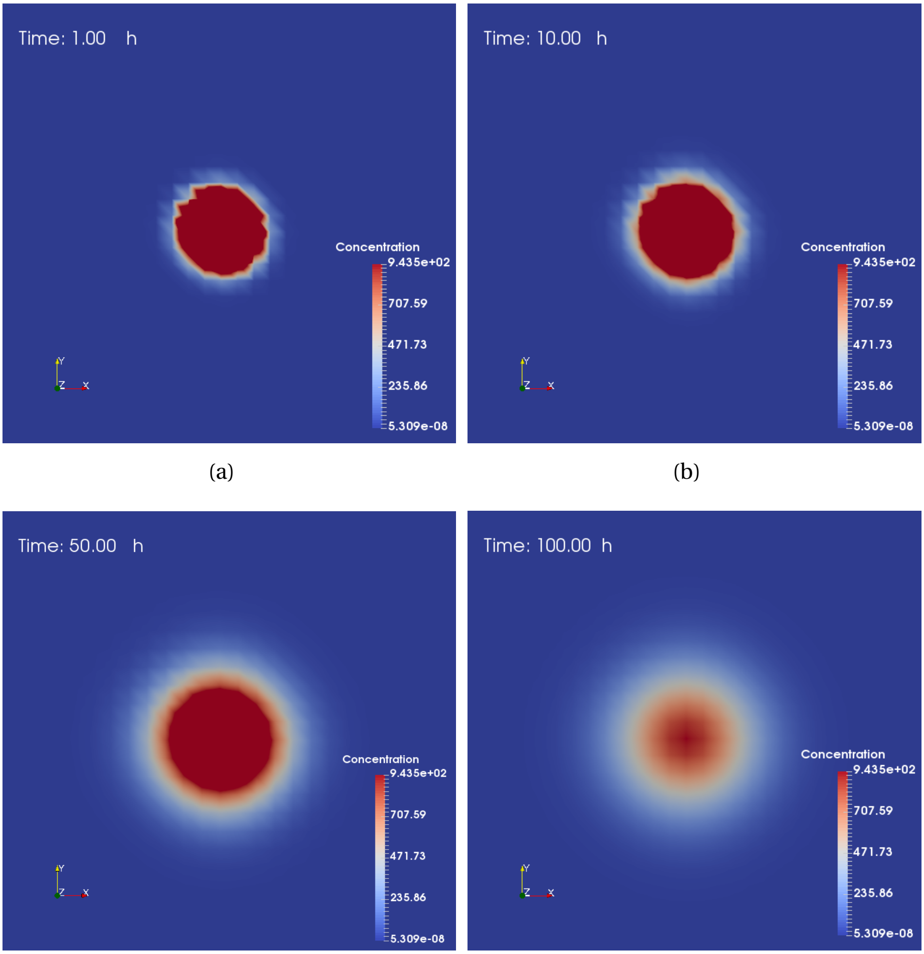

(a) (b)

(c) (d)

Figure 4.7: Consecutive slice plots of viral spread. No cancer cells are present and viral infection is not simulated, which means no new proliferating viruses. The slices are taken from the angle of a z-axis top view, which is located in the middle of the computational domain. A color bar indicates the concentration of viruses.

In addition, viral diffusion with the time evolution (when $t = 1, 10, 50, 100$ h) of each situation is shown by slices in Figure 4.7 and Figure 4.8, respectively. The slices are taken from the angle of a z-axis top view, which is located in the middle of the computational domain. Figure 4.7 presents a slow and relatively smooth diffusion phenomenon, with no viruses on the computational boundary at $t = 100$ h. However, viral spread in Figure 4.8 is faster as a result of the supply new breeding viruses from cancer cells and seems to be more random, which we think to be more in line with the infection and spread of viruses in reality. Eventually, some viruses spread to the edge and are dissipated from the border of the domain. Dissipated or remaining viruses after treatment might be removed by immune cells or, in worse cases, be virulent to healthy tissue. Therefore, it is vital to assess the toxicity of the remaining viruses after treatment.

To visualize the modeling progression of oncolytic virotherapy, some consecutive snapshots are shown in Figure 4.9. An extension of the model in Figure 4.4, where the computational domain $\Omega = 15 \times 15 \times 15$ mm^3 has been divided into $N = 30 \times 30 \times 30$ lattices. The domain is filled with cancer cells at time $t = 0$ h, see Figure 4.9(a). Typically, viruses are injected intratumorally if cancer occurs under the epidermis [203], otherwise, intravenous injection is the main approach for virotherapy [200]. However, the intravenous injections could cause many viruses to infect other tissue outside of the tumor, or be removed by the immune system or be dissipated before reaching the cancer area. To make the problem tractable, we consider one dose of intratumoral injection, which is given at the center of the domain. Subsequently, internal cancer cells will start to get infected, indicated in black color, and subsequently die, which is indicated by the white color, see Figure 4.9(b) and Figure 4.9(c). Local cells at lattice point i may get infected once the local concentration of viruses exceeds the threshold, which is $\hat{c} = 10$ pfu/mm^3. Afterwards, infected cancer cells (black color in Figure 4.9) are able to die (unoccupied (white) grid nodes) and release new breeding viruses with a burst size $N_s = 100$ pfu/mm^3. The dead lattice sites at state $S = 0$ are reminiscent to a wound. Then a chain reaction is triggered such that the virotherapy speeds up. Since internal lattice points are released after the death of cancer cells, we suppose that the normal constitutive cells around the cancer region will migrate to this area and fill the wound by proliferation, see Figure 4.9(d), Figure 4.9(e) and Figure 4.9(f).

The model describes an ideal virus type with a small dose to kill cancer cells, however, the role of the viral dose remains unclear. Since some viruses, like NDV, lead to a significant therapeutic benefit at high doses, whereas other viruses do not [200]. However, the residual viruses after therapy may be toxic, which varies from viral type to type. The risk could be tiny symptoms, such as flu or fever [204], and also could be severe like fatal muscle toxicity or neurotoxicity [205]. Therefore, the evaluation of residual viruses after treatment is crucially important. In our model, according to the boundary condition in Equation (4.9), viruses will dissipate from the boundary to other tissues or organs. Thereby we estimate the

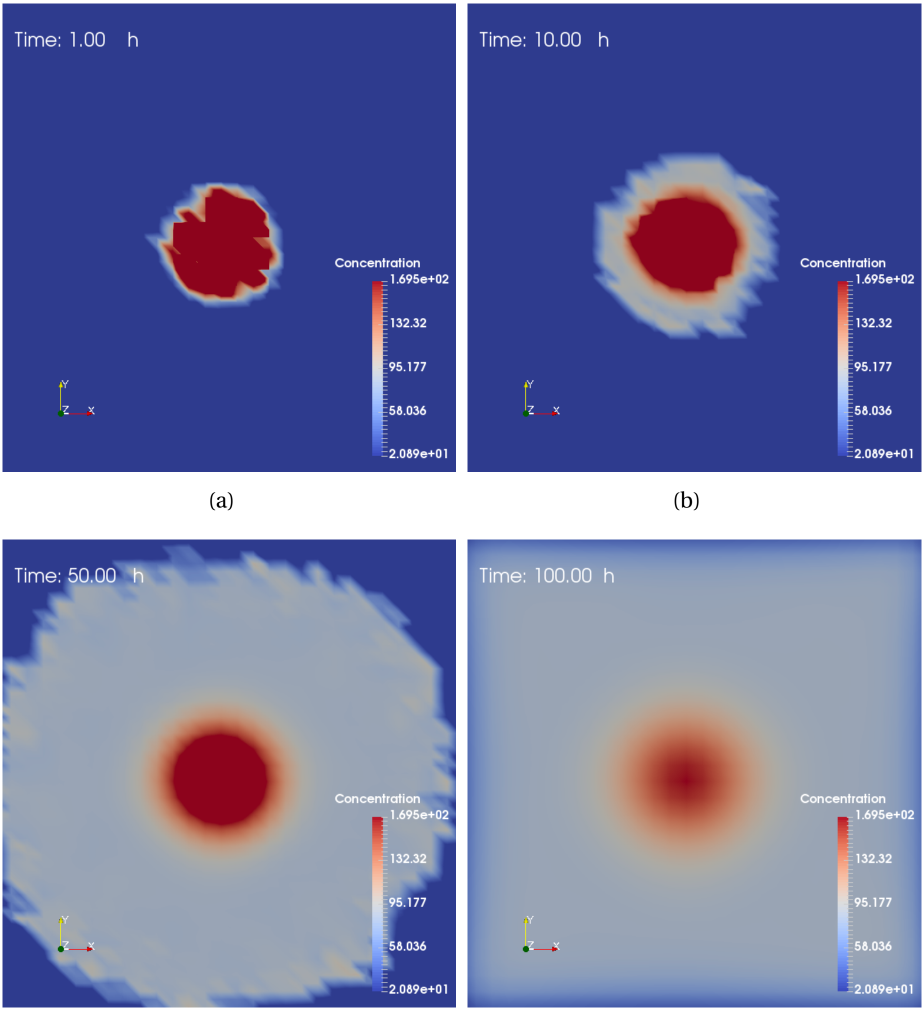

(a) (b)

(c) (d)

Figure 4.8: Consecutive slice plots of viral spread. In the presence of cancer cells (cancer cells are not shown for clarity), viral infection ensues, viruses replicate leading to rupture of cancer cells, which then releases the viruses. The slices are taken from the angle of a z-axis top view, which is located in the middle of the computational domain. A color bar indicates the concentration of viruses.

remaining viruses in the modeled area and ignore the dissipated viruses when $t = 100$ h. Figure 4.10(a) and b show changes in total viruses and cancer volume, respectively, in the domain with the evolution of time. At the beginning, a total dose 0.18×10^5 pfu (injection rate $r = 0.5 \times 10^4$ pfu/h) is given (see the enlarged

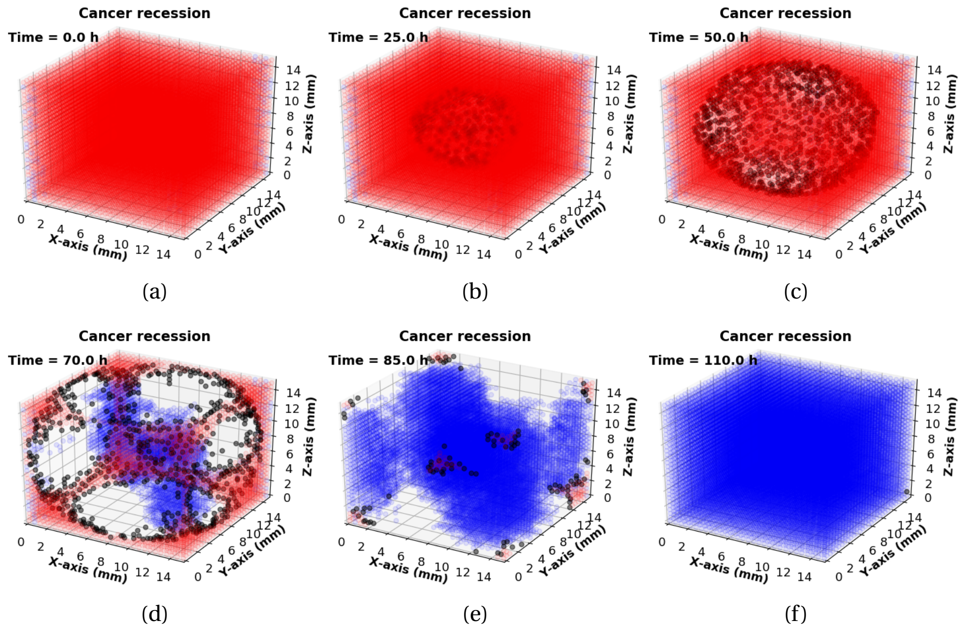

Figure 4.9: Consecutive snapshots of oncolytic virotherapy. The blue, red and black color are visualized as epithelial, cancer and infected cancer cells, respectively. In addtion, white color means the dead cells or unoccupied lattice points. A small scale of cancerous tissue that returns to normal tissue by cell reproduction or migration under the oncolytic virotherapy after $t = 110$ h.

view in Figure 4.10(a)), where the domain is fully occupied by cancer cells with a volume as large as 3375 mm^3 (see Figure 4.10(b)). Once cancer cells get infected

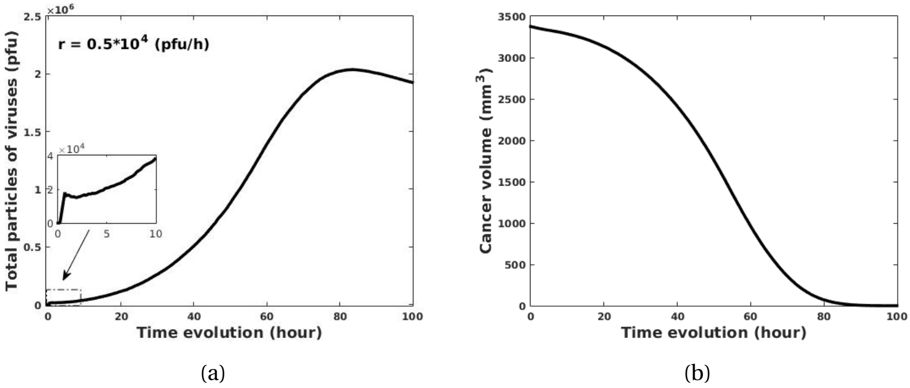

Figure 4.10: (a) Changes in viral quantity in the compuational domain with the evolution of time; (b) Changes in cancer volume with time.

by viruses, successful viruses begin to replicate themselves until the host cancer cells crack, which results in a significant increase in viral quantity and decrease in cancer volume. When time approaches 80 h, the number of viruses in the domain have accumulated to a peak (see Figure 4.10(a)), whereas most cancer cells are damaged (see Figure 4.10(b)). Furthermore, Figure 4.10(a) shows that the number of viruses gradually decreases after 80 h and this is mainly because a fraction of viruses escapes from the domain boundary. Note that there is a minor decline in the numer of viruses (see the enlarged view in Figure 4.10(a)), which may be due to the fact that the actual number of viruses present exceeds the carrying capacity of viruses. In order to investigate whether there is a maximum capacity of viruses in a limited domain, various injection rates (i.e. 1×10^4, 0.5×10^5, 1×10^5 pfu/h) are compared. The results given in Figure 4.11 show that a larger viral dose leads to a greater decline in total particles after injection and do not affect the eventual result because of the maximum capacity of viruses in the computational domain. The results suggest that if a certain threshold is exceeded for the amount of injected viruses, then its temporal evolution is more or less the same.

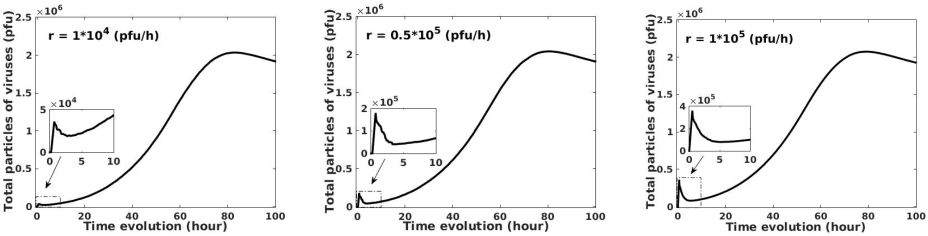

(a) (b) (c)

Figure 4.11: (a) Changes in viral quantity as the evolution of time with an injection rate r = 1×10^4 pfu/h; (b) Changes in viral quantity as the evolution of time with an injection rate r = 0.5×10^5 pfu/h; (c) Changes in viral quantity as the evolution of time with an injection rate r = 1×10^5 pfu/h.

4.4.3. MONTE CARLO SIMULATIONS

Kelly and Russell [206] showed that immunosuppressed patients normally have a better therapeutic benefit than those who have an intact immune system in oncolytic virotherapy. However, a defective immune system would lead to a large number of viruses, which is associated with unacceptable toxicity in most cases [205]. To make our model applicable to a wide range of virus species, the antiviral immune response is incorporated in the Monte Carlo simulations as one of the input variables, which we sample from a probability distribution. Therefore, Equation (4.9) is revised slightly to

$$\begin{cases} \frac{\partial c(\mathbf{r})}{\partial t} - D\Delta c(\mathbf{r}) = \sum\limits_{p\in\mathbb{V}(t)} \gamma(t)\delta(\mathbf{x}-\mathbf{x}_p(t)) + \beta c(\mathbf{r})(1-\dfrac{c(\mathbf{r})}{N_v}) - \eta c(\mathbf{r}) \\ D\frac{\partial c(\mathbf{r})}{\partial n} + Tc(\mathbf{r}) = 0, \quad \text{on } \partial\Omega \end{cases}, \tag{4.22}$$

where $\eta c(\mathbf{r})$ represents the neutralization process by immune cells and η denotes the neutralization rate. Therefore, the antiviral immune strength is investigated by variation of the η parameter. Since the appropriate dose of a specific virus is still unclear, the total dose of viral injection is considered by varying the injection rate r. Moreover, the infection threshold $\hat{c}$ is used to evaluate the ability of viral infectivity regarding its impact on the final total particles of the remaining viruses and cancer area. To perform the Monte Carlo simulations, 5000 samples are chosen for the injection rate r, infection threshold $\hat{c}$ and immune strength η, where sampling parameters follow the normal distribution. The mean and variance of the sampling parameters have been listed in Table 4.2. Taking CPU time into consideration, we limit each simulation up to 50 h and then compare total particles of the remaining viruses and cancer area in the computational domain. Based on 5000 samples, Figure 4.12(a) and Figure 4.12(b) show the histograms of the total particles of the remaining viruses and cancer area, respectively in 2D simulations with a total area of the domain of 225 mm^2 (15 mm × 15 mm). Of 5000 samples, 700 simulations end with few residual viruses, see Figure 4.12(a) and thereby there are around 700 cases with a cancer area above 200 mm^2 in Figure 4.12(b). These cases mean a failed virotherapy, which may be caused by a combination of low injection rate, high infection rate and a strong antiviral immune response.

Table 4.2: Mean and standard deviation in the Monte Carlo simulation sampling

Parameter	r	$\hat{c}$	η
Value	$(1\times10^4, (0.4\times10^4)^2)$	$(15\ 5^2)$	$(1\times10^{-2}, (1\times10^{-2})^2)$

Since the simulation is limited to 50 h, most cases end with a large cancer area compared with the original area, which is from 100 to 200 mm^2. Correspondingly, there is a large portion of simulations that have the remaining viral quantity ranging from 1×10^4 to 3×10^4 pfu at $t = 50$ h. To see the correlations between variables and the numerical results, several scatter plots are shown in Figure 4.13, Figure 4.14 and Figure 4.15. The role of viral dose is tested by using the injection rate r in Figure 4.13, which shows that there is no obvious correlation between the injected virus dose and the remaining viral quantity and cancer area. This

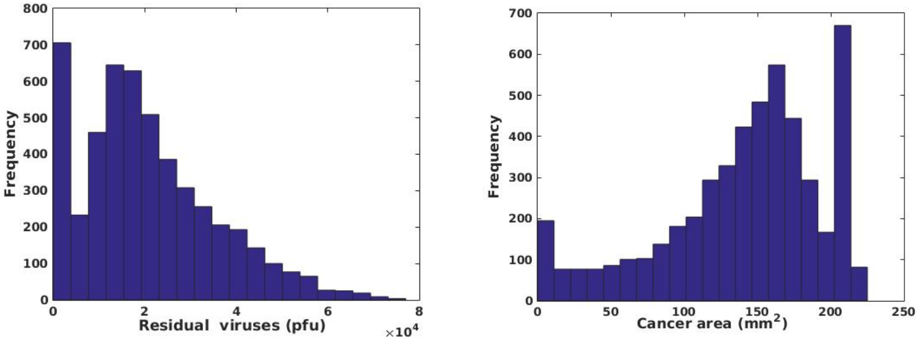

(a) (b)

Figure 4.12: (a) Histogram of residual viruses in Monte Carlo simulations on parameters r, $\hat{c}$ and η; (b) Histogram of cancer area in Monte Carlo simulations on parameters r, $\hat{c}$ and η.

is probably because of an insufficient simulation time period or the maximum capacity of viruses in a limited domain (see Figure 4.11 as an illustration for this claim). In contrast, the infection threshold, which is used to represent the ability of viral infectivity, shows a significant correlation with the remaining viral quantity and cancer area in Figure 4.14. The higher the threshold value, the higher the concentration of the virus is needed to infect the cancer cells, which hints at a lower ability of the viral infectivity. From Figure 4.14(a), the number of residual viruses decreases with increasing infection threshold since viruses with low

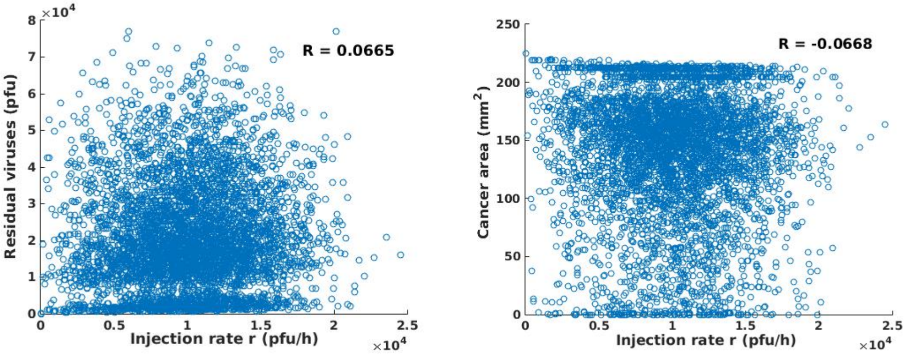

(a) (b)

Figure 4.13: (a) Scatter plot of injection rate r and residual viruses. The corresponding correlation coefficient is $R = 0.0665$; (b) Scatter plot of injection rate of r and the final cancer area with a correlation coefficient $R = -0.0668$.

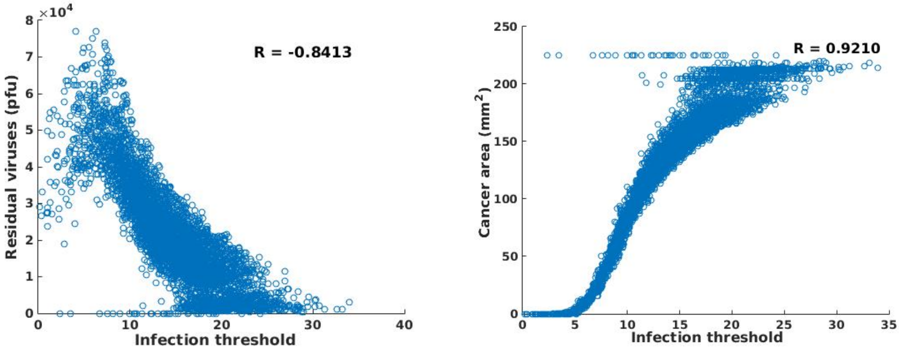

(a) (b)

Figure 4.14: (a) Scatter plot of infection threshold $\hat{c}$ and residual viruses. The corresponding correlation coefficient is $R = -0.8413$; (b) Scatter plot of infection threshold $\hat{c}$ and the final cancer area. The correlation coefficient of infection threshold $\hat{c}$ and the final cancer area is $R = 0.9210$.

infection ability are not able to damage cancer cells, but they can be eliminated by the antiviral immune response. Therefore, antiviral immune and insufficient newborn viruses facilitate cases with few residual viruses after 50 h. Certainly, the cancer area will not reduce significantly if the viral infection ability is weak. Viruses with a good infectivity ($\hat{c} \leq 5$) are able to neutralize cancer cells within a period of $t = 50$ h. Based on Equation (4.22), the term $\eta c(\mathbf{r})$ reflects the immune strength, therefore, the immune strength is investigated through variation of immune reduction rate η. Note that the value of $c(\mathbf{r})$ is quite large and thereby the η is chosen very small (from 0 - 0.06) to guarantee a simulation with a likelihood of success. A large η denotes a strong antiviral immune response that would result in the death of most viruses. According to Figure 4.15(a), in the case of immunodeficiency, the residual viruses could accumulate to a large amount, while the amount falls as the immunity increases. When the antiviral response is strong like $\eta > 0.04$, viruses will be eliminated by immune cells completely in the domain. On the contrary, the cancer area has declined with the intervention of residual viruses if the antiviral immune is defective (see when η arppoches to 0). However, the cancer area is more likely to be large in size when the immune response is strong, like $\eta > 0.04$. This indicates that patients with a weaker immune response may benefit from a larger reduction of the tumor size. However, at the same time, patients with a weak immune system are sensitive to have large amounts of residual viruses in their bodies.

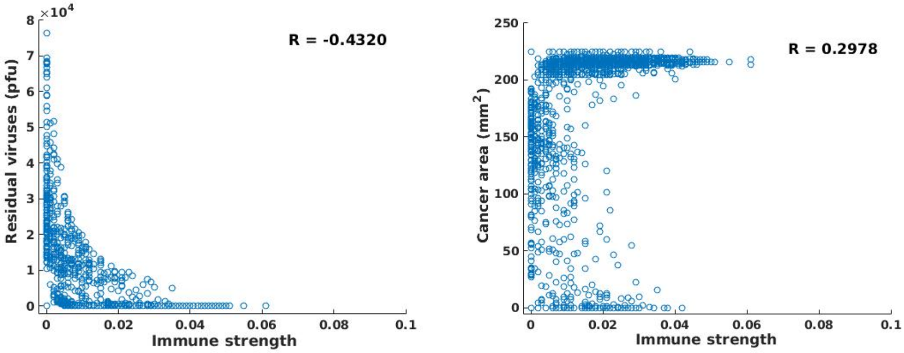

(a) (b)

Figure 4.15: (a) Scatter plot of immune strength and the remaining viral quantity. The correlation coefficient of immune strength and the remaining viral quantity is $R = -0.4320$; (b) Scatter plot of immune strength and the final cancer area. The correlation coefficient of immune strength and the cancer area is $R = 0.2978$.

4.5. CONCLUSION

Many animal-based experiments and clinical trials yielded a remarkable tumor attenuation by using oncolytic viruses [173, 176]. However, currently, viruses are not deemed as a useful means to stop or inhibit cancer since there is no effective way to control the virulence and retaining their replication capability in cancer cells [206]. We have developed a cell-based model in pancreatic cancer at early stages in Chapter 2, which is subsequently extended to therapy model in Chapter 3. However, compared to classical treatments for pancreatic cancer like surgery, radiotherapy, chemotherapy, virotherapy has its own limitations, which needs further scientific assessment. In particular, the limitations include antiviral immune responses, inefficient delivery of virus as well as the poor virus spread in tumor area [189]. Therefore, more research in terms of oncolytic virotherapy is needed.

In the present study, we develop a 3D cellular automata model for oncolytic virotherapy. As we expected, the model is able to simulate cancer progression at early stages, which include the biological processes such as mutation, proliferation and death. Within 1600 h (appropriate 67 days), cancerous cells mutate from healthy somatic cells and then colonize the computational domain as big as $15 \times 15 \times 15$ mm^3. Certainly, the model is scalable and the speed of cancer progression can be adjusted by variation of input parameters. Therefore, different growth trends have been compared and one numerical result of our model could fit experimental results very well. Subsequently, oncolytic virotherapy is phenomenologically simulated in the same domain that is completely occupied by cancer cells. The migration and proliferation of the virus is modeled by using a reaction-diffusion equation, which is solved by a FDM method. Since viruses specifically infect and damage cancer cells, the model predicts cancer attenuation as time evolves. Eventually, normal somatic cells fill in the gap through migration and proliferation.

In addition, Monte Carlo simulations are performed in a 2D model to quantitatively investigate the correlations between several input variables and numerical results. Among 5000 samples, there are 700 simulations end with few residual viruses and large cancer area, which dues to failed virotherapy probably as results of the extreme parameter values. The results indicate an insignificant correlation between the injection dose of viruses and simulated results (total residual viruses and cancer area), and that is probably because of an improper value range of injection rate, an insufficient simulation time period or a limited computational domain. However, we believe that this result is acceptable, since some virus species, such as NDV, show a high correlation between given doses and therapeutic benefits, whereas others do not [200]. Further, the viral infection threshold has a significant correlation with total amount of remaining viruses and with the final cancer area, which means that viruses with low viral infectivity likely allow a large cancer area with just few viruses left. Moreover, the anti-viral immune response presents an obvious correlation with the numerical results. Specifically, most simulations end up with relatively fewer viruses if the anti-viral reaction is strong and thereby the corresponding residual cancer area is also larger.

Due to gene mutation (i.e. RAS, TP53), the anti-viral infection ability of cancer cells is weakened, which gives the oncolytic viruses a chance [207] to infect the cancer cells. Research in oncolytic viruses is not limited to cancer therapy research, also in studies that combine other treatments, such as immunotherapy [208] and chemotherapy [209]. In order to optimize the viral therapy in terms of fighting cancer, and leaving as few viral particles post-therapy as possible, further experimental studies are necessary. The required quantification in order to optimize viral therapy implies that mathematical modeling is a necessary and very helpful step.

5

A PHENOMENOLOGICAL MODEL FOR CELL AND NUCLEUS DEFORMATION DURING CANCER METASTASIS

Cell migration plays an essential role in cancer metastasis. In cancer invasion through confined spaces, cells must undergo extensive deformation, which is a capability related to their metastatic potentials. Here, we simulate the deformation of the cell and nucleus during invasion through a dense, physiological microenvironment by developing a phenomenological computational model. In this chapter, cells are attracted by a generic emitting source (e.g. a chemokine or stiffness signal), which is treated by using Green's fundamental solutions. To incorporate the microvascular bloodstream, Poisseuille flow in a small blood vessel is considered. We use an IMEX integration method where the linear parts and the nonlinear parts are treated by using a Euler backward scheme and a Euler forward method, respectively. We develop the numerical model for an obstacle-induced deformation in 2D or/and 3D. Considering the uncertainty in cell mobility, stochastic processes are incorporated and uncertainties in the input variables are evaluated using Monte Carlo simulations. This quantitative study aims at estimating the likelihood for invasion and the length of the time interval in which the cell in-

---

The partial contents of this chapter have been published in the paper [210]: Jiao Chen, Daphne Weihs, Marcel Van Dijk, and Fred J. Vermolen. "A phenomenological model for cell and nucleus deformation during cancer metastasis." Biomechanics and modeling in mechanobiology 17, no. 5 (2018): 1429-1450.

vades the tissue through an obstacle. Subsequently, the 2D cell deformation model is applied to simplified cancer metastasis processes to serve as a model for in vivo or in vitro biomedical experiments.

5.1. INTRODUCTION

Cell locomotion is closely involved in various physiological and pathological processes. For example, the migration of leukocytes is important for the inflammatory response and movement of fibroblasts and also vascular endothelial cells are essential for wound healing [211]. On the contrary, cell migration can play a detrimental role during cancer metastasis, where the dissemination of cancer cells initializes the invasion-metastasis cascade as introduced by Chambers *et al.* [212], Fidler [213], Lambert *et al.* [214].

The diversity of cancers exceeds 200 distinct disease entities, which have differences in the normal cells of origin and similarities in subsequent cancer metastasis. Compared to primary tumors, metastatic cancers cause the overwhelming majority of cancer-associated deaths as high as 90% [214–216]. During the metastatic spreading of tumors, cancer cells can undergo transitions between two forms of movement, which are the amoeboid mode and the mesenchymal mode to optimize their invasiveness [217, 218]. Moreover, Pinner and Sahai [219] observe that cancer cells are able to move quickly (up to 15 μm/min) like some leukocytes and rapidly change their shapes and directions of migration in an amoeboid manner with intravital confocal microscopy technology. The amoeboid movement could happen in the absence of matrix protease [220, 221] where cancer cells alternatively generate large contractile force pushing fibers of matrix away and squeeze between small paths. However, if the contractile force is insufficient to deform the stiff extracellular matrix (ECM), the matrix-metallo proteases (MMP's) will be secreted by cancer cells to degrade the ECM and thereby invade further [222, 223]. In summary, cancer cells frequently chemically and/or mechanically 'dig' their ways through ECM in order to reach the distinct parts of the body.

When a single cancer cell is metastasizing through a narrow cavity, it must deform its morphology by extending its membrane into an elongated protrusion; this is often driven by external signals such as chemotaxis, durotaxis or tensotaxis. Large cell deformations will also induce changes in the nucleus morphology. Extensive deformation of the nucleus can induce damage, and reduce the nuclear envelope integrity, see for instance the work by Denais *et al.* [224]. However, the cancer cell is also capable of repairing its ruptured nuclear envelope and damaged DNA after the penetration. Then the cell may be able to further promote cancer development. Thus, as noted by Denais *et al.* [224], the stage of nuclear envelop rupture could represent a particularly fragile point, thereby providing an opportunity to develop new anti-metastatic cancer drugs to inhibit DNA repair and increase cell death. Cell deformation during cancer metastasis has been difficult to study in detail both in vivo and vitro, and further understanding of cell deformation mechanisms is crucially important. In cases where the pore sizes are much smaller than the size of the nucleus, the nucleus mostly arrests and fails to penetrate the pore due to defective nuclear deformability. On the contrary, with pore diameters above a threshold, e.g. 7 μm in the work [223], MMP-independent migration in dense ECM relies on the hourglass-shaped deformation of the nucleus. Hence, in this chapter, we develop a mathematical model to investigate the correlation between the deformation of a cell and of its nucleus, and show the dynamic changes in cell mechanostructure that occur during the invasion process.

Mathematical modeling has been shown to be an important tool to quantify the relations in many biomedical processes such as wound healing, cell migration and tumor progression in various scales. Cell deformation and migration models exist in the colony scale, e.g. in the works by Rey and Garcia-Aznar [225], Byrne and Drasdo [17], and Vermolen and Gefen [41], where the cell geometry is fixed to be circular or spherical, respectively, in 2D and 3D simulations. On a smaller scale, one looks at the deformation of individual cells, and to this extent, cellular automata models have been developed and combined with finite-element strategies by Borau *et al.* [226] and van Oers *et al.* [227]. Other cell deformation models are based on phase-field models, like in the work by Marth and Voigt [228], or on visco-elasticity with moving meshes as in [20]. A phenomenological approach to cell migration and deformation is proposed in Vermolen and Gefen [229] and Vermolen *et al.* [230], where in the latter work cell migration and deformation have been modeled in relation with the immune response system where white blood cells migrate out of the venules and transmigrate through the venule walls to chase and engulf pathogens. Moreover, Odenthal *et al.* [231] introduce a deformable cell model to describe mechanical communication among the interacting cells and between the cell and its environment. Another deformable model regarding the interactions with an emphasis on the relationship between varying matrix geometries and adhesion, contractility as well as cell velocity can be found in [232]. In terms of the nucleus deformable models, Moussavi-Baygi *et al.* [233] establish a coarse-grained model of the nuclear pore complex to simulate the nucleocytoplasmic transport. As the increasing attention in the cell mechanics, agent-based models are booming, see [72], where three types of agent-based models are described.

Cao *et al.* [234] develop a chemomechanical model to investigate the impacts of transmigration through confined interstitial spaces on the geometrical and mechanical features of the cell nuclei. In their model, the shape alterations of the cell and nucleus during the transendothelial migration driven by actomyosin contraction force can perturb the genomic organization, which in turn affects the behavior of cells. More nuclear profiles regarding chromatin deformations and nuclear envelope deformations during transmigration are further investigated. This mechanical model successfully predicts the morphological evolution when one cell transmigrates an endothelial gap [234]. In comparison, our model extends the process and behavior of cell transmigration driven by a chemical/ stiffness signal during cancer metastasis, whereas the most inner cellular mechanical properties are neglected for the sake of simplicity.

None of the aforementioned studies, however, have taken into account the Monte Carlo uncertainty quantification in the cell deformation modeling. This chapter aims at modeling the interaction between cell deformation (due to migration) and the deformation of the nucleus as well as quantitative analysis of unknown parameters by Monte Carlo simulations. We quantify the correlation between nuclear deformation relaxation and the cell's ability to penetration through narrow passages, which is important in the context of metastatic invasion. Section 5.2 describes the mathematical model in terms of the equations, subsequently, the numerical method is presented in Section 5.3, which is followed by the description of the results in Section 5.4. Finally conclusions are drawn in Section 5.5.

5.2. MATHEMATICAL MODEL

This section introduces the model in terms of mathematical relations. We start with the deformation of the cell and its nucleus in two dimensions and extend the formalism to three spatial dimensions subsequently. Moreover, the model is applied to simplified physiological transmigration of cancer cells and six parameters are studied by Monte Carlo simulations.

5.2.1. THE MODEL IN TWO DIMENSIONS

Table 5.1: Comparison of CPU-time and the cell penetration time τ

N	10	30	50	100
CPU-time	2.43 s	5.07 s	7.81 s	14.85 s
τ	0.3771 hour	0.3735 hour	0.3812 hour	0.3906 hour

The nucleus must move in coordination with the cell cytoskeletal dynamics at the front edge and rear end [235]. To mimic cell's cytoskeleton, a cell is treated as a collection of 30 parallel nodal points that are located on the cell membrane and on the outer boundary of the nucleus. We have compared the number of nodal points N ($N = 10, 30, 50, 100$) and we found that if the cell is freely moving that the pattern is hardly influenced by the number of springs, whereas the CPU-time increases proportionally with the number of springs. With a large number of springs, the time-step needs to be adjusted if the cell is in contact with an obstacle. In particular, it may happen if the resolution is too high that the nodal points on the cell boundary overtake each other when they are in (partial) contact with a rigid boundary. Taking the model in Figure 5.6 as an example (no perturbation of the random walk), the CPU-time and penetration time τ are compared with various N in the following Table 5.1. The table shows that CPU-time increases, whereas the cell penetration time τ is comparable with the increase of N. Each node on the cell membrane is connected to its corresponding node on the surface of the cell nucleus. On each of the nodes on the cell membrane surface, an external signal, such as a concentration gradient in the case of chemotaxis or durotaxis, is computed. This signal determines the movement of the nodal point. Next to this signal, the migration of the nodal point is determined by its position relative to its corresponding point of the nucleus boundary via the deformation relaxation of the cell's cytoskeleton. In this way the deformation and migration of the cell are modeled and sketched in Figure 5.1.

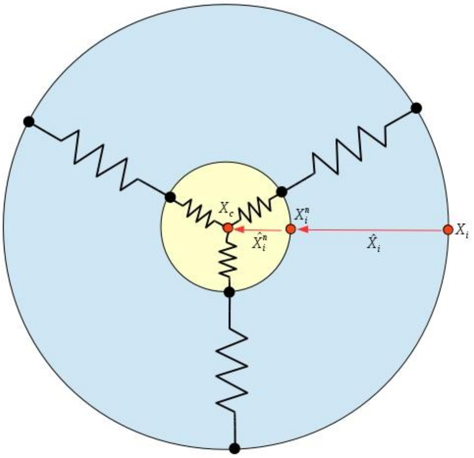

Figure 5.1: A schematic of the distribution of the nodal points on the cell boundary membrane and the surface of the nucleus. The cytoskeleton is represented as a collection of springs. The red dots, $\mathbf{x}_i$, $\mathbf{x}_i^n$ and $\mathbf{x}_c$, denote nodal points on the cell membrane, nucleus surface and x coordinate of the cell center of mass, respectively. The vectors $\hat{\mathbf{x}}_i$ and $\hat{\mathbf{x}}_i^n$ are represented in red arrows.

We consider a generic signal, of which the gradient determines the migration of the nodal points on the cell boundary membrane. This signal could be the extracellular stiffness or the concentration of a chemoattractant or a light intensity for instance. In the work by Massalha and Weihs [148], the gel-stiffness-dependent differences among cells with various metastatic potentials have been observed to be correlated with cancer invasiveness, where the metastatic cells apply a wide spectrum of traction forces (100 - 600 nN) for their adhesion to a stiffer gel. For the sake of presentation, we denote the intensity of the signal by $c(t,\mathbf{x})$, where t and $\mathbf{x}$, respectively, denote time and spatial position. The signal, as well as its gradient, can be obtained from a given relationship in which the gradient is determined either analytically or numerically. A numerical evaluation in a finite-element framework could be carried out by for instance gradient recovery techniques or by mixed finite-element formulations. In the present chapter, we consider a chemical attractant, such as a generic growth factor that attracts the cells. For the sake of illustration, we consider a point source since this allows for a simple treatment using Green's fundamental solutions. To this extent, let the emitting source of the chemoattractant by positioned on $\mathbf{x}_S$, then on an unbounded domain, we solve

$$-D\Delta c = \gamma_S \delta(\mathbf{x}(t) - \mathbf{x}_S(t)). \tag{5.1}$$

Here, D and γ_S represent the diffusion coefficient of the chemokine and the secretion rate of the source. Moreover, δ is the Delta Dirac function, while $\mathbf{x}(t)$ and $\mathbf{x}_S(t)$ denote positions of the nodal points on the cell membrane and the source. The fundamental solution to this equation in an unbounded domain is used in two spatial dimensions as follows,

$$c(t,\mathbf{x}) = -\frac{\gamma_S}{2\pi D}\ln(\mathbf{x}(t) - \mathbf{x}_S(t)). \tag{5.2}$$

In the presence of multiple cells, the superposition principle is used to construct the solution. We note that the signal can be taken as generic as one wishes. The above equation just serves as an illustration. Note that the above equation predicts negative values for the concentration if the distance between the point of observation and the source is too large. In our simulations, the distances are such that the above expression predicts nonnegative values only. Let the set $\mathbf{x}_i(t)$ and $\mathbf{x}_i^n(t)$, respectively, denote the nodal points on the cell boundary membrane and on the surface of the nucleus of the cell. Then, the migration of the nodal points on the cell boundary membrane is determined by

$$\mathrm{d}\mathbf{x}_i(t) = \beta\nabla c(t,\mathbf{x}_\mathbf{i}(t))\mathrm{d}t + \alpha\left(\mathbf{x}_i^n(t) + \hat{\mathbf{x}}_i - \mathbf{x}_i(t)\right)\mathrm{d}t + \eta \mathrm{d}\mathbf{W}(t), \quad i \in \{1,\dots,N\}. \tag{5.3}$$

Here $\hat{\mathbf{x}}_i$ represents the vector connecting the initial position of nodal point i on the cell boundary membrane to the initial position of point i on the cell nucleus (see Figure 5.1). This vector defines the equilibrium cell shape. In this text, we only consider circular and spherical cells, however, this formulation allows to consider cells of generic shapes such as dendritic shapes. Furthermore, β stands for the cell's response to external signals, and $\alpha > 0$ denotes the cell's deformation relaxation. Over a spectrum of cell types, the mobility of the cell boundary has a locally persistent random character [211], thus the last term takes care of the randomness movements of each node, where η is a constant and $\mathrm{d}\mathbf{W}(t)$ denotes a vector Wiener process with independent samples from a normal distribution with zero mean and variance $\mathrm{d}t$. The above equation warrants convergence to the equilibrium cell shape if there is no external stimulus for the deformation and migration of the cell.

Next, we introduce the equation of motion for the nodal points on the surface of the nucleus. We proceed similarly to the previous treatment of the nodal points on the cell boundary membrane, where we link the positions of the nodal points on the surface of the nucleus to their counterparts on the boundary membrane as well as to the position of the midpoint of the cell nucleus. To this extent, we obtain for $i \in \{1, \dots, N\}$

$$\mathrm{d}\mathbf{x}_i^n(t) = \alpha^n \left(\mathbf{x}_c(t) + \hat{\mathbf{x}}_i^n - \mathbf{x}_i^n(t)\right)\mathrm{d}t - \alpha\left(\mathbf{x}_i^n(t) + \hat{\mathbf{x}}_i - \mathbf{x}_i(t)\right)\mathrm{d}t + \eta \mathrm{d}\mathbf{W}(t). \tag{5.4}$$

Here α^n, $\mathbf{x}_c$ and $\hat{\mathbf{x}}_i^n$, respectively, stand for the deformation relaxation of the nucleus, the position of the center of the nucleus and the vector connecting the initial position of point i on the surface of the nucleus to the initial center of the nucleus (see Figure 5.1). Furthermore, the random character of the mobility of the boundary of the nucleus has been taken into account. This treatment of the points on the surface of the nucleus provides the interaction between the nucleus and the cell membrane. However, this interaction such that the deformation of the nucleus is delayed and damped with respect to the deformation of the membrane.

In order to maintain the right orientation of the cell, we also introduce the rotation matrix after rotation of an angle ϕ relative to the x-axis:

$$B(\phi) = \begin{pmatrix} \cos(\phi) & -\sin(\phi) \\ \sin(\phi) & \cos(\phi) \end{pmatrix}, \tag{5.5}$$

which tranforms a vector $\mathbf{x} \in \mathbb{R}^2$ to

$$\mathbf{x} \longrightarrow B(\phi)\mathbf{x}. \tag{5.6}$$

The rotation matrix $B(\phi)$ is used to determine the new equilibrium points of the cell boundary membrane and of the surface of the nucleus. Therefore, one cell is able to converge to its initial shape as well as to its rotation as a result of its migration to simulate the cell morphological polarization, see Figure 5.2 for a

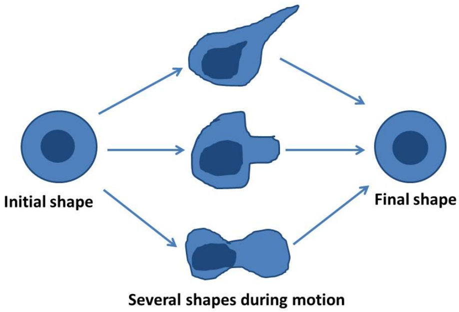

Figure 5.2: An example of movement and polarity of the cell.

sketch. The angle ϕ is determined such that it is closest to the current position of all the nodal points on the cell boundary membrane:

$$\phi = \underset{\phi \in [0,2\pi)}{\arg\min} \left(\sum_{i=1}^{N} ||B(\tilde{\phi})\tilde{\mathbf{x}}_i - \mathbf{x}_i(t)||^2 \right), \tag{5.7}$$

where $\tilde{\mathbf{x}}_i$ represents the initial position of the i-th node on the cell membrane surface with the cell center position at time t. After the above problem has been solved, then the angle of rotation of the cell with respect to the x-axis is known. This angle, ϕ, is substituted into the equations of motion for all nodal points on the cell membrane surface and on the surface of the cell nucleus, which gives for $i \in \{1,\dots,N\}$:

$$\mathrm{d}\mathbf{x}_i(t) = \beta \nabla c(t, \mathbf{x_i(t)})\mathrm{d}t + \alpha \left(\mathbf{x}_i^n(t) + B(\phi)\hat{\mathbf{x}}_i - \mathbf{x}_i(t) \right) \mathrm{d}t + \eta \mathrm{d}\mathbf{W}(t), \tag{5.8}$$

and

$$\mathrm{d}\mathbf{x}_i^n(t) = \alpha^n \left(\mathbf{x}_c(t) + B(\phi)\hat{\mathbf{x}}_i^n - \mathbf{x}_i^n(t) \right) \mathrm{d}t - \alpha \left(\mathbf{x}_i^n(t) + B(\phi)\hat{\mathbf{x}}_i - \mathbf{x}_i(t) \right) \mathrm{d}t + \eta \mathrm{d}\mathbf{W}(t). \tag{5.9}$$

Next we consider the treatment of an obstacle. Imagine that the surface or contour (in 2D) of the obstacle is given by $\partial\Omega$ and let the unit normal vector be given by $\mathbf{n}$, then we require that the component of the migration vector, $\mathrm{d}\mathbf{x}_i(t)$ has no component in the normal direction of the obstacle's surface, hence we require that the inner product of $\mathrm{d}\mathbf{x}_i(t)$ and $\mathbf{n}$ vanishes, that is

$$(\mathrm{d}\mathbf{x}_i(t), \mathbf{n}(\mathbf{x}_i(t))) = 0, \qquad \text{if } \mathbf{x}_i(t) \in \partial\Omega. \tag{5.10}$$

From this we subtract the component of $\mathrm{d}\mathbf{x}_i(t)$ in the direction of $\mathbf{n}$, hence this gives the following adjustment

$$\mathrm{d}\mathbf{x}_i(t) \longleftarrow \mathrm{d}\mathbf{x}_i(t) - (\mathrm{d}\mathbf{x}_i(t), \mathbf{n}(\mathbf{x}_i(t)))\,\mathbf{n}(\mathbf{x}_i(t)), \text{if } \mathbf{x}_i(t) \in \partial\Omega. \tag{5.11}$$

Note that herewith the obstacle slows down the migration of cells. This principle is also applied if cells are colliding into each other. The current model simplifies the mechanics of the cell considerably. Inertial effects would change equations (3,4,8,9) into second order equations with respect to the time derivative. The first term with the first-order time derivative is generally associated with friction or damping. Since in most studies inertia is neglected compared to friction terms [236–238], we are faced with a system of first-order differential equations. Note that the incorporation of more complex mechanics also increases the parameter space of the model, where input parameters are often hard to get.

5.2.2. EXTENSION TO THREE SPATIAL DIMENSIONS

Chemotaxis migration is modeled by using the Green's function as a solution of Equation (5.1). However, compared to the 2D model, the Green's functions in 3D changes to,

$$c(t,\mathbf{x}) = \frac{\gamma s}{4\pi D\|\mathbf{x}(t)-\mathbf{x}_s(t)\|^2}, \tag{5.12}$$

where both of $\mathbf{x}(\mathbf{t})$ and $\mathbf{x}_s(t)$ have x, y and z components.

The surface of the outer membrane and the nuclear surface are divided into mesh points. For this case, superpositions of the 3D Green's fundamental solutions are used, as well as the same principles for collision with obstacles and other cells. Further, the rotation can be imposed around all the three coordinate axes, and to this extent, the rotation matrix $B(\phi)$, entailing a rotation about the z-axis, where ϕ denotes the angle with respect to the x–axis, we extend the rotation matrix to all three coordinate axes:

$$B(\phi_x,\phi_y,\phi_z) = B_x(\phi_x)\cdot B_y(\phi_y)\cdot B_z(\phi_z). \tag{5.13}$$

Here $B_q(\phi_q)$ denotes the rotation matrix about the q–axis ($q \in \{x,y,z\}$), given by

$$\begin{aligned} B_x(\phi_x) &= \begin{pmatrix} 1 & 0 & 0 \\ 0 & \cos(\phi_x) & -\sin(\phi_x) \\ 0 & \sin(\phi_x) & \cos(\phi_x) \end{pmatrix}, \\ B_y(\phi_y) &= \begin{pmatrix} \cos(\phi_y) & 0 & -\sin(\phi_y) \\ 0 & 1 & 0 \\ \sin(\phi_y) & 0 & \cos(\phi_y) \end{pmatrix}, \\ B_z(\phi_z) &= \begin{pmatrix} \cos(\phi_z) & -\sin(\phi_z) & 0 \\ \sin(\phi_z) & \cos(\phi_z) & 0 \\ 0 & 0 & 1 \end{pmatrix}. \end{aligned} \tag{5.14}$$

All other principles remain the same and rotation is determined using a minimization with respect to the three coordinate angles.

5.2.3. THE APPLICATION TO CANCER METASTASIS

The ECM has pre-existing pores (diameter varies from 1 μm to 20 μm) or fiber-like (ranging from less than 3 μm to 30 μm in width) and channel-like (varying from 100 μm to 600 μm) tracks [239]. Furthermore, cells are viscoelastic objects such that morphological deformation happens frequently during the cancer invasion process [240]. Thence, our model for cell and nucleus deformation is applied to a simplified process occurring during cancer metastasis in a pore and a channel-like microenvironment. During the invasion, a cancer cell is normally able to squeeze obstacles like cells, tissue, capillary-sized vessels and deform itself as well as its nucleus to penetrate and seed in other organs. In the model, we use a constraint cavity with varying roughnesses to simulate the microenvironment during cancer spread, which is mimicked using a trigonometric function as follows.

$$y = \pm(y_0 + \epsilon \sin(\omega x)), \tag{5.15}$$

where y depicts the rough tube bounds and y_0 is a constant used to adjust the width of a tube. Through changing ϵ and ω, different roughnesses (varying amplitudes and frequencies) can be simulated.

5.3. NUMERICAL METHOD

5.3.1. TIME INTEGRATION

We describe the 2D case and provide information for the 3D case if it substantially differs from the 2D case. Initially the cell outer membrane surface is divided into N mesh points with respect to the cell center located on (x_c, y_c) as follows

$$\mathbf{x}_i(0) = (x_c + R\cos(2\pi\frac{(i-1)}{N}),\ y_c + R\sin(2\pi\frac{(i-1)}{N})), \quad i \in \{1,\dots,N\}. \tag{5.16}$$

where we assume the cell to be circular in 2D with radius R. The counterparts of the mesh points on the nuclear surface are given by

$$\mathbf{x}_i^n(0) = (x_c + R^n\cos(2\pi\frac{(i-1)}{N}),\ y_c + R^n\sin(2\pi\frac{(i-1)}{N})), \quad i \in \{1,\dots,N\}, \tag{5.17}$$

where $R^n < R$ represents the radius of the cell nucleus. The 3D spherical cell is described analogously for $i \in \{1, \ldots, N\}$ and $j \in \{1, \ldots, M\}$

$$\mathbf{x}_{i,j}(0) = (x_c + R\cos(2\pi\frac{(i-1)}{N})\sin(\pi\frac{(j-1)}{M}),\ y_c + R\sin(2\pi\frac{(i-1)}{N})\sin(\pi\frac{(j-1)}{M}), \\ z_c + R\cos(\pi\frac{(i-1)}{M})), \tag{5.18}$$

and on the nuclear surface by

$$\mathbf{x}_{i,j}(0) = (x_c + R^n\cos(2\pi\frac{(i-1)}{N})\sin(\pi\frac{(j-1)}{M}),\ y_c + R^n\sin(2\pi\frac{(i-1)}{N})\sin(\pi\frac{(j-1)}{M}), \\ z_c + R^n\cos(\pi\frac{(i-1)}{M})). \tag{5.19}$$

These initial values can be applied to the multi-cell configuration similarly. To determine the positions of the nodal points on the outer membrane surface, we use an IMplicit-EXplicit (IMEX) time integration to update the positions at the next time-step in such a way that the linear parts are treated in a Euler backward method, whereas the nonlinear parts are treated using a forward Euler method. This treatment has been chosen to avoid the need of solving a nonlinear system using an iterative procedure. This treatment results in the following equation (for the single-cell 2D case) for the nodes on the outer membrane

$$\mathbf{x}_i(t^{p+1}) = \mathbf{x}_i(t^p) + \Delta t \cdot (\beta\nabla c_i(t^{p+1}) + \alpha(\mathbf{x}_i^n(t^p) + \hat{\mathbf{x}}_i - \mathbf{x}_i(t^{p+1}))) + \eta\Delta\mathbf{W}, \tag{5.20}$$

and

$$\mathbf{x}_i^n(t^{p+1}) = \mathbf{x}_i^n(t^p) + \Delta t \cdot (-\alpha(\mathbf{x}_i^n(t^p) + \hat{\mathbf{x}}_i - \mathbf{x}_i(t^{p+1})) + \alpha^n(\mathbf{x}_c(t^p) + \hat{\mathbf{x}}_i^n - \mathbf{x}_i^n(t^{p+1}))) + \eta\Delta\mathbf{W}, \tag{5.21}$$

for the nodes on the nuclear surface, for $i \in \{1, \ldots, N\}$. Here, $\Delta\mathbf{W}$ is a 2D Wiener process with variables from a normal distribution with zero mean and Δt variance. For the definition and introduction of the vector-Wiener process, one can refer to [241]. For the gradient of the concentration (or any other signal that triggers cell migration and deformation), we use the following IMEX convention based on the Green's fundamental solutions in 2D (in 3D analogously)

$$\nabla c_i^{p+1} = \frac{\gamma_S(t^{p+1})(\mathbf{x}_S(t^{p+1}) - \mathbf{x}_i(t^{p+1}))}{\pi D||\mathbf{x}_S(t^p) - \mathbf{x}_i(t^p)||^2}. \tag{5.22}$$

5.3.2. CELL SHAPE

In order to compute the coordinate of the cell mass center, we need the area or volume of the cell and nucleus. The area $A(t)$ in 2D is computed by realizing that the cell is a polygon, which follows from

$$\begin{aligned} A(t) &= \int_{\partial\Omega} x(t) n_x(t) d\Gamma \\ &\approx \frac{1}{2}\Big[\sum_{i\in\{1,\dots N-1\}} (x_{i+1}+x_i)(y_{i+1}-y_i) + (x_1+x_N))(y_1-y_N)\Big]. \end{aligned} \tag{5.23}$$

For the 3D counterpart, we divide the cell into triangles (in order to allow any finite-element surface mesh), and compute the volume $V(t)$ of the cell by

$$\begin{aligned} V(t) = \int_{\partial\Omega} x(t) n_x(t) \mathrm{d}S &= \sum_{j\in\{1,\dots,N_{el}\}} \int_{\partial\Omega_j} x(t) n_x(t) \mathrm{d}S \\ &\approx \sum_{j\in\{1,\dots,N_{el}\}} \frac{|\Delta_j| n_x}{6} \cdot \sum_{m\in\{j_1,j_2,j_3\}} x_m, \end{aligned} \tag{5.24}$$

where N_{el} denotes the number of triangles that are used to approximate the cell (or nuclear) surface, and j_1, j_2 and j_3 refer to the indexes of the vertices of triangle j. Further, $\frac{1}{2}|\Delta_j|$ denotes the area of the j–th triangle, where we compute Δ_j by

$$|\Delta_j| = ||(\mathbf{x}_{j2} - \mathbf{x}_{j1}) \times (\mathbf{x}_{j3} - \mathbf{x}_{j1})||, \tag{5.25}$$

and the unit outward normal vector by

$$\mathbf{n}_j = \frac{(\mathbf{x}_{j2} - \mathbf{x}_{j1}) \times (\mathbf{x}_{j3} - \mathbf{x}_{j1})}{||(\mathbf{x}_{j2} - \mathbf{x}_{j1}) \times (\mathbf{x}_{j3} - \mathbf{x}_{j1})||}, \tag{5.26}$$

and hence to compute $|\Delta_j| n_x$, it suffices to take the x–coordinate of $(\mathbf{x}_{j2} - \mathbf{x}_{j1}) \times (\mathbf{x}_{j3} - \mathbf{x}_{j1})$.

For the 3D-case, we note that the area is computed by summing the areas of all the triangles, that is

$$A_b(t) \approx \frac{1}{2} \sum_{j\in\{1,\dots,N_{el}\}} ||(\mathbf{x}_{j2} - \mathbf{x}_{j1}) \times (\mathbf{x}_{j3} - \mathbf{x}_{j1})||. \tag{5.27}$$

5.3.3. MONTE CARLO SIMULATIONS

In our model, most experimental data is difficult or even impossible to collect, therefore, we refer to other literature data or estimate the input data and thereby evaluating the quantification of the propagation of uncertainty in the variables is very important. To investigate the output influence and correlation among variables, Monte Carlo simulations are carried out based on the model of cancer metastasis. There, a cell transmigrates through a narrow rough tubular path to get from one part of the surrounding tissue to another part. Passage through the tube requires deformation of the cells' cytoplasm and nucleus and affects the corresponding penetration time τ which is quantified under different conditions.

Suppose the variable $X \in \{D, \beta, \alpha, \alpha^n\}$ follows a normal distribution $X \sim N(\mu, \sigma^2)$, where μ and σ represent the mean of the distribution and the standard deviation. Then, the stochastic variable X could be generated by

$$X = (\mathrm{randn}(N_s, 1) \times \sigma) + \mu, \tag{5.28}$$

here N_s denotes the number of samples. The strength of the linear association between every variable and penetration time τ is quantified by the correlation coefficient r given by

$$r = \frac{\sum\limits_{j=1}^{N} (X_j - \bar{X})(\tau_j - \bar{\tau})}{[\sum\limits_{j=1}^{N} (X_j - \bar{X})^2 \sum\limits_{j=1}^{N} (\tau_j - \bar{\tau})^2]^{\frac{1}{2}}}. \tag{5.29}$$

Note the correlation coefficient is always bounded by $[-1, 1]$, where -1 or 1, respectively, indicates a perfect negative or positive linear correlation.

5.3.4. ERROR ANALYSIS

Numerical methods yield approximate results, where the numerical error E arises from the IMEX method and the Monte Carlo simulations. The IMEX time integration error E_{ti} is defined by

$$\|E_{ti}\| = \|\hat{\tau} - \hat{\tau}^{\Delta t}\| \leqslant C \cdot \Delta t, \tag{5.30}$$

here C represents a positive constant, $\hat{\tau}$ and $\hat{\tau}^{\Delta t}$ denote the real mean penetration time and numerical mean penetration time, respectively. The numerical result becomes accurate with the limitation of a sufficiently small time step Δt. Furthermore, the accuracy of the Monte Carlo simulations depends on the number of samples N_s and this error E_{mc} is achieved by

$$\|E_{mc}\| = \|\hat{\tau}^{\Delta t} - \hat{\tau}^{\Delta t}_{N_s}\| \simeq \frac{S_n}{\sqrt{N_s}}, \tag{5.31}$$

where S_n denotes the sample standard deviation and $\hat{\tau}^{\Delta t}_{N_s}$ is the sample mean as a result of N_s samples, which is $\hat{\tau}^{\Delta t}_{N_s} = \frac{\sum_{j=1}^{N} \tau_j^{\Delta t}}{N_s}$. Here $\tau_j^{\Delta t}$ denotes the penetration time of sample j, and the sample standard deviation is given by $S_n = \left[\frac{\sum_{j=1}^{N_s} (\tau_j^{\Delta t} - \hat{\tau}^{\Delta t}_{N_s})^2}{N_s - 1}\right]^{\frac{1}{2}}$. Note that this error decreases with increasing number of trials.

Therefore, the total error E is given by

$$\begin{aligned} \|E\| = \|\hat{\tau} - \hat{\tau}^{\Delta t}_{N_s}\| &\leqslant \|\hat{\tau} - \hat{\tau}^{\Delta t}\| + \|\hat{\tau}^{\Delta t} - \hat{\tau}^{\Delta t}_{N_s}\| \\ &\lesssim C \cdot \Delta t + \frac{S_n}{\sqrt{N_s}}. \end{aligned} \tag{5.32}$$

To keep the numerical approximation as accurate as possible, the time step should be small enough and the number of samples should be sufficiently large. Take the Monte Carlo simulations with six parameters as an example. If we fix all the six parameters and set the random walk parameter to zero, then the computation is fully deterministic. The time step is 0.0001 hour and the constant C can be estimated using Richardson error estimation by

$$\begin{cases} \hat{\tau} = \hat{\tau}^{\Delta t} + C \cdot \Delta t \\ \hat{\tau} = \hat{\tau}^{2\Delta t} + C \cdot 2\Delta t, \end{cases} \tag{5.33}$$

where $C = \frac{\hat{\tau}^{\Delta t} - \hat{\tau}^{2\Delta t}}{\Delta t} = 133$, which is a mean value of ten times calculations. With 10000 Monte Carlo (with sampling in the six parameters and using random walk) samples, the analytical error analysis can be derived as,

$$\begin{aligned} \|E\| &\leqslant 1.33 \times 10^{-2} + \frac{0.0687}{\sqrt{10000}} \\ &\simeq 1.40 \times 10^{-2}, \end{aligned} \tag{5.34}$$

where 0.0687 is the sample standard deviation S_n. Therefore, the total error in the Monte Carlo simulations with six parameters is bounded by 0.014 hour.

5.4. NUMERICAL SIMULATIONS

First we describe the simulations in which one cell migrates towards the gradient of an increasing stimulus along with obstacles in 2D and 3D. Subsequently, this deformation model of the cell and its nucleus is applied to a simplified cancer metastasis phenomenon. Furthermore, six parameters are studied and analyzed by Monte Carlo simulations.

5.4.1. PARAMETER VALUES

Most often the experimental parameter values are not available to us, therefore estimating input values based on experimental literature is essential. For example, we use 10 μm in 2D and 16 μm in 3D for diameters of the nucleus referring to the work by Friedl *et al.* [235], where the diameter of the nucleus varies from 10 ~ 20 μm in 2D and 5 ~ 15 μm in 3D. Analogously, other default input values are listed in Table 5.2, as well as the sources from the literature whenever possible.

Table 5.2: Parameter values

Parameter	Notation	Value and unit	Source
Radius of a circular cell in 2D	R	12.5 μm	[242]
Radius of a spherical cell in 3D	R	10 μm	[242]
Radius of a circular nucleus in 2D	R_c	5 μm	[235]
Radius of a spherical nucleus in 3D	R_c	8 μm	[235]
Cell deformation relaxation	α	250 hour^{-1}	-
Nucleus deformation relaxation	α^n	2500 hour^{-1}	-
Diffusivity of the chemokine	D	3600 μm^2/hour	[243]
Mobility of points on cell membrane	β	60 hour^{-1}	[41]
Secretion rate of the chemokine	γ_s	1.2 $\times 10^6$ mol/hour $\cdot\, \mu$m^3	[165]
Time step in 2D	Δt	0.0001 hour	[219]
Time step in 3D	Δt	0.01 hour	-
Number of nodes on a 2D cell	N	30	-
Number of circles on a 3D cell	N_c	30	-
Pressure difference	dp	1 kPa/100 μm	-
Viscosity	μ	0.1 Pa·hour	-

5.4.2. CELL MIGRATION ALONG A RIGID OBJECT IN 2D AND 3D

ONE CELL MIGRATING ALONG A RIGID OBJECT IN 2D

In solid tumors, cell migration shows trends in its direction according to the presence of chemotactic gradients or other external cues. Since there are many parallels existing in the mechanisms underlying the movement of cancer cells and immune cells within tissues as well as in the blood circulation [219], the modeled cell can be an immune cell with a chemical source of antigen or a cancer cell with a source of oxygen or substrate/ECM stiffness.

The cell moves according to the gradient of chemokine. Snapshots at different stages of the migration are shown in Figure 5.3, where the red, green and grey objects visualize the cell, nucleus and a rigid obstacle, respectively. Furthermore, the signal source location is represented by an asterisk. To pass a stiff barrier or overcome an obstacle, the migrating cell has to reshape and adapt the mechanostructure of the cytoplasm and the membrane. That is done via exerting contractile forces or withstanding the stresses from neighbor cells, which are mediated by the cell cytoskeleton [244]. According to the experimental observation of Brunner *et al.* [244], one migrating cell could push a small obstacle upwards by exerting forces and crawl underneath this obstacle. Given a larger obstacle in our simulation, the cell and nucleus are more likely to crawl along the rigid boundary by morphological adjustments to different extents. Ultimately, the cell

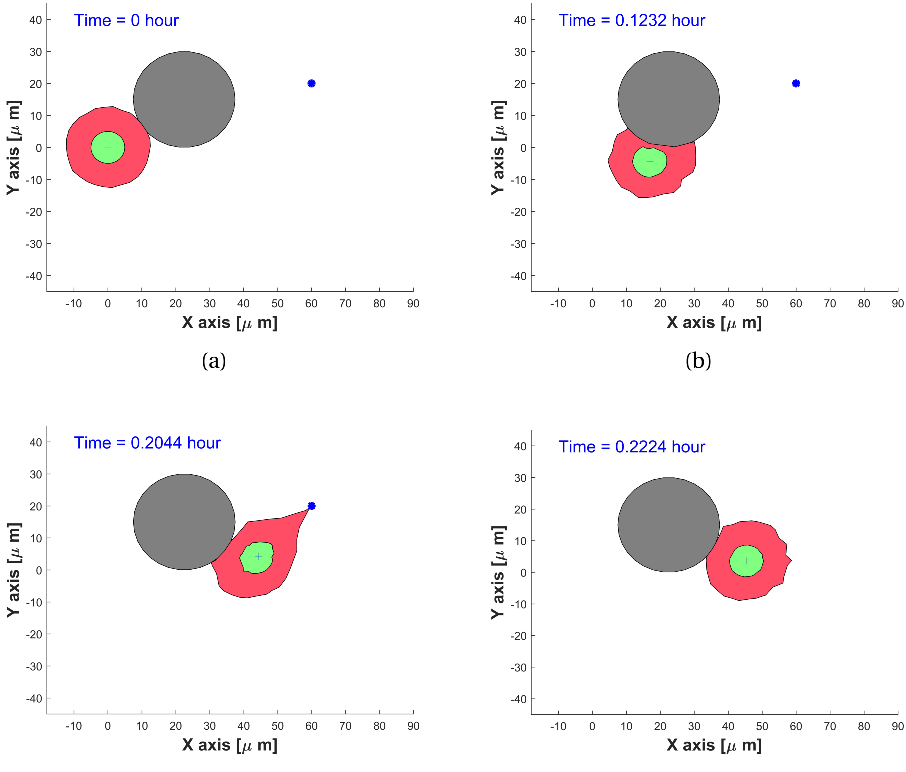

(a) (b)

(c) (d)

Figure 5.3: Consecutive snapshots of one cell migrating along a rigid obstacle in a 2D simulation. The cell, nucleus and obstacle are visualized by red, green and grey colors, respectively. A blue asterisk denotes a source secreting a chemokine with the secretion rate of 2×10^5 mol/hour $\cdot\, \mu\mathrm{m}^3$. The CPU time of this model takes 2.20 seconds.

and nucleus are able to return to their initial shapes due to cell polarity once the source is no longer active.

ONE CELL MOVING ALONG A RIGID OBJECT IN 3D

In three-dimensional interstitial tissues, cells typically utilize one of two mechanisms for invasion: mesenchymal or amoeboid, respectively, involving degradation of the surrounding ECM or squeezing through sub-cell-size pores in the ECM; these mechanisms require, respectively, proteinases that can degrade the ECM or deformations of the cell shape [235]. To simplify the problem and make it time-efficient to solve, we only consider the mechanical deformability of the cell in this model rather than deformability of both the environment and the cell. The degradation of the ECM is hence modeled implicitly in the β-term in Equa-

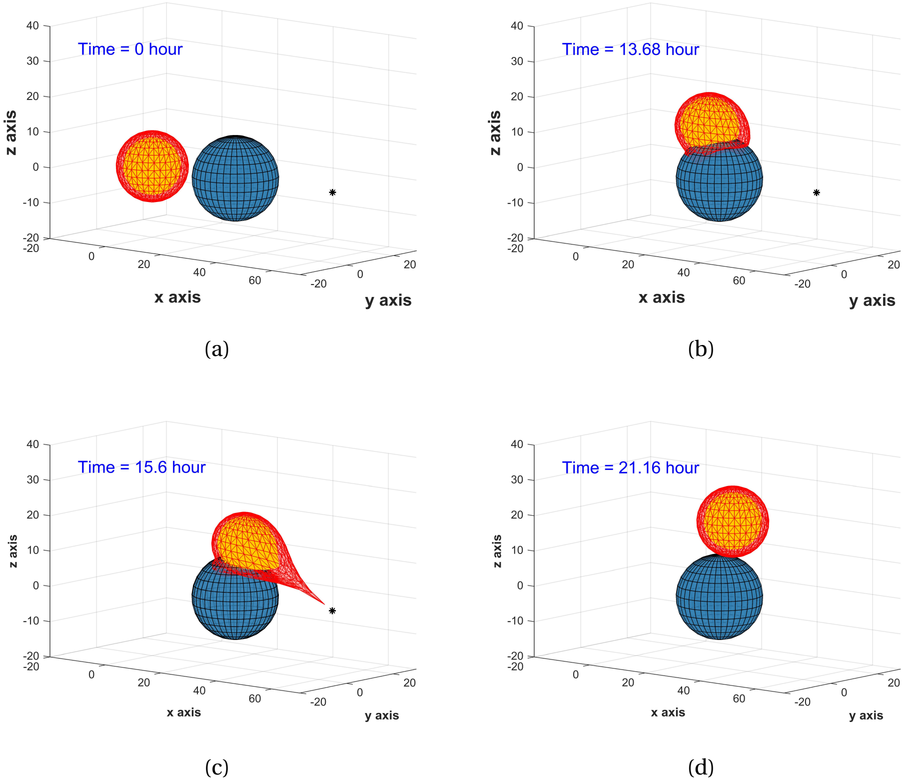

(a) (b)

(c) (d)

Figure 5.4: Consecutive snapshots of one cell migration along a rigid obstacle in 3D simulation. The cell, nucleus and obstacle are visualized by red, yellow and blue colors, respectively. A black asterisk denotes any type of sources. The CPU time of this model is 21.77 seconds.

tion (5.3). Note that if the ECM decay-rate would be zero, then the β-parameter would be zero as well. Hence the β-parameter accounts for the decay of ECM and the mobility of the node. In a future study, the decay process of the ECM could be modeled more explicitly so that the migration and deformation process of the cell can be modeled to be rate-determined by the slowest process. We model a 3D cell with a spherical equilibrium geometry that travels over an obstacle towards a source that secretes a chemokine, e.g. for immune cells the source may be a pathogen. In Figure 5.4, consecutive snapshots of a 3D cell that reaches a source and engulfs it are shown. It can be seen that the cell deforms mechanostructurally and that the cell shape returns to its equilibrium spherical shape once the stimulus has been removed. Note that the cell is still attached to the obstacle once the source has disappeared. Due to this mechanical attachment and cell elasticity, the cell deforms back to its equilibrium and thereby pushes itself away from the obstacle such that there is only attachment at one point of the cell boundary to the obstacle. This is a characteristic of the current model in which steady-state adherence has been neglected. The figures illustrate how the model takes into account the hard mechanical impingement between the cell and the rigid obstacle.

In general, dimensionality does not affect the expected numerical result in this case. Furthermore, the computational time of a 2D model is much shorter as a result of the need for fewer gridpoints on the boundaries of the cell and nucleus, and thereby we use a 2D model for further application and analysis in this work.

5.4.3. APPLICATION TO CANCER METASTASIS IN 2D

There are pre-existing openings (pores, fiber-like or channel-like tracks) in ECM that enable cancer cells to migrate with the independence of MMP's [239]. In this section, we apply the model to the transmigration of cancer cells through pores and channels to migrate from one part to another part of the tissue without degrading ECM.

SIMULATION ON PENETRATION OF A CELL THROUGH A CAVITY

We initially consider a single cell penetrating through a cavity, which is formed by two circular obstacles, without secreting proteolytic enzymes and remodeling the ECM; i.e. the cell migration is assumed to utilize the amoeboid mode. The initial state is shown in Figure 5.5 (top-left). The cell is attracted to an imaginary source (indicated by the blue asterisk) that releases a chemokine or an ECM stiffness signal. The migration of the cell is directed up the gradient of the chemokine, and it is limited by the presence of the two physical obstacles. Further, it can be seen that the cell is mechanically compressed as a result of its shrinkage due to its migration through the cavity and the nucleus deforms whenever the size of the pore is smaller than the size of the nucleus, see Figure 5.5. As soon as the cell exits the constriction and is no longer mechanically compressed, the nucleus returns to its equilibrium circular shape. Once the source has been engulfed, the cell shape returns to its equilibrium circular shape. The model only incorporates temporary adherence to the obstacle, no permanent adherence. After the disappearance of the source, the only restoration of the cell shape is modeled.

SIMULATION ON PENETRATION OF A CELL THROUGH A TUBE CHANNEL

Cell deformation is normally studied in vitro by using microfluidic devices [245–247]. In the latter work, discord-shaped red blood cells have been shown to be

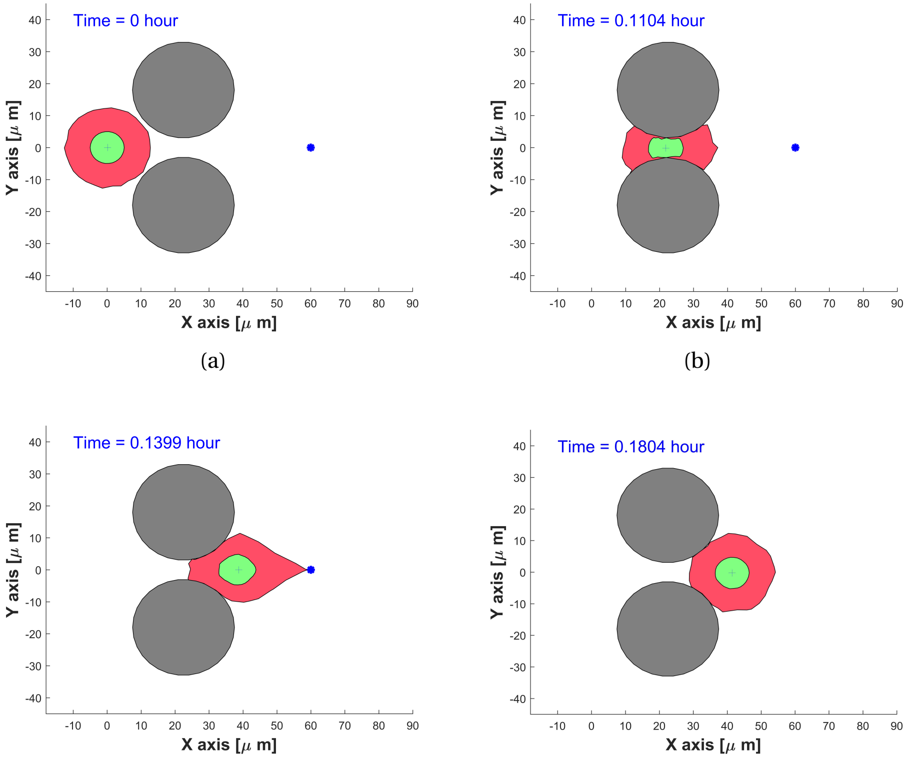

(a)

(b)

(c)

(d)

Figure 5.5: Consecutive snapshots of one cell penetration a cavity made of two obstacles in 2D simulation. The cell, nucleus and obstacles are visualized by red, green and grey colors, respectively. A blue asterisk denotes any type of sources. The CPU time of this model is 2.18 seconds.

able to repeatly deform when penetrating through microcapillaries with a diameter of 2.5 μm or even less. As mentioned in Section 5.2.3, there are abundant pre-existing fiber-like and channel-like tracks formed by the alignments of the collagen architecture in interstitial tissues and organs, which guide or inhibit cell migration [239, 248]. In Figure 5.6, a schematic representation of an endothelial cell wall with a channel of approximate 10 μm in width is depicted [239]. This value is considered here to guarantee that the cell is able to penetrate through it in most cases.

Mechanical boundaries could regulate some biomedical processes and Mak *et al.* [245] demonstrate that if the confined dimensional modulation of a microfluidic device has a mechanical barrier smaller than the cell nucleus, then metastatic breast adenocarcinoma cells likely deform in elongated morpholog-

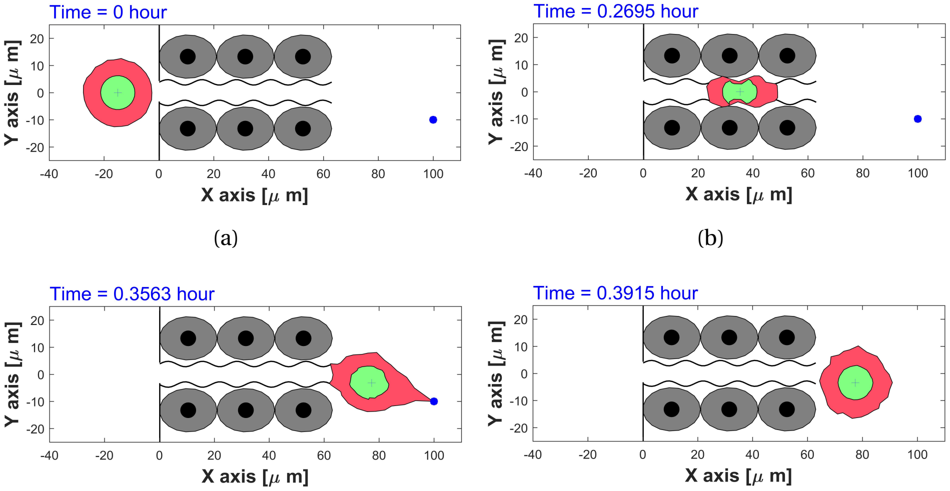

(a) (b)

(c) (d)

Figure 5.6: Consecutive snapshots of one cell penetration through an endothelial cell wall in 2D simulation. The migrating cell, nucleus and endothelial cells are visualized by red, green and grey colors, respectively. A blue asterisk denotes any type of sources. The CPU time of this model is 6.05 seconds.

ical states and invade distinct sites. Here, taking mechanical boundaries into account, we use the trigonometric function (from Equation (5.15)) to simulate the different roughnesses through changing the value of parameter ϵ and ω. A highly rough boundary of the channel is defined if the perturbation (see Equation (5.15)) has a high frequency or/and a big amplitude, which is determined by the surface of the endothelial cells. Whereas a lower frequency (also a lower amplitude) as we depict in Figure 5.6 could show where each cell is located. The discrepancy between the endothelial cellular surfaces and the channel through which cancer (or immune) cell migrates, could be a consequence of the extracellular matrix around the cells. Then the boundary of the channel can have various roughnesses, which combined with other parameters, are analyzed by using Monte Carlo simulations based on this model. To investigate how the cell speed changes in the current scenario, the speed evolution with the respect of time is plotted in Figure 5.8(a) without the perturbation of vector Wiener process. As we expected, the cell speed slows down when it starts to squeeze the opening and subsequently accelerates to move toward the emitting source. When the τ equals approximate 0.37 hour, the instantaneous speed reaches a peak and drops to zero after the engulfment of the source and cell shape recovery. During the transmigration in the tube, the cell migrates with a speed vibrating up and down at 200 μm/hour, which is in the range 1-5 μm/min for the typical speed of amoeboid movement observed in vivo in the work [219]. Moreover, cell speed can be controlled under various conditions, like the number of emitting sources, the diffusion coefficient, cell mobility, etc.

SIMULATION ON CANCER METASTASIS

Immune cells and cancer cells similarly deform in chemically or mechanically induced locomotion. The work by Springer [249] reports that leukocytes can attach to the wall of a blood vessel by binding to adhesion molecules of the endothelial cells, subsequently the leukocytes flatten themselves, and then squeeze through openings which are much smaller than themselves among the endothelial cells. Analogously, metastatic cells utilize similar mechanisms when intravasting into or extravasating out of blood vessels. Cancer metastasis is a multi-step cascade that can be divided into the following steps, 1) escape from the primary tumor site; 2) survive transit in the bloodstream or lymphatic vessels after successful intravasation; 3) disseminate and extravasate subsequently; 4) start to proliferate and colonize secondary sites at distant organs [250, 251]. We attempt to simulate the steps of intravasation and extravasation and several consecutive snapshots showing the shape changes of cell and nucleus are provided in Figure 5.7, where a schematic diagram of a capillary-sized channel is depicted. In order to get around hypoxia (or lack of nutrition) as a result of competitive growth in cancer cell colonies or as a response to a stiffness gradient, metastatic cells show migratory exploratory behavior towards regions outside the colony they reside in. This migration can be inspired by gel-stiffness-dependent differences in traction forces or strain energies in [148]. Therefore cancer cells are capable of penetrating through small openings in endothelium. This process is highly inefficient, and during this dissemination, the majority of cancer cells would die and only $< 0.02\%$ of them are able to seed at distant sites successfully [252, 253].

Since we are assuming a slow flow in the capillary-sized vessel, it is natural to consider laminar flow. Note that we only consider a component in the axial direction of the blood flow velocity to simplify the phenomenon. Considering the pressure-induced Poisseuille flow, where the bloodstream is treated as an incompressible fluid, the solution reads as

$$u_z(r) = -\frac{\partial p}{\partial z} \cdot \frac{R_t^2}{4\mu} \cdot (1 - \frac{r^2}{R_t^2}), \quad \text{in } \Omega_b, \tag{5.35}$$

where, p, μ and R_t denote the pressure, viscosity of fluid and half width of the blood vessel. Within the vasculature domain Ω_b, the distance between one nodal point and vessel boundary r decides the axial velocity of the nodal point, which gives a parabolic profile. This straightforward phenomenological treatment of the blood flow can also be found in [88]. Then the position of a nodal point $\mathbf{X}_i(t)$ is determined by

$$\mathrm{d}\mathbf{x}_i(t) = \beta\nabla c(t,\mathbf{x}_i(t))\mathrm{d}t + \alpha\left(\mathbf{x}_i^n(t) + B(\phi)\hat{\mathbf{x}}_i - \mathbf{x}_i(t)\right)\mathrm{d}t + u_z(r_i)\mathrm{d}t + \eta_1\mathrm{d}\mathbf{W}(t). \quad (5.36)$$

and the motion of a nodal point on the surface of the nucleus is given by

$$\mathrm{d}\mathbf{x}_i^n(t) = \alpha^n\left(\mathbf{x}_c(t) + B(\phi)\hat{\mathbf{x}}_i^n - \mathbf{x}_i^n(t)\right)\mathrm{d}t - \alpha\left(\mathbf{x}_i^n(t) + B(\phi)\hat{\mathbf{x}}_i - \mathbf{x}_i(t)\right)\mathrm{d}t + \eta_2\mathrm{d}\mathbf{W}(t). \quad (5.37)$$

We note that the current formalism is two-dimensional and that real world situations are three-dimensional. In a three-dimensional setting a cell is able to migrate around a venule and hence it is able to reach a location behind a small blood vessel without having to be transported through a vessel. The current simulation should be considered as phenomenological in the sense that the current model provides a formalism that can be used to use the following chain: (1) transmigration of (cancer) cells through a vessel, (2) transport through the small blood vessel to a remote location, and (3) the subsequent transmigration through a vessel wall, triggered by an external signal, to exit the blood vessel. Finally, the cell can possibly colonize through possible successful proliferation in its environment. This is one of the scenarios in which cancer can spread from one tumor to different locations in the body of an organism.

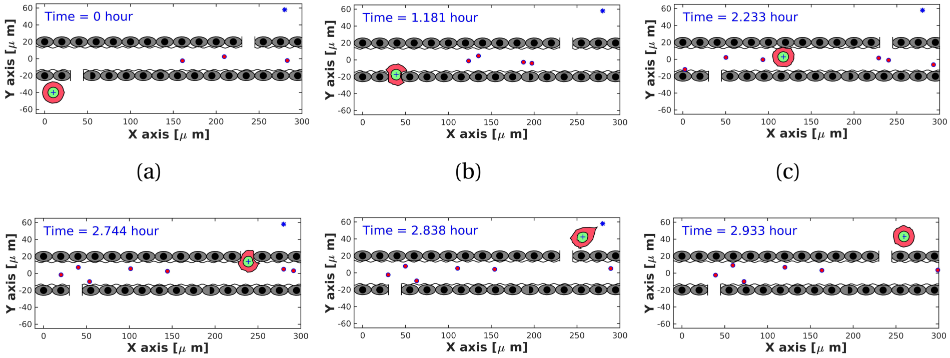

(a) (b) (c)

(d) (e) (f)

Figure 5.7: Consecutive snapshots of one cell about intravasation and extravasation of a blood or lymphatic vessel in 2D simulation. The migrating cell, nucleus and the vessel are visualized by red, green and grey colors, respectively. A blue asterisk denotes any type of sources. The CPU time of this model is 355.09 seconds.

We model the intravasation of a metastatic cell through a preexisting pore in endothelium, where the exact underlying mechanism is still poorly understood. Some studies suggest that cell intravasation is regulated by tumor-stromal cell interactions [254], biochemical factors (like tumor necrosis factor alpha TNF-α) or other cell-cell communications [255]. Therefore, we assume that a cancer cell is attracted to translocate into the bloodstream by a biochemical signal (see Figure 5.7(a)). Due to the flow of microfluid in the vessel, the migrating cell is advected at a velocity whenever subject to the flow. Note that there is no slip on the vessel wall, hence the blood velocity is zero on the vessel boundaries. To visualize the blood flow, some imaginary particles indicated in red color have been plotted in Figure 5.7, which have no influence on the migrating cell. Subsequently, the cell is capable of moving towards the emitting source (chemokine or stiffness) to complete the extravasation in Figure 5.7(d). Once the source is engulfed, the cancer cell is no longer mechanically deformed and hence the cell (and also its nucleus) returns to its equilibrium circular shapes.

Furthermore, the cell speed evolution of this model is shown in Figure 5.8(b), the speed is around 200 μm/hour in the channel and reaches to a peak instantaneously when the cell gets close to the source. The reason for this peak is the singularity in Equation (5.2) at the position of the source, which gives a very large gradient of the concentration near the source. This peak could be regularised by either adding a time-dependency (through an analytic solution or through a numerical solution of the concentration) or by replacing the chemotaxis by a factor such that the velocity stays bounded. All these approaches make the model more complication and since the objective was a construct a simple model, this has been omitted. At the final stages, the speed decreases to zero due to lack of attraction signals and the vector Wiener process. We also remark that the large variations in Figure 5.8(b) are caused by the cell having to pass through the apertures and having to migrate along the wall of the channel. This interaction between the cell boundary and obstacle causes the switch between repulsion and migration along the tangent of the obstacle and attraction as a result of a component normal to the tangent of the boundary of the obstacle. This effect of this discontinuous switch mechanism can only be inhibited by choosing a smaller time step.

5.4.4. PARAMETER STUDY WITH MONTE CARLO SIMULATIONS

If certain input values contain uncertainties, Monte Carlo simulations could be a way to evaluate the impacts of output. This method enables us to estimate of the impact from variables ranging from various statistical distributions like Pareto, uniform, normal, lognormal, chi-square, exponential, etc. [167]. Furthermore, Monte Carlo simulations have been used over a spectrum of systems, which is typically concluded in the following four steps, 1) generate the input random values based on their probability distribution functions; 2) calculate samples; 3) repeat the above-mentioned steps with a number of trials N_s; 4) calculate the

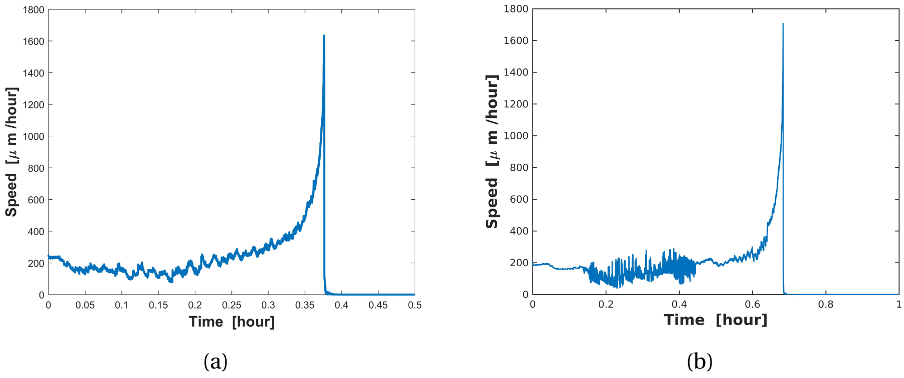

(a) (b)

Figure 5.8: (a).The cell speed evolution in cell penetration model (Figure 5.6); (b) The cell speed evolution in cell metastasis model (Figure 5.7).

mean and construct a relative frequency distribution of the simulated results [167, 256]. Furthermore, one can estimate the correlation between the various input and output parameters.

The model introduced in the Section 5.4.3 is used in Monte Carlo simulations, with the channel boundary of 60 μm in length and approximately 10 μm in width. The transit time interval that starts once one of the cell's boundary points enters the channel and lasts until the last point exits the channel is defined as the penetration time τ. In this section, the influences of several parameters on the penetration time τ are investigated.

As we discussed in the Section 5.3.4, the accuracy of the simulation result depends on the number of samples. To achieve an accurate approximation, the number of samples is tested that is shown in Figure 5.9.

Note that the axes represent the logarithm of sample count and the mean of transit time, respectively. If the sample count in the Monte Carlo simulations is too small, then the average penetration time has not yet converged (see Figure 5.9 for $N_s < 200$). We observe that using 10000 samples only gives very small fluctuations in the average penetration time (see Figure 5.9). The result has converged sufficiently to approximate 0.356 hour. However, to evaluate the uncertainty of input data quantitatively, 10000 samples are chosen in our simulation which gives acceptable computation times in the order of hour. Using Equation (5.31), the Monte Carlo error is estimated by $\|E_{mc}\| = \|\hat{\tau}^{\Delta t} - \hat{\tau}^{\Delta t}_{N_s}\| \simeq \frac{S_n}{\sqrt{N_s}}$.

MONTE CARLO SIMULATIONS ON PARAMETERS D, β, α, α^n

We start with the Monte Carlo simulations on four input parameters which are the diffusion coefficient of the chemokine D, cell point mobility β, cell deforma-

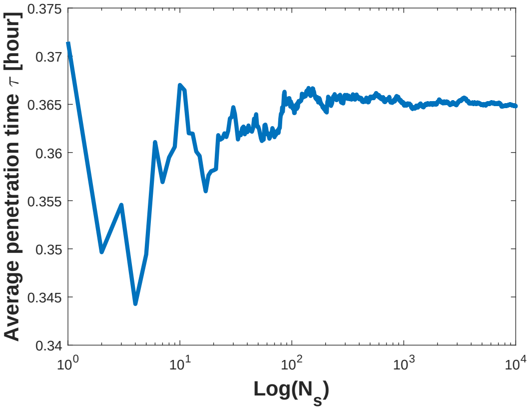

Figure 5.9: Sample quantity test for convergence of average penetration time τ. The penetration time is in hours.

tion relaxation α and the nucleus deformation relaxation α^n. We sample them from the normal distribution, then they can be generated by Equation (5.28) with the default values in Table 5.3. The mean value of each is the same as the value in

Table 5.3: Parameter values

-	D	β	α	α^n
Value	$N \sim (600, 30^2)$	$N \sim (60, 3^2)$	$N \sim (250, 40^2)$	$N \sim (2500, 125^2)$

Table 5.1 and corresponding standard deviation reflects the degree of dispersion among samples. The values have been chosen mathematically based on extensive testing. In Figure 5.10, we plot a histogram of 10000 samples as well as a cumulative distribution function (CDF) of the estimated probability of penetration time τ. Thence, the x-axis denotes the consecutive variable penetration time τ and the y-axis represents the frequency of occurrence or the probability $P_n(t \le \tau)$ of the corresponding variable depending on the chart considered in Figure 5.10.

Taking different roughnesses of the channel boundary into consideration, various values of ϵ ($\epsilon = 0,\ 0.5,\ 1.0,\ 1.5\ \mu$m) and ω ($\omega = 0,\ 0.25,\ 0.5,\ 0.75\ \mu m^{-1}$) are set and compared in Figure 5.11. The ϵ parameter manifests the magnitude of vertical fluctuation, i.e. the amplitude; while ω determines the frequency of the fluctuations of the boundary. A smooth boundary has a small ω value, then one cell is able to move through it much faster than through a rough channel. In Figure 5.11(a), we observe four cumulative distribution functions with different slopes $f(\tau)$, which represents the probability density. Thus, any probability

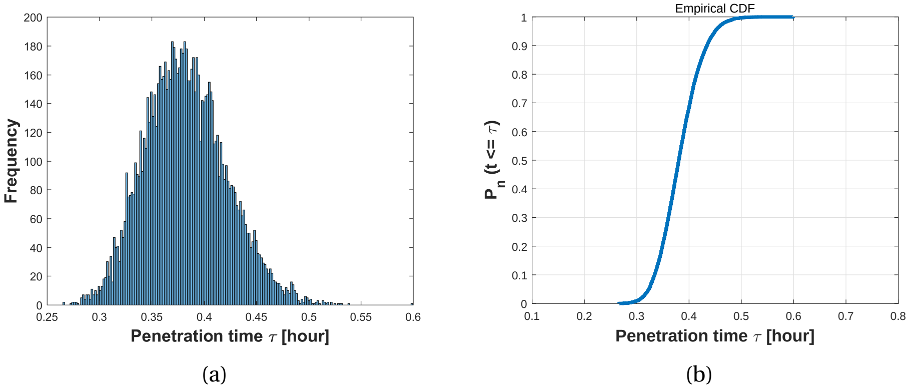

(a) (b)

Figure 5.10: The histogram (a) and CDF plot (b) of cell penetration time τ in Monte Carlo simulations on parameters D, β, α, α^n.

P_n of a time interval $[\tau - \frac{\Delta t}{2}, \tau + \frac{\Delta t}{2}]$ occurring can be calculated by the formula $P_n(\tau - \frac{\Delta t}{2} \leq \hat{\tau} \leq \tau + \frac{\Delta t}{2}) \approx f(\tau) \cdot \Delta t$. Conversely, with the same probability, taking $P_n = 0.5$ for an example, we can get the information about the transit time of one cell with 50% probability in various conditions, where $\tau_1(\epsilon = 0\ \mu\text{m}) < \tau_2(\epsilon = 0.5\ \mu\text{m}) < \tau_3(\epsilon = 1.0\ \mu\text{m}) < \tau_4(\epsilon = 1.5\ \mu\text{m})$. Analogously, Figure 5.11 (b) showing four cumulative distribution functions of the penetration time τ are compared under different conditions with varying ω. With 50 % probability, one cell takes penetration time τ_1 with a straight boundary $\omega = 0\ \mu\text{m}^{-1}$, the penetration time rises to τ_2, τ_3 and τ_4 with the increase in roughnesses $\omega = 0.25\ \mu\text{m}^{-1}$, $\omega = 0.5\ \mu\text{m}^{-1}$ and $\omega = 0.75\ \mu\text{m}^{-1}$, respectively. In conclusion, both the standard deviation in the arrival times and the mean arrival time increase with increasing values of ϵ and ω. Subsequently, we fix the roughness parameter values to $\epsilon = 1.0\ \mu\text{m}$ and $\omega = 0.5\ \mu\text{m}^{-1}$, then the impacts of four parameters $D, \beta, \alpha, \alpha^n$ on the penetration time τ are investigated and the correlation analysis are shown in Figure 5.12. Based on the results, there is some positive correlation between the penetration time τ and both D and α with correlation coefficient r equal to 0.6068 and 0.49772, respectively. Moreover, β has a negative linear correlation with τ, whereas, the nucleus deformation relaxation has no obvious correlation with penetration time in this situation. However, the nucleus is the stiffest cellular component, which inhibits the confined cell migration if the pore diameter in the ECM is below a critical threshold [223, 257]. Therefore, the correlation between the penetration time and nucleus stiffness is expected to be highly positive if the width of channel is smaller than a critical threshold.

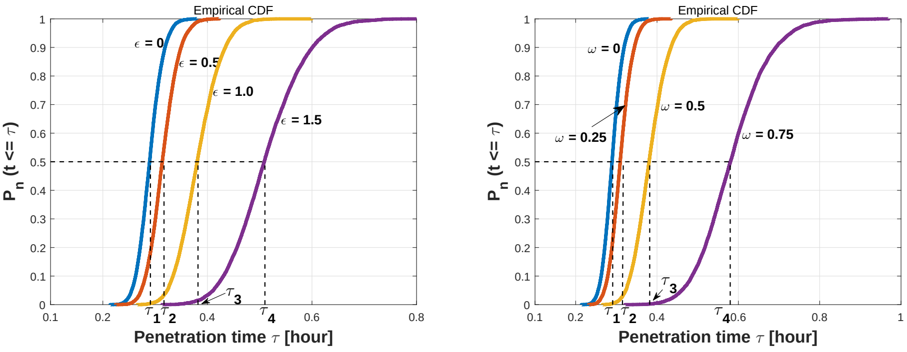

(a) (b)

Figure 5.11: Figure (a) compares the CDF plots of cell penetration time τ in terms of various ϵ (ϵ = 0, 0.5, 1.0, 1.5 μm) with a fixed ω value (ω = 0.5 μm^{-1}). Figure (b) compares the CDF plots of cell penetration time τ in terms of various ω (ω = 0, 0.25, 0.5, 0.75 μm^{-1}) with a fixed ϵ value (ϵ = 1.0 μm).

MONTE CARLO SIMULATIONS ON PARAMETERS ϵ AND ω

We next analyzed the other two parameters ϵ and ω, which reflect the amplitude and frequency of the channel boundary. Suppose ϵ and ω are too large, i.e. $\epsilon, \omega > 2$ in our simulations, the trigonometric functions probably would trap migrating cells due to sharp peaks or corners. Therefore, ϵ and ω are generated carefully with uniform normal distribution by the following equation,

$$\begin{cases} \epsilon & \sim \quad U(0.5,\ 1.5), \\ \omega & \sim \quad U(0,\ 0.6). \end{cases} \tag{5.38}$$

This above equation guarantees the value of ϵ and ω are uniformly distributed and bounded by (0.5, 1.5) and (0, 0.6). Based on the 10000 samples, Figure 5.13(a) shows the corresponding histogram, which looks like a log-normal chart and fits from a qualitative point of view with the experimental results by Abuhattum and Weihs [258], where the migration speeds of single preadipocytes without chemoattractants follow a log-normal distribution. A cumulative percentage of the number of occurrences regarding the cell penetration time τ is plotted in Figure 5.13(b).

Analogously, scatter diagrams about ϵ and ω with penetration time τ indicating their correlations are shown in Figure 5.14. With the increase of roughness, one cell travels a longer time to penetrate the channel in most cases. Furthermore, the increment of ω makes a contribution to the total travel time of one cell.

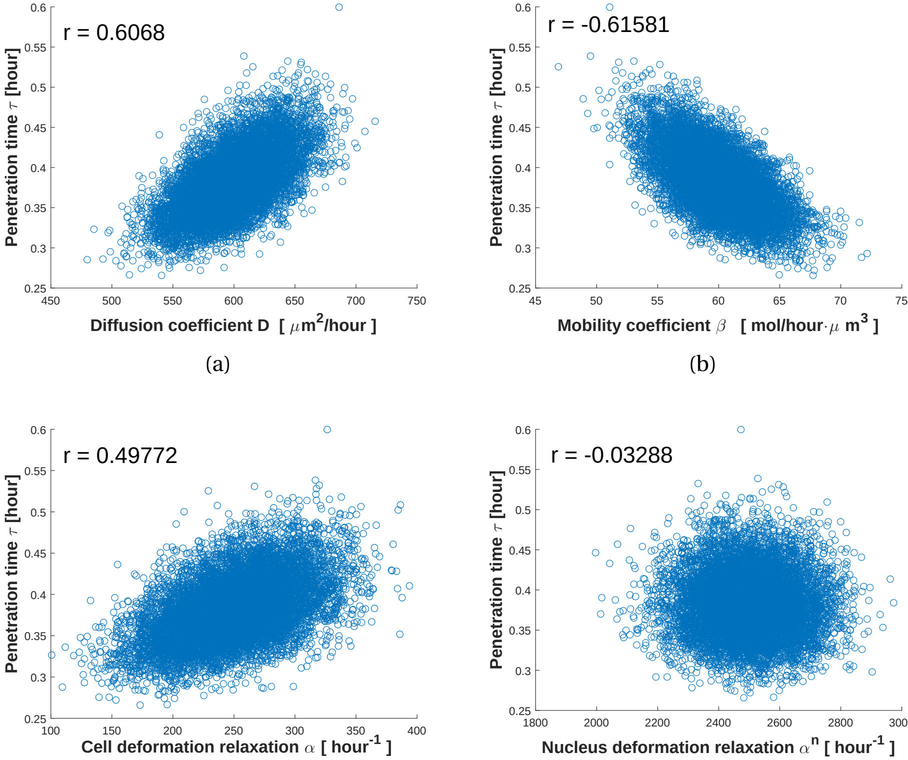

(a) (b)

(c) (d)

Figure 5.12: Scatter plots of cell penetration time τ with respect to various variables D, β, α, α^n.

This is also reflected by the correlations of $r = 0.4310$ and $r = 0.7100$ between the penetration time and ϵ and ω, respectively.

To test the essential variables simultaneously, all six parameters D, β, α, α^n, ϵ and ω are analyzed by Monte Carlo simulations. The histogram of the penetration time τ is shown in Figure 5.15(a) which can be fitted to a lognormal distribution. Furthermore, a CDF result is shown based on a sample of 10000 times simulations in Figure 5.15(b).

MONTE CARLO SIMULATIONS ON PARAMETERS D, β, α, α^n, ϵ AND ω

To investigate the impacts of variables on output results and analyze the correlations of each variable with penetration time τ, a couple of scatter plots are shown in Figure 5.16, respectively. Adding some control variables that are statistically distributed yields more uncertainty to the system. The increase in uncertainty generally decreases the correlation. Therefore, in the current simulation

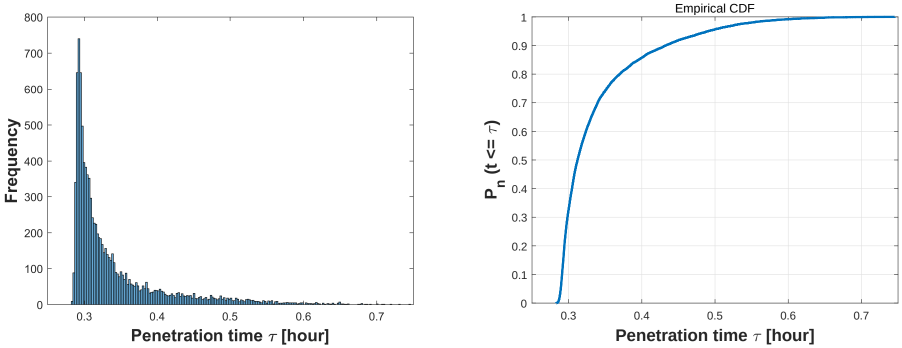

(a) (b)

Figure 5.13: The histogram (a) and CDF plot (b) of cell penetration time τ in Monte Carlo simulations on parameters ϵ and ω.

of six parameters, the correlation of parameters D, β, α, ϵ and ω with time τ decrease slightly compared with the simulations with the variation of four parameters. The correlation between τ and α^n is still negligible. Further, Figure 5.16 shows that the roughness (ϵ and ω) dominantly influences the cell travel time.

5.5. CONCLUSION AND DISCUSSION

In this chapter, we develop a cell-based model to describe the morphological evolution of the cell and nucleus in a phenomenological way. The cell cytoskeleton spanning between the nucleus and the cell membrane is simulated by 30 springs. As we expected, an immune cell or a single cancer cell can deform according to the specific obstacles or paths when it encounters a stiff obstacle in a 2D or 3D environment. Compared with some existing models, e.g. a model investigating the role of nucleus deformation in the cell deformation under different geometrical and fluid flow conditions [259] and a 3D model describing nucleus mechanics during cell migration and deformation [260], one of the major advantages of our modeling is its efficiency regarding CPU time, which enables to carry out Monte Carlo simulations for evaluation of parameter sensitivity. A further merit of the current model is its simplicity. If one is able measure the velocity of points on the surface of the cell under the influence of (the gradient of) a generic (being a concentration or a stiffness for instance) signal, then the β-parameter can be determined. If one further is able to measure the retraction speed on the boundaries of the cell and the nucleus once the signal has disappeared, then it can fit the α parameters.

The uncertainties in the input values necessitate us to study the impact of

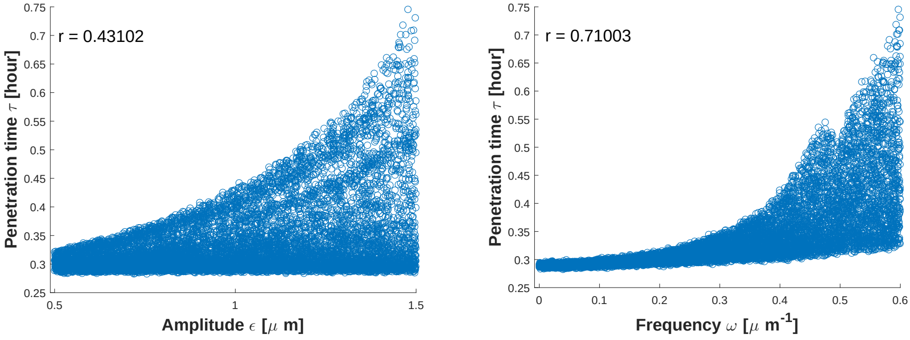

(a) (b)

Figure 5.14: Scatter plots about cell penetration time τ with respect to various variables ϵ and ω.

uncertainty by carrying out Monte Carlo simulations. With 10000 samples, the correlations of each variable D, β, α, α^n, ϵ and ω with cell penetration time τ are analyzed. The results show that α^n has no significant correlation with the penetration time in the current situation, where the reason probably is the low range of parametric values in our simulations. A larger range, with variations over a lognormal distribution could give a higher correlation. The use of very high values of α_n in the model when the cell is penetrating through an aperture needs more investigation. Moreover, Serrano-Alcalde *et al.* [259] state that a small cell nucleus does not play a crucial role in cell deformability-based experiments under fluid flow. Therefore, the deformability of the nucleus could be impacted by the size of the nucleus, and thereby influence the penetration time. Whereas, other variables influence the cell penetration time τ to varying degrees, where the correlation of roughness is the most significant.

To make the problem tractable, some assumptions are made based on the simplified biomedical phenomenon, which are: 1) the equilibrium morphology of the cell is circular in 2D and spherical in 3D, respectively; 2) the cell is not allowed to die, which means the cell cannot be removed, in any extreme narrow scenarios; 3) cell mobility is simulated by a source secreting a single cytokine evenly and continuously until it is consumed, which makes the model consist of a system of ordinary differential equations; 4) the obstacles are absolutely stiff such that they cannot deform and thereby we do not need to consider the degradation of substrate/ ECM on the obstacles. Further, the introduction of elastic obstacles also needs the inclusion of mechanical balance based on Newton's law for the objects. Although this would be an interesting extension of the model, we omit this in the current chapter since this extension enlarges the parameter

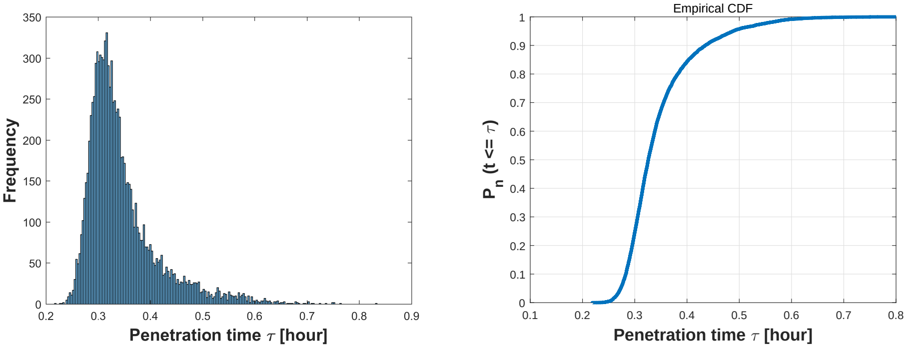

(a) (b)

Figure 5.15: The histogram (a) and CDF plot (b) of cell penetration time τ in Monte Carlo simulations on parameters D, β, α, α^n, ϵ and ω.

space for the Monte Carlo simulations. In order to improve the model, the following aspects could be considered in future work.

- Compared to a 2D model, a 3D model is more physiological, however, there is no significant qualitative difference in terms of expected numerical results. Moreover, taking the Monte Carlo simulations into account, the CPU time for simulating the 2D model is much more reasonable. However, a 3D model will still be an interesting research direction in the future.

- Amoeboid and mesenchymal movement, as the two basic forms of cell locomotion, mutually transform and participate in the process of cell migration. The former is also called pseudopodia movement including lamellipodia and filopodia, which normally takes place close to the cell front as a result of cell polarization [211, 239, 261]. Since the interconversion between the amoeboid model and the mesenchymal model due to the cytoskeleton rearrangement happens during cancer cell migration [262], the filopodia that is an extension of the active membrane of cell front and rear might be considered in future work.

- In the current work, we define constant values for the cell deformation relaxation α and cell mobility β everywhere, while they in general depend on chemokines. Therefore, to introduce surface-resident chemical species, some surface partial differential equations can be incorporated such that it describes the evolution of the chemical signals over the membrane sur-

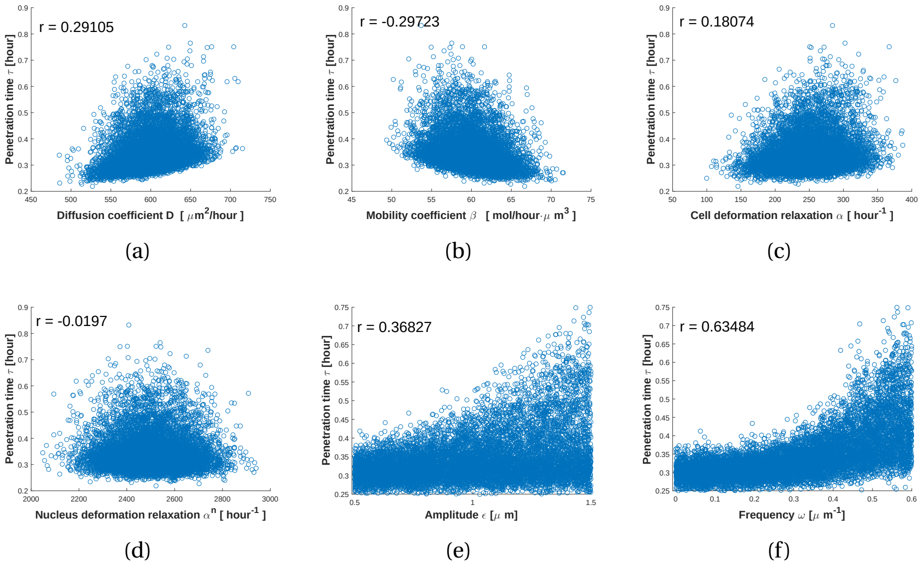

(a) (b) (c)

(d) (e) (f)

Figure 5.16: Scatter plots about cell penetration time τ with respect to various variables.

face. This amounts to solving

$$\begin{aligned} &\underline{a}_t + \nabla_\Gamma \cdot (\mathbf{v}\underline{a}) - D_a \Delta_\Gamma \underline{a} = \underline{f}(\underline{a}), \\ &\mathbf{v} = \frac{\mathrm{d}}{\mathrm{d}t}\underline{x}(t), \qquad (t, \mathbf{x}(t)) \in \mathbb{R}^+ \times \Gamma(t). \end{aligned} \tag{5.39}$$

This is an interesting and relevant research direction, which will be taken into consideration in future work.

- A tumor is typically surrounded by a dense network of collagen fibers, which are normally utilized by motile cancer cells to guide their paths [263]. Furthermore, mutated cancer cells are capable of remodeling the normal ECM around them, abnormal ECM or the density of fibers preferably reshapes aligned direction in a parallel arrangement, which forms an anisotropic medium and thereby has a significant impact on cell migration. If we formalize this directional dependence through the so-called orientation tensor Ψ. Then we get the following revision on the response to the external signal of the migration equations:

$$\begin{aligned} \mathrm{d}\mathbf{x}_i(t) = (\beta_0 \mathbf{I} + \beta_1 \Psi)\nabla c(t, \mathbf{x_i}(t))\mathrm{d}t + \alpha(\mathbf{x}_i^n(t) + \hat{\mathbf{x}}_i - \mathbf{x}_i(t))\mathrm{d}t + \eta \mathrm{d}\mathbf{W}(t), \\ i \in \{1, \ldots, N\}, \end{aligned} \tag{5.40}$$

where β_0 and β_1 are two constants and Ψ can be obtained by

$$\Psi(t,\mathbf{x}) = \begin{pmatrix} \Psi_{xx} & \Psi_{xy} \\ \Psi_{xy} & \Psi_{yy} \end{pmatrix}. \tag{5.41}$$

For the formalism, one can refers to the work by Cumming *et al.* [98] and a further application in the work [264].

- We note that the relaxation parameter of the nucleus has little correlation with the transmigration time. This finding seems counter-intuitive. According to the studies of [259], the stiffness of the nucleus hardly plays a role in cell-deformability experiments if the nucleus is relatively small. However for larger sizes, this deformability of the nucleus may become more important.

Over the past several decades, significant progress has been made in medical technology and attempts have been made to investigate the complexity of cancer initiation and progression. For example, cell deformability has been shown to have certain correlations with disease states of cells and metastatic potentials [240, 265]. Nonetheless, the biological mechanisms of a multi-step metastatic cancer still remain poorly understood [214]. To make a contribution, our group will continue to work on biological mathematical modeling to predict the behavior of cells in the microenvironment and aid the biological experiments for the further understanding of cancer and drug development.

6

CONCLUSION AND DISCUSSION

6.1. CONCLUSION

Mathematical simulations with a wide range of techniques can be applied to many different practical problems and its importance on cancer research has been increasingly recognized in recent decades. Differential equation-based continuum models are able to cover relevant scales from 10^2 μm to 10 cm, whereas hybrid models including cellular automata, and agent-based techniques can span scales from microns to millimeters [34]. Normally, mathematical modeling is a process of several steps: 1) choose a specific problem and computational domain; 2) make some simplifications using assumptions and convert this real-world problem to a mathematical problem through quantification; 3) establish mathematical equations, which enable to describe the relationship between the relevant quantities; 4) calculate the solution to the actual problem quickly and accurately using computing technology, software and other tools. Certainly, a sound mathematical model in this context must be analyzed (i.e. well-posedness, stability, error, etc.), validated in vitro or in vivo and applied to obtain further understanding of the fatal disease or any other biophysical or biomedical phenomenon.

CONCLUSIONS ON CHAPTER 2

Specific T-lymphocytes play an essential role in anti-tumor response in cancer. However, pancreatic cancer has immune tolerance, where T-lymphocytes are trapped in the desmoplastic stroma that hardly can neutralize cancer cells. In Chapter 2, our cell-based model presents the T-lymphocytes mediated immune response in pancreatic cancer at early stages. The model quantifies the delay of invasion of T-lymphocytes, which is caused by the stromal orientation and predicts the potential cancer progression in patients with different strengths of immune response.

The migration of T-lymphocytes is cytokines-driven chemotaxis modeled by solving a steady-state reaction-diffusion equation, whereas, mechanotaxis of other cells' movement is dealt with using the strain energy density. An orientation tensor and a vector Wiener process are used to simulate the anisotropic guidance of desmoplastic stroma and random walk of cells. To update the displacement of cells, a large system of stochastic differential equations is solved by the classical Euler-Maruyama method.

CONCLUSIONS ON CHAPTER 3

Based on the numerical results in Chapter 2, early targeted treatment can obviously increase the likelihood of success of pancreatic cancer therapy. Therefore, we extend the model to a stage of treatment in Chapter 3, where two different drugs are given at an early stage. The model shows that the drug PEGPH20 breaks down the orientation of desmoplastic stroma and the drug gemcitabine slows down the proliferation of cancer cells. In addition, the cell-based model predicts the therapeutic effects of various strategies including various drug doses and different times when treatment starts.

Analogously, the migration of cells is modeled by using a large system of stochastic differential equations. For diffusion of drug, the steady-state reaction-diffusion equation is taken into consideration, which is solved based on Green's fundamental solutions. Moreover, Monte Carlo simulations are performed to quantitatively investigate the propagation of uncertainties in the input parameters, which predicts the likelihood of a successful therapy with various diagnosis stages and treatment strategies.

CONCLUSIONS ON CHAPTER 4

In Chapter 4, we set up a cellular automata model that is different from the cell-based model. Cellular automata models enable each computational lattice point to be occupied by one cell or multiple cells, which upscales the simulation to a tissue level. The model successfully exhibits pancreatic cancer progression at an early stage and subsequent cancer recession under application of oncolytic virotherapy in a tissue level. Taking the viral toxicity into account, this model also investigates the viral therapeutic effects in various scenarios and residual viruses.

The fundamental cell processes (like cell mutation, cell proliferation, etc.) is modeled by using probabilistic principles. The virus is injected intratumorally and its diffusion is modeled by the time-depended reaction-diffusion equation, which is discretized by the finite difference method and integrated by the IMEX approach. Furthermore, Monte Carlo simulations are used to investigate the influences of input parameters on numerical results.

CONCLUSIONS ON CHAPTER 5

In previous chapters, the shape of cells are fixed circular, however, Chapter 5 presents a cell-based deformable model. The model phenomenologically shows the morphological evolution of the cell and its nucleus when encountering stiff obstacles. To mimic cancer metastasis, a microvascular bloodstream is incorporated and the cancer cell shows a dynamic cell shape. This chapter also gives the estimation of the likelihood of (cancer) cell metastasis.

Cells are attracted by an imaginational source (like chemokine or stiffness signal), which is dealt with using Dirac delta functions and Green's fundamental solutions. To mimic the deformable shape of the cell and its nucleus, each cell boundary is treated as a collection of a series of nodal points, and springs connecting the cell boundary and nucleus. To update the location of each nodal point, an IMEX-time integration method is used and parameters are quantitatively studied with Monte Carlo simulations. Moreover, the error of the IMEX-time integration method and Monte Carlo simulations are analyzed in this chapter.

6.2. DISCUSSION

Since biomedical studies often involve extensive experimental data in terms of patterns and numbers, the quantified hypotheses pose mathematical challenges, which are the backbone of mathematical models. The mathematical models can be used to investigate case studies that do not exactly fit within the experimental outcomes. A major advantage of mathematical modeling is that the number of animals or in vitro experiments can be reduced. Many mathematical models are based on the abstraction of biological phenomena into sets of partial differential equations, stochastic processes or even combinations of both. The approximate solutions are obtained by using numerical methods such as combinations of time integration, finite element methods, Green's functions, or using stochastic processes. In the case of probabilistic models, the model results need a statistical assessment in terms of intervals of confidence, correlations or other statistical tests.

In our future studies, we will develop models with more physiological features, such as the formation of abnormal stroma caused by cancer, the interaction of innate immunity and adaptive immunity for cancer, angiogenesis and network models for cancer metastasis, as well as other processes. Through the combination of various stages of the models of cancer, the complete model is expected to be applied in various aspects of cancer research. To keep the CPU time of the model low, a small number of cells is considered in two and three dimensions currently. However, parallel computing makes it possible to increase the number of cells in size to achieve large-scale quantitative simulation of cells. Therefore, we might use parallel computing facilities to simulate human tissue and even organs in a 3D environment to make the model as realistic as possible.

Existing models by us and others will also need to be expanded to include more complexity and physiological aspects. One aspect is sensitivity analysis of input values, due to the uncertainties, the study of parametric variation is crucially important. In our statistical evaluation of results, we use Monte Carlo simulations, which enable us to simultaneously and quantitatively investigate the input variables and correlations among them [167, 256]. It could be useful to compare our statistical outcomes in terms of probabilities, correlations and significance with large data sets from experimental and clinical studies and to investigate whether similar trends arise.

Another important matter is the accessibility to realistic values of the input parameters, currently most of the parameters in our simulations have been chosen on the basis of the literature or by estimation. Hopefully, more realistic input values will be available to us such that we are able to validate our modeling results better with available experimental outcomes. Thence it is crucial to cooperate with biomedical labs or hospitals to realize the validation, evaluation and application of our models, which definitely enable to enhance further understanding of the progression and inhibition of cancer. Another important issue concerns the variations of the input from patient to patient due to age, genetic pattern, lifestyle and gender. This makes that many of the simulated results contain uncertainties despite possibly well-measured data in generic patients. These uncertainties require a probabilistic modeling approach and hence a statistical assessment of the simulation results is indispensable.

Last but not least, next to common surgical therapies where tumors are removed or where chemotherapy is applied, therapies could be directed to paralyzing cancer cells in terms of motility and invasiveness by reducing cell deformability and/or by reducing the durotactic signal through de-stiffening certain body parts. Further treatments could target cancer cells by decreasing their proliferation rate and by increasing mortality rates. This is often done in chemotherapies. Alternatively, one could investigate and quantify the treatment of cancers by Nano-particles that only target the cancer cells. Modeling studies and frameworks could help investigate the impact and feasibility of the aforementioned treatments. Our cellular automata model for oncolytic virotherapy could be a starting point for these modeling studies.

In this thesis, we illustrated the importance of mathematical modeling to the cancer research community. A large advantage of mathematical modeling is the availability of a tool to predict outcomes from conditions that are beyond the measured and observed values. Biological and clinical researchers normally have limited training in mathematics, conversely, applied mathematicians often poorly understand the complicated multiscale dynamics that characterize the processes studies in the life sciences [5]. As a fact, typically medical biologists and clinicians show little interest in mathematical modeling, and thereby limited data are accessible to mathematicians. Another problem is that often mathematical modelers ask for parameters that are hard or even impossible to measure by medical biologists.

The evolutionary nature of cancer is undoubtedly important for oncologists to hack cancer disease, where mathematical modeling is able to aid us to obtain a better understanding of how cancer evolves and how it adapts to the environment. Moreover, mathematical modeling can help clinicians optimize the drug treatment strategies, and further do the pre-validation studies on a computer with a few seconds before administering therapy to patients [6]. This can also be helpful for experimentalists to reduce the number of clinical trials on animals or humans. At later stages, the mathematical models will be used to improve existing therapies and to quantify the impact of new therapies against cancer. To summarize, mathematical modeling has brought new insights into the underlying mechanisms of cancer evolution and provides prospects for oncology research and it facilitates a decrease in the number of animal experiments.

REFERENCES

REFERENCES

[1] J. Chen, D. Weihs, and F. J. Vermolen, *Computational cell-based modeling and visualization of cancer development and progression,* in *New Developments on Computational Methods and Imaging in Biomechanics and Biomedical Engineering* (Springer, 2019) pp. 93–119.

[2] A. Jemal, F. Bray, M. M. Center, J. Ferlay, E. Ward, and D. Forman, *Global cancer statistics,* CA: a cancer journal for clinicians **61**, 69–90 (2011).

[3] E. Commission, *Animals used for scientific purposes,* (2016).

[4] C. A. Reinhardt, *Alternatives to animal testing: new ways in the biomedical sciences, trends and progress.* .

[5] R. A. Gatenby, *Mathematical modeling in cancer,* in *Biomedical Informatics for Cancer Research* (Springer, 2010) pp. 139–147.

[6] K. Gammon, *Mathematical modelling: Forecasting cancer,* Nature **491**, S66–S67 (2012).

[7] D. W. Thompson *et al.*, *On growth and form.* On growth and form. (1942).

[8] E. R. Fearon and B. Vogelstein, *A genetic model for colorectal tumorigenesis,* Cell **61**, 759–767 (1990).

[9] R. A. Gatenby and T. L. Vincent, *An evolutionary model of carcinogenesis,* Cancer Research **63**, 6212–6220 (2003).

[10] T. L. Vincent and R. A. Gatenby, *An evolutionary model for initiation, promotion, and progression in carcinogenesis,* International journal of oncology **32**, 729–737 (2008).

[11] R. Friedman, K. Boye, and K. Flatmark, *Molecular modelling and simulations in cancer research,* Biochimica et Biophysica Acta (BBA)-Reviews on Cancer **1836**, 1–14 (2013).

[12] W. Im, S. Seefeld, and B. Roux, *A grand canonical monte carlo–brownian dynamics algorithm for simulating ion channels,* Biophysical Journal **79**, 788–801 (2000).

[13] C. Chen and B. M. Pettitt, *The binding process of a nonspecific enzyme with dna,* Biophysical journal **101**, 1139–1147 (2011).

[14] K. Spiegel and A. Magistrato, *Modeling anticancer drug–dna interactions via mixed qm/mm molecular dynamics simulations,* Organic & biomolecular chemistry **4**, 2507–2517 (2006).

[15] A. G. Turjanski, G. Hummer, and J. S. Gutkind, *How mitogen-activated protein kinases recognize and phosphorylate their targets: A qm/mm study,* Journal of the American Chemical Society **131**, 6141–6148 (2009).

[16] D. Drasdo and S. Höhme, *A single-cell-based model of tumor growth in vitro: monolayers and spheroids,* Physical biology **2**, 133 (2005).

[17] H. Byrne and D. Drasdo, *Individual-based and continuum models of growing cell populations: a comparison,* Journal of mathematical biology **58**, 657–687 (2009).

[18] K. A. Rejniak, *An immersed boundary framework for modelling the growth of individual cells: an application to the early tumour development,* Journal of theoretical biology **247**, 186–204 (2007).

[19] F. Vermolen and A. Gefen, *A phenomenological model for chemico-mechanically induced cell shape changes during migration and cell–cell contacts,* Biomechanics and modeling in mechanobiology **12**, 301–323 (2013).

[20] A. Madzvamuse and U. Z. George, *The moving grid finite element method applied to cell movement and deformation,* Finite Elements in Analysis and Design **74**, 76–92 (2013).

[21] C. M. Elliott, B. Stinner, and C. Venkataraman, *Modelling cell motility and chemotaxis with evolving surface finite elements,* Journal of The Royal Society Interface , rsif20120276 (2012).

[22] J. Murray, *Mathematical biology ii: Spatial models and biomedical applications (3rd editio),* (2003).

[23] Y. Merkher and D. Weihs, *Proximity of metastatic cells enhances their mechanobiological invasiveness,* Annals of Biomedical Engineering , 1–8 (2017).

[24] M. K. Jolly, M. Boareto, B. G. Debeb, N. Aceto, M. C. Farach-Carson, W. A. Woodward, and H. Levine, *Inflammatory breast cancer: a model for investigating cluster-based dissemination,* npj Breast Cancer **3**, 21 (2017).

[25] M. Dudaie, D. Weihs, F. Vermolen, and A. Gefen, *Modeling migration in cell colonies in two and three dimensional substrates with varying stiffnesses,* In Silico Cell and Tissue Science **2**, 2 (2015).

[26] T. Da-Jun, F. Tang, T. Lee, D. Sarda, A. Krishnan, and A. Goryachev, *Parallel computing platform for the agent-based modeling of multicellular biological systems,* in *PDCAT* (Springer, 2004) pp. 5–8.

[27] D. Siemann, *Vascular targeting agents. horizons in cancer therapeutics: From bench to bedside,* Cancer **3**, 4–15 (2002).

[28] J. Forkman, *Tumor angiogenesis: Role in regulation of tumor growth,* Syrup Soc Dev Biol **30**, 43–52 (1974).

[29] J. Chen and F. Vermolen, *Literature study on cell-based semi-stochastic modelling for the dynamics of growth of cell colonies,* (2016).

[30] F. Vermolen, R. Van der Meijden, M. Van Es, A. Gefen, and D. Weihs, *Towards a mathematical formalism for semi-stochastic cell-level computational modeling of tumor initiation,* Annals of biomedical engineering **43**, 1680–1694 (2015).

[31] H. Enderling, A. R. Anderson, M. A. Chaplain, A. J. Munro, and J. S. Vaidya, *Mathematical modelling of radiotherapy strategies for early breast cancer,* Journal of Theoretical Biology **241**, 158–171 (2006).

[32] J. Folkman and C. Haudenschild, *Angiogenesis in vitro,* (1980).

[33] N. Savage, *Modelling: computing cancer,* Nature **491**, S62–S63 (2012).

[34] A. Shirinifard, J. S. Gens, B. L. Zaitlen, N. J. Popławski, M. Swat, and J. A. Glazier, *3d multi-cell simulation of tumor growth and angiogenesis,* PloS one **4**, e7190 (2009).

[35] L. Rens, S. Boas, and R. Merks, *Modelling the growth of blood vessels in health and disease,* ERCIM News , 36–37 (2016).

[36] M. A. Chaplain, *Mathematical modelling of angiogenesis,* Journal of neurooncology **50**, 37–51 (2000).

[37] S. R. McDougall, A. R. Anderson, and M. A. Chaplain, *Mathematical modelling of dynamic adaptive tumour-induced angiogenesis: clinical implications and therapeutic targeting strategies,* Journal of theoretical biology **241**, 564–589 (2006).

[38] A. Stephanou, S. R. McDougall, A. R. Anderson, and M. A. Chaplain, *Mathematical modelling of flow in 2d and 3d vascular networks: applications to anti-angiogenic and chemotherapeutic drug strategies,* Mathematical and Computer Modelling **41**, 1137–1156 (2005).

[39] C. L. Chaffer and R. A. Weinberg, *A perspective on cancer cell metastasis,* Science **331**, 1559–1564 (2011).

[40] C. A. Reinhart-King, M. Dembo, and D. A. Hammer, *Cell-cell mechanical communication through compliant substrates,* Biophysical journal **95**, 6044–6051 (2008).

[41] F. Vermolen and A. Gefen, *A semi-stochastic cell-based formalism to model the dynamics of migration of cells in colonies,* Biomechanics and modeling in mechanobiology **11**, 183–195 (2012).

[42] C. C. DuFort, M. J. Paszek, and V. M. Weaver, *Balancing forces: architectural control of mechanotransduction,* Nature reviews Molecular cell biology **12**, 308–319 (2011).

[43] J. Winer, A. Chopra, J. Kresh, and P. Janmey, *Mechanobiology of cell–cell and cell–matrix interactions. ch. 2,* (2011).

[44] S. Massalha and D. Weihs, *Metastatic breast cancer cells adhere strongly on varying stiffness substrates, initially without adjusting their morphology,* Biomechanics and Modeling in Mechanobiology , 1–10 (2016).

[45] R. Kristal-Muscal, L. Dvir, and D. Weihs, *Metastatic cancer cells tenaciously indent impenetrable, soft substrates,* New Journal of Physics **15**, 035022 (2013).

[46] M. D. Ryser and S. V. Komarova, *Mathematical modeling of cancer metastases,* Computational Bioengineering , 211 (2015).

[47] I. Ramis-Conde, M. A. Chaplain, and A. R. Anderson, *Mathematical modelling of cancer cell invasion of tissue,* Mathematical and Computer Modelling **47**, 533–545 (2008).

[48] S. Turner and J. A. Sherratt, *Intercellular adhesion and cancer invasion: a discrete simulation using the extended potts model,* Journal of Theoretical Biology **216**, 85–100 (2002).

[49] T. D. Tlsty and L. M. Coussens, *Tumor stroma and regulation of cancer development,* Annu. Rev. Pathol. Mech. Dis. **1**, 119–150 (2006).

[50] A. Simmons, P. M. Burrage, D. V. Nicolau, S. R. Lakhani, and K. Burrage, *Environmental factors in breast cancer invasion: a mathematical modelling review,* Pathology (2017).

[51] H. Enderling, A. R. Anderson, and M. A. Chaplain, *A model of breast carcinogenesis and recurrence after radiotherapy,* PAMM **7**, 1121701–1121702 (2007).

[52] H. Enderling, M. A. Chaplain, A. R. Anderson, and J. S. Vaidya, *A mathematical model of breast cancer development, local treatment and recurrence,* Journal of theoretical biology **246**, 245–259 (2007).

[53] G. Tanaka, Y. Hirata, S. L. Goldenberg, N. Bruchovsky, and K. Aihara, *Mathematical modelling of prostate cancer growth and its application to hormone therapy,* Philosophical Transactions of the Royal Society of London A: Mathematical, Physical and Engineering Sciences **368**, 5029–5044 (2010).

[54] H. Namazi, V. V. Kulish, and A. Wong, *Mathematical modelling and prediction of the effect of chemotherapy on cancer cells,* Scientific reports **5**, 13583 (2015).

[55] J. Couzin-Frankel, *Cancer immunotherapy,* (2013).

[56] I. Mellman, G. Coukos, and G. Dranoff, *Cancer immunotherapy comes of age,* Nature **480**, 480–489 (2011).

[57] D. Kirschner and J. C. Panetta, *Modeling immunotherapy of the tumor–immune interaction,* Journal of mathematical biology **37**, 235–252 (1998).

[58] N. Bellomo and L. Preziosi, *Modelling and mathematical problems related to tumor evolution and its interaction with the immune system,* Mathematical and Computer Modelling **32**, 413–452 (2000).

[59] L. Abbott and F. Michor, *Mathematical models of targeted cancer therapy,* British journal of cancer **95**, 1136–1141 (2006).

[60] D. Hanahan and R. A. Weinberg, *The hallmarks of cancer,* cell **100**, 57–70 (2000).

[61] J. Ferlay, I. Soerjomataram, M. Ervik, R. Dikshit, S. Eser, C. Mathers, M. Rebelo, D. Parkin, D. Forman, and F. Bray, *Globocan 2012 v1. 0, cancer incidence and mortality worldwide: Iarc cancerbase no. 11 [internet]. 2013; lyon, france: International agency for research on cancer,* globocan. iarc. fr/Default. aspx (2014).

[62] J. Chmielecki, J. Foo, G. R. Oxnard, K. Hutchinson, K. Ohashi, R. Somwar, L. Wang, K. R. Amato, M. Arcila, M. L. Sos, *et al.*, *Optimization of dosing for egfr-mutant non–small cell lung cancer with evolutionary cancer modeling,* Science translational medicine **3**, 90ra59–90ra59 (2011).

[63] Z. Wang, L. Zhang, J. Sagotsky, and T. S. Deisboeck, *Simulating non-small cell lung cancer with a multiscale agent-based model,* Theoretical Biology and Medical Modelling **4**, 50 (2007).

[64] F. Bianconi, E. Baldelli, V. Ludovini, L. Crinò, A. Flacco, and P. Valigi, *Computational model of egfr and igf1r pathways in lung cancer: a systems biology approach for translational oncology,* Biotechnology advances **30**, 142–153 (2012).

[65] W. Weens, *Mathematical modeling of liver tumor*, Ph.D. thesis, Université Pierre et Marie Curie-Paris VI (2012).

[66] G. Powathil, M. Kohandel, S. Sivaloganathan, A. Oza, and M. Milosevic, *Mathematical modeling of brain tumors: effects of radiotherapy and chemotherapy,* Physics in medicine and biology **52**, 3291 (2007).

[67] H. Hatzikirou, A. Deutsch, C. Schaller, M. Simon, and K. Swanson, *Mathematical modelling of glioblastoma tumour development: a review,* Mathematical Models and Methods in Applied Sciences **15**, 1779–1794 (2005).

[68] J. P. Ward and J. King, *Mathematical modelling of avascular-tumour growth,* Mathematical Medicine and Biology: A Journal of the IMA **14**, 39–69 (1997).

[69] T. Jackson, *A mathematical model of prostate tumor growth and androgen-independent relapse,* Discrete and continuous dynamical systems series B **4**, 187–202 (2004).

[70] K. A. Rejniak and R. H. Dillon, *A single cell-based model of the ductal tumour microarchitecture,* Computational and Mathematical Methods in Medicine **8**, 51–69 (2007).

[71] A. Jemal, T. Murray, E. Ward, A. Samuels, R. C. Tiwari, A. Ghafoor, E. J. Feuer, and M. J. Thun, *Cancer statistics, 2005,* CA: a cancer journal for clinicians **55**, 10–30 (2005).

[72] P. Van Liedekerke, M. Palm, N. Jagiella, and D. Drasdo, *Simulating tissue mechanics with agent-based models: concepts, perspectives and some novel results,* Computational Particle Mechanics **2**, 401–444 (2015).

[73] M. Block, E. Schöll, and D. Drasdo, *Classifying the expansion kinetics and critical surface dynamics of growing cell populations,* Physical review letters **99**, 248101 (2007).

[74] M. Radszuweit, M. Block, J. Hengstler, E. Schöll, and D. Drasdo, *Comparing the growth kinetics of cell populations in two and three dimensions,* Physical Review E **79**, 051907 (2009).

[75] D. H. Rothman and S. Zaleski, *Lattice-gas cellular automata: Simple models of complex hydrodynamics,* Vol. 5 (Cambridge University Press, 2004).

[76] R. Merks and P. Koolwijk, *Modeling morphogenesis in silico and in vitro: towards quantitative, predictive, cell-based modeling,* Mathematical Modelling of Natural Phenomena **4**, 149–171 (2009).

[77] R. F. van Oers, E. G. Rens, D. J. LaValley, C. A. Reinhart-King, and R. M. Merks, *Mechanical cell-matrix feedback explains pairwise and collective endothelial cell behavior in vitro,* PLoS Comput Biol **10**, e1003774 (2014).

[78] J. A. Glazier and F. Graner, *Simulation of the differential adhesion driven rearrangement of biological cells,* Physical Review E **47**, 2128 (1993).

[79] F. Vermolen, *Particle methods to solve modelling problems in wound healing and tumor growth,* Computational Particle Mechanics **2**, 381–399 (2015).

[80] M.-C. Kim, J. Whisler, Y. R. Silberberg, R. D. Kamm, and H. H. Asada, *Cell invasion dynamics into a three dimensional extracellular matrix fibre network,* PLoS Comput Biol **11**, e1004535 (2015).

[81] F. Ribeiro, M. Gómez-Benito, J. Folgado, P. Fernandes, and J. García-Aznar, *Computational model of mesenchymal migration in 3d under chemotaxis,* Computer methods in BiomeChaniCs and BiomediCal engineering **20**, 59–74 (2017).

[82] D. Drasdo and S. Hoehme, *A single-cell-based model of tumor growth in vitro: monolayers and spheroids,* Physical biology **2**, 133 (2005).

[83] H. Byrne and D. Drasdo, *Individual-based and continuum models of growing cell populations: a comparison,* Journal of mathematical biology **58**, 657–687 (2009).

[84] F. Vermolen and A. Gefen, *A semi-stochastic cell-based formalism to model the dynamics of migration of cells in colonies,* Biomechanics and modeling in mechanobiology **11**, 183–195 (2012).

[85] F. Vermolen and A. Gefen, *A semi-stochastic cell-based model for in vitro infected 'wound'healing through motility reduction: A simulation study,* Journal of theoretical biology **318**, 68–80 (2013).

[86] A. Madzvamuse and U. Z. George, *The moving grid finite element method applied to cell movement and deformation,* Finite Elements in Analysis and Design **74**, 76–92 (2013).

[87] C. Borau, W. J. Polacheck, R. D. Kamm, and J. M. García-Aznar, *Probabilistic voxel-fe model for single cell motility in 3d,* In silico cell and tissue science **1**, 1–17 (2014).

[88] F. Vermolen, M. Mul, and A. Gefen, *Semi-stochastic cell-level computational modeling of the immune system response to bacterial infections and the effects of antibiotics,* Biomechanics and modeling in mechanobiology **13**, 713–734 (2014).

[89] Y. Kim, M. A. Stolarska, and H. G. Othmer, *A hybrid model for tumor spheroid growth in vitro i: theoretical development and early results,* Mathematical Models and Methods in Applied Sciences **17**, 1773–1798 (2007).

[90] L. Yang, T. M. Witten, and R. M. Pidaparti, *A biomechanical model of wound contraction and scar formation,* Journal of theoretical biology **332**, 228–248 (2013).

[91] F. Milde, M. Bergdorf, and P. Koumoutsakos, *A hybrid model for three-dimensional simulations of sprouting angiogenesis,* Biophysical journal **95**, 3146–3160 (2008).

[92] J. Chen, D. Weihs, and F. J. Vermolen, *A model for cell migration in non-isotropic fibrin networks with an application to pancreatic tumor islets,* Biomechanics and modeling in mechanobiology **17**, 367–386 (2018).

[93] A. D. Rhim, P. E. Oberstein, D. H. Thomas, E. T. Mirek, C. F. Palermo, S. A. Sastra, E. N. Dekleva, T. Saunders, C. P. Becerra, I. W. Tattersall, *et al.*, *Stromal elements act to restrain, rather than support, pancreatic ductal adenocarcinoma,* Cancer cell **25**, 735–747 (2014).

[94] F. Angeli, G. Koumakis, M.-C. Chen, S. Kumar, and J. G. Delinassios, *Role of stromal fibroblasts in cancer: promoting or impeding?* Tumor Biology **30**, 109–120 (2009).

[95] B. C. Özdemir, T. Pentcheva-Hoang, J. L. Carstens, X. Zheng, C.-C. Wu, T. R. Simpson, H. Laklai, H. Sugimoto, C. Kahlert, S. V. Novitskiy, *et al.*, *Depletion of carcinoma-associated fibroblasts and fibrosis induces immunosuppression and accelerates pancreas cancer with reduced survival,* Cancer cell **25**, 719–734 (2014).

[96] H. Salmon and E. Donnadieu, *Within tumors, interactions between t cells and tumor cells are impeded by the extracellular matrix,* OncoImmunology **1**, 992–994 (2012).

[97] D. Hanahan and R. A. Weinberg, *Hallmarks of cancer: the next generation,* cell **144**, 646–674 (2011).

[98] B. D. Cumming, D. McElwain, and Z. Upton, *A mathematical model of wound healing and subsequent scarring,* Journal of The Royal Society Interface **7**, 19–34 (2010).

[99] J. H. Wang and J.-S. Lin, *Cell traction force and measurement methods,* Biomechanics and modeling in mechanobiology **6**, 361–371 (2007).

[100] C. A. Reinhart-King, M. Dembo, and D. A. Hammer, *Cell-cell mechanical communication through compliant substrates,* Biophysical journal **95**, 6044–6051 (2008).

[101] R. Kristal-Muscal, L. Dvir, M. Schvartzer, and D. Weihs, *Mechanical interaction of metastatic cancer cells with a soft gel,* Procedia IUTAM **12**, 211–219 (2015).

[102] R. Merkel, N. Kirchgeßner, C. M. Cesa, and B. Hoffmann, *Cell force microscopy on elastic layers of finite thickness,* Biophysical journal **93**, 3314–3323 (2007).

[103] A. Gefen, *Effects of virus size and cell stiffness on forces, work, and pressures driving membrane invagination in a receptor-mediated endocytosis,* Journal of biomechanical engineering **132**, 084501 (2010).

[104] S. Sen, A. J. Engler, and D. E. Discher, *Matrix strains induced by cells: computing how far cells can feel,* Cellular and molecular bioengineering **2**, 39–48 (2009).

[105] C. M. Nelson and C. S. Chen, *Cell-cell signaling by direct contact increases cell proliferation via a pi3k-dependent signal,* Febs Letters **514**, 238–242 (2002).

[106] C. S. Chen, M. Mrksich, S. Huang, G. M. Whitesides, and D. E. Ingber, *Geometric control of cell life and death,* Science **276**, 1425–1428 (1997).

[107] M. Malumbres and M. Barbacid, *Milestones in cell division: to cycle or not to cycle: a critical decision in cancer,* Nature Reviews Cancer **1**, 222–231 (2001).

[108] C. B. Harley, N. Kim, K. Prowse, S. Weinrich, K. Hirsch, M. West, S. Bacchetti, H. Hirte, C. Counter, C. Greider, *et al.*, *Telomerase, cell immortality, and cancer,* in *Cold Spring Harbor symposia on quantitative biology,* Vol. 59 (Cold Spring Harbor Laboratory Press, 1994) pp. 307–315.

[109] D. G. Stupack and D. A. Cheresh, *Get a ligand, get a life: integrins, signaling and cell survival,* Journal of cell science **115**, 3729–3738 (2002).

[110] L. Li, J. Backer, A. S. Wong, E. L. Schwanke, B. G. Stewart, and M. Pasdar, *Bcl-2 expression decreases cadherin-mediated cell-cell adhesion,* Journal of cell science **116**, 3687–3700 (2003).

[111] M. E. Warchol, *Cell density and n-cadherin interactions regulate cell proliferation in the sensory epithelia of the inner ear,* The Journal of neuroscience **22**, 2607–2616 (2002).

[112] P. A. Klekotka, S. A. Santoro, A. Ho, S. F. Dowdy, and M. M. Zutter, *Mammary epithelial cell-cycle progression via the α 2 β 1 integrin: Unique and synergistic roles of the α2 cytoplasmic domain,* The American journal of pathology **159**, 983–992 (2001).

[113] M. Delarue, F. Montel, D. Vignjevic, J. Prost, J.-F. Joanny, and G. Cappello, *Compressive stress inhibits proliferation in tumor spheroids through a volume limitation,* Biophysical journal **107**, 1821–1828 (2014).

[114] E. Farge, *Mechanical induction of twist in the drosophila foregut/stomodeal primordium,* Current biology **13**, 1365–1377 (2003).

[115] S. Kumar and V. M. Weaver, *Mechanics, malignancy, and metastasis: the force journey of a tumor cell,* Cancer and Metastasis Reviews **28**, 113–127 (2009).

[116] S. Huang and D. E. Ingber, *Cell tension, matrix mechanics, and cancer development,* Cancer cell **8**, 175–176 (2005).

[117] M. J. Paszek and V. M. Weaver, *The tension mounts: mechanics meets morphogenesis and malignancy,* Journal of mammary gland biology and neoplasia **9**, 325–342 (2004).

[118] H. Bougherara, A. Mansuet-Lupo, M. Alifano, C. Ngô, D. Damotte, M.-A. Le Frère-Belda, E. Donnadieu, and E. Peranzoni, *real-time imaging of resident t cells in human lung and ovarian carcinomas reveals how different tumor microenvironments control t lymphocyte migration,* Frontiers in immunology **6** (2015).

[119] D. Ruiter, T. Bogenrieder, D. Elder, and M. Herlyn, *Melanoma–stroma interactions: structural and functional aspects,* The lancet oncology **3**, 35–43 (2002).

[120] J. Van Damme, P. Proost, J.-P. Lenaerts, and G. Opdenakker, *Structural and functional identification of two human, tumor-derived monocyte chemotactic proteins (mcp-2 and mcp-3) belonging to the chemokine family.* The Journal of experimental medicine **176**, 59–65 (1992).

[121] M. H. Kershaw, G. Wang, J. A. Westwood, R. K. Pachynski, H. L. Tiffany, F. M. Marincola, E. Wang, H. A. Young, P. M. Murphy, and P. Hwu, *Redirecting migration of t cells to chemokine secreted from tumors by genetic modification with cxcr2,* Human gene therapy **13**, 1971–1980 (2002).

[122] M. P. Colombo and G. Trinchieri, *Interleukin-12 in anti-tumor immunity and immunotherapy,* Cytokine & growth factor reviews **13**, 155–168 (2002).

[123] C. A. Reinhart-King, M. Dembo, and D. A. Hammer, *Endothelial cell traction forces on rgd-derivatized polyacrylamide substrata,* Langmuir **19**, 1573–1579 (2003).

[124] A. Ganz, M. Lambert, A. Saez, P. Silberzan, A. Buguin, R. M. Mège, and B. Ladoux, *Traction forces exerted through n-cadherin contacts,* Biology of the Cell **98**, 721–730 (2006).

[125] J. Lindsey, N. I. McGill, L. A. Lindsey, D. K. Green, and H. J. Cooke, *In vivo loss of telomeric repeats with age in humans,* Mutation Research/DNAging **256**, 45–48 (1991).

[126] R. C. Allsopp, H. Vaziri, C. Patterson, S. Goldstein, E. V. Younglai, A. B. Futcher, C. W. Greider, and C. B. Harley, *Telomere length predicts replicative capacity of human fibroblasts,* Proceedings of the National Academy of Sciences **89**, 10114–10118 (1992).

[127] F. Bookholt, H. Monsuur, S. Gibbs, and F. Vermolen, *Mathematical modelling of angiogenesis using continuous cell-based models,* Biomechanics and modeling in mechanobiology , 1–24 (2016).

[128] T. Kalebic, S. Garbisa, B. Glaser, and L. Liotta, *Basement membrane collagen: degradation by migrating endothelial cells,* Science **221**, 281–283 (1983).

[129] J. Couzin-Frankel, *Cancer immunotherapy,* Science **342**, 1432–1433 (2013).

[130] J. Chen, D. Weihs, and F. J. Vermolen, *Computational modeling of therapy on pancreatic cancer in its early stages,* Biomechanics and modeling in mechanobiology , Accepted (2019).

[131] D. Li, K. Xie, R. Wolff, and J. Abbruzzese, *Pancreatic cancer,* The Lancet **363**, 1049–1057 (2004).

[132] H. Salmon and E. Donnadieu, *Within tumors, interactions between t cells and tumor cells are impeded by the extracellular matrix,* Oncoimmunology **1**, 992–994 (2012).

[133] P. Provenzano, C. Cuevas, A. Chang, V. Goel, D. Von Hoff, and S. Hingorani, *Enzymatic targeting of the stroma ablates physical barriers to treatment of pancreatic ductal adenocarcinoma,* Cancer cell **21**, 418–429 (2012).

[134] H. Shepard, *Breaching the castle walls: hyaluronan depletion as a therapeutic approach to cancer therapy,* Front Oncol **5**, 192 (2015).

[135] M. Jacobetz, D. Chan, A. Neesse, T. Bapiro, N. Cook, K. Frese, C. Feig, T. Nakagawa, M. Caldwell, H. Zecchini, *et al.*, *Hyaluronan impairs vascular function and drug delivery in a mouse model of pancreatic cancer,* Gut , gutjnl–2012 (2012).

[136] S. Moolgavkar and A. Knudson, *Mutation and cancer: a model for human carcinogenesis,* JNCI: Journal of the National Cancer Institute **66**, 1037–1052 (1981).

[137] N. Beerenwinkel, T. Antal, D. Dingli, A. Traulsen, K. Kinzler, V. Velculescu, B. Vogelstein, and M. Nowak, *Genetic progression and the waiting time to cancer,* PLoS Comput Biol **3**, e225 (2007).

[138] Y. Louzoun, C. Xue, G. Lesinski, and A. Friedman, *A mathematical model for pancreatic cancer growth and treatments,* J Theor Biol **351**, 74–82 (2014).

[139] H. Haeno, M. Gonen, M. Davis, J. Herman, C. Iacobuzio-Donahue, and F. Michor, *Computational modeling of pancreatic cancer reveals kinetics of metastasis suggesting optimum treatment strategies,* Cell **148**, 362–375 (2012).

[140] E. Campillo-Funollet, C. Venkataraman, and A. Madzvamuse, *Bayesian parameter identification for turing systems on stationary and evolving domains,* Bulletin of mathematical biology **81**, 81–104 (2019).

[141] A. Gefen, *Effects of virus size and cell stiffness on forces, work, and pressures driving membrane invagination in a receptor-mediated endocytosis,* Journal of biomechanical engineering **132**, 084501 (2010).

[142] C. L. Stokes and D. A. Lauffenburger, *Analysis of the roles of microvessel endothelial cell random motility and chemotaxis in angiogenesis,* Journal of theoretical biology **152**, 377–403 (1991).

[143] B. D. Cumming, D. McElwain, and Z. Upton, *A mathematical model of wound healing and subsequent scarring,* Journal of The Royal Society Interface **7**, 19–34 (2009).

[144] S. Kar, W. T. Baumann, M. R. Paul, and J. J. Tyson, *Exploring the roles of noise in the eukaryotic cell cycle,* Proceedings of the National Academy of Sciences **106**, 6471–6476 (2009).

[145] K. P. Olive, M. A. Jacobetz, C. J. Davidson, A. Gopinathan, D. McIntyre, D. Honess, B. Madhu, M. A. Goldgraben, M. E. Caldwell, D. Allard, *et al.*, *Inhibition of hedgehog signaling enhances delivery of chemotherapy in a mouse model of pancreatic cancer,* Science **324**, 1457–1461 (2009).

[146] D. Öhlund, A. Handly-Santana, G. Biffi, E. Elyada, A. S. Almeida, M. Ponz-Sarvise, V. Corbo, T. E. Oni, S. A. Hearn, E. J. Lee, *et al.*, *Distinct populations of inflammatory fibroblasts and myofibroblasts in pancreatic cancer,* Journal of Experimental Medicine **214**, 579–596 (2017).

[147] W. Plunkett, P. Huang, Y. Xu, V. Heinemann, R. Grunewald, and V. Gandhi, *Gemcitabine: metabolism, mechanisms of action, and self-potentiation.* in *Semin Oncol*, Vol. 22 (1995) pp. 3–10.

[148] S. Massalha and D. Weihs, *Metastatic breast cancer cells adhere strongly on varying stiffness substrates, initially without adjusting their morphology,* Biomech Model Mechanobiol **16**, 961–970 (2017).

[149] R. Merkel, N. Kirchgeßner, C. Cesa, and B. Hoffmann, *Cell force microscopy on elastic layers of finite thickness,* Biophys J **93**, 3314–3323 (2007).

[150] P. E. Kloeden and E. Platen, *Numerical solution of stochastic differential equations,* Vol. 23 (Springer Science & Business Media, 2013).

[151] J. Van Damme, J.-P. Proost, J. Lenaerts, and G. Opdenakker, *Structural and functional identification of two human, tumor-derived monocyte chemotactic proteins (mcp-2 and mcp-3) belonging to the chemokine family.* J Exp Med **176**, 59–65 (1992).

[152] M. Kershaw, G. Wang, J. Westwood, R. Pachynski, H. Tiffany, F. Marincola, E. Wang, H. Young, P. Murphy, and P. Hwu, *Redirecting migration of t cells to chemokine secreted from tumors by genetic modification with CXCR2,* Hum Gene Ther **13**, 1971–1980 (2002).

[153] F. Vermolen, *Particle methods to solve modelling problems in wound healing and tumor growth,* Comput Part Mech **2**, 381–399 (2015).

[154] G. Grimmett, D. Stirzaker, *et al.*, *Probability and random processes* (Oxford university press, 2001).

[155] D. Hanahan and R. Weinberg, *Hallmarks of cancer: the next generation,* cell **144**, 646–674 (2011).

[156] A. Rhim, P. Oberstein, D. Thomas, E. Mirek, C. Palermo, S. Sastra, E. Dekleva, T. Saunders, C. Becerra, I. Tattersall, *et al.*, *Stromal elements act to restrain, rather than support, pancreatic ductal adenocarcinoma,* Cancer cell **25**, 735–747 (2014).

[157] H. Bougherara, A. Mansuet-Lupo, M. Alifano, C. Ngô, D. Damotte, L. Frère-Belda, E. Donnadieu, E. Peranzoni, *et al.*, *Real-time imaging of resident T cells in human lung and ovarian carcinomas reveals how different tumor microenvironments control T lymphocyte migration,* Front Immunol **6**, 500 (2015).

[158] C. Feig, A. Gopinathan, A. Neesse, D. S. Chan, N. Cook, and D. A. Tuveson, *The pancreas cancer microenvironment,* (2012).

[159] A. Neesse, P. Michl, K. K. Frese, C. Feig, N. Cook, M. A. Jacobetz, M. P. Lolkema, M. Buchholz, K. P. Olive, T. M. Gress, *et al.*, *Stromal biology and therapy in pancreatic cancer,* Gut **60**, 861–868 (2011).

[160] S. Awale, J. Lu, S. Kalauni, Y. Kurashima, Y. Tezuka, S. Kadota, and H. Esumi, *Identification of arctigenin as an antitumor agent having the ability to eliminate the tolerance of cancer cells to nutrient starvation,* Cancer Res **66**, 1751–1757 (2006).

[161] M. Young, P. Carroad, and R. Bell, *Estimation of diffusion coefficients of proteins,* Biotechnol Bioeng **22**, 947–955 (1980).

[162] C. De Paiva, S. Pflugfelder, and D.-Q. Li, *Cell size correlates with phenotype and proliferative capacity in human corneal epithelial cells,* Stem cells **24**, 368–375 (2006).

[163] F. Bookholt, H. Monsuur, S. Gibbs, and F. Vermolen, *Mathematical modelling of angiogenesis using continuous cell-based models,* Biomechanics and modeling in mechanobiology **15**, 1577–1600 (2016).

[164] N. Jeon, H. Baskaran, S. Dertinger, G. Whitesides, L. Van De Water, and M. Toner, *Neutrophil chemotaxis in linear and complex gradients of interleukin-8 formed in a microfabricated device,* Nat Biotechnol **20**, 826 (2002).

[165] J. Savinell, G. Lee, and B. Palsson, *On the orders of magnitude of epigenic dynamics and monoclonal antibody production,* Bioproc Biosyst Eng **4**, 231–234 (1989).

[166] D. Lachowski, E. Cortes, D. Pink, A. Chronopoulos, S. Karim, J. Morton, and E. Armando, *Substrate rigidity controls activation and durotaxis in pancreatic stellate cells,* Sci Rep **7**, 2506 (2017).

[167] C. Z. Mooney, *Monte carlo simulation,* Vol. 116 (Sage Publications, 1997).

[168] C. Thompson, H. Shepard, P. O'Connor, S. Kadhim, P. Jiang, R. Osgood, L. Bookbinder, X. Li, B. Sugarman, R. Connor, *et al.*, *Enzymatic depletion of tumor hyaluronan induces antitumor responses in preclinical animal models,* Mol Cancer Ther , 1535–7163 (2010).

[169] J. Gore and M. Korc, *Pancreatic cancer stroma: friend or foe?* Cancer cell **25**, 711–712 (2014).

[170] M. Apte, J. Wilson, A. Lugea, and S. Pandol, *A starring role for stellate cells in the pancreatic cancer microenvironment,* Gastroenterology **144**, 1210–1219 (2013).

[171] T. Kamisawa, L. Wood, T. Itoi, and K. Takaori, *Pancreatic cancer,* The Lancet **388**, 73–85 (2016).

[172] M. Chiaravalli, M. Reni, and E. O'Reilly, *Pancreatic ductal adenocarcinoma: State-of-the-art 2017 and new therapeutic strategies,* Cancer Treat Rev **60**, 32–43 (2017).

[173] N. De Pace, *Sulla scomparsa di un enorme cancro vegetante del collo dell'utero senza cura chirurgica,* (1912).

[174] C. Levaditi and S. Nicolau, *Sur le culture du virus vaccinal dans les neoplasmes epithelieux,* CR Soc Biol **86**, 928 (1922).

[175] G. T. Pack, *Note on the experimental use of rabies vaccine for melanomatosis,* AMA archives of dermatology and syphilology **62**, 694–695 (1950).

[176] H. Kasuya, S. Takeda, S. Nomoto, and A. Nakao, *The potential of oncolytic virus therapy for pancreatic cancer,* Cancer gene therapy **12**, 725 (2005).

[177] D. Kirn, *Oncolytic virotherapy for cancer with the adenovirus dl1520 (onyx-015): results of phase i and ii trials,* Expert opinion on biological therapy **1**, 525–538 (2001).

[178] M. Gil, M. Seshadri, M. P. Komorowski, S. I. Abrams, and D. Kozbor, *Targeting cxcl12/cxcr4 signaling with oncolytic virotherapy disrupts tumor vasculature and inhibits breast cancer metastases,* Proceedings of the National Academy of Sciences **110**, E1291–E1300 (2013).

[179] M. Gil, M. P. Komorowski, M. Seshadri, H. Rokita, A. R. McGray, M. Opyrchal, K. O. Odunsi, and D. Kozbor, *Cxcl12/cxcr4 blockade by oncolytic virotherapy inhibits ovarian cancer growth by decreasing immunosuppression and targeting cancer-initiating cells,* The Journal of Immunology **193**, 5327–5337 (2014).

[180] R. L. Martuza, A. Malick, J. M. Markert, K. L. Ruffner, and D. M. Coen, *Experimental therapy of human glioma by means of a genetically engineered virus mutant,* Science **252**, 854–856 (1991).

[181] Z.-J. Xia, J.-H. Chang, L. Zhang, W.-Q. Jiang, Z.-Z. Guan, J.-W. Liu, Y. Zhang, X.-H. Hu, G.-H. Wu, H.-Q. Wang, *et al., Phase iii randomized clinical trial of intratumoral injection of e1b gene-deleted adenovirus (h101) combined with cisplatin-based chemotherapy in treating squamous cell cancer of head and neck or esophagus,* Ai zheng= Aizheng= Chinese journal of cancer **23**, 1666–1670 (2004).

[182] H. Fukuhara, Y. Ino, and T. Todo, *Oncolytic virus therapy: a new era of cancer treatment at dawn,* Cancer science **107**, 1373–1379 (2016).

[183] M. Korc, *Pancreatic cancer–associated stroma production,* The American Journal of Surgery **194**, S84–S86 (2007).

[184] F. Bray, J. Ferlay, I. Soerjomataram, R. L. Siegel, L. A. Torre, and A. Jemal, *Global cancer statistics 2018: Globocan estimates of incidence and mortality worldwide for 36 cancers in 185 countries,* CA: a cancer journal for clinicians **68**, 394–424 (2018).

[185] J. A. Moir, J. Mann, and S. A. White, *The role of pancreatic stellate cells in pancreatic cancer,* Surgical oncology **24**, 232–238 (2015).

[186] M. A. Jacobetz, D. S. Chan, A. Neesse, T. E. Bapiro, N. Cook, K. K. Frese, C. Feig, T. Nakagawa, M. E. Caldwell, H. I. Zecchini, *et al.*, *Hyaluronan impairs vascular function and drug delivery in a mouse model of pancreatic cancer,* Gut **62**, 112–120 (2013).

[187] C. S. Ilkow, M. Marguerie, C. Batenchuk, J. Mayer, D. B. Neriah, S. Cousineau, T. Falls, V. A. Jennings, M. Boileau, D. Bellamy, *et al.*, *Reciprocal cellular cross-talk within the tumor microenvironment promotes oncolytic virus activity,* Nature medicine **21**, 530 (2015).

[188] M. Sunamura, H. Hamada, F. Motoi, M. Oonuma, H. Abe, Y. Saitoh, T. Hoshida, S. Ottomo, N. Omura, and S. Matsuno, *Oncolytic virotherapy as a novel strategy for pancreatic cancer,* Pancreas **28**, 326–329 (2004).

[189] S. Wennier, S. Li, and G. McFadden, *Oncolytic virotherapy for pancreatic cancer,* Expert reviews in molecular medicine **13** (2011).

[190] X. Fu, L. Tao, M. Li, W. E. Fisher, and X. Zhang, *Effective treatment of pancreatic cancer xenografts with a conditionally replicating virus derived from type 2 herpes simplex virus,* Clinical cancer research **12**, 3152–3157 (2006).

[191] C. G. Langton, *Self-reproduction in cellular automata,* Physica D: Nonlinear Phenomena **10**, 135–144 (1984).

[192] A. Deutsch, S. Dormann, *et al.*, *Cellular automaton modeling of biological pattern formation* (Springer, 2005).

[193] E. Reis, L. Santos, and S. T. R. d. Pinho, *A cellular automata model for avascular solid tumor growth under the effect of therapy,* Physica A: Statistical Mechanics and its Applications **388**, 1303–1314 (2009).

[194] H. Hatzikirou and A. Deutsch, *Cellular automata as microscopic models of cell migration in heterogeneous environments,* Current Topics in Developmental Biology **81**, 401–434 (2008).

[195] H. Enderling, M. A. Chaplain, and P. Hahnfeldt, *Quantitative modeling of tumor dynamics and radiotherapy,* Acta biotheoretica **58**, 341–353 (2010).

[196] F. Pourhasanzade and S. Sabzpoushan, *A cellular automata model of chemotherapy effects on tumour growth: targeting cancer and immune cells,* Mathematical and Computer Modelling of Dynamical Systems , 1–27 (2019).

[197] F. Vermolen and I. Pölönen, *Uncertainty quantification on a spatial markov-chain model for the progression of skin cancer,* Accepted by Journal of Mathematical Biology (2019).

[198] D. P. Kroese, T. Brereton, T. Taimre, and Z. I. Botev, *Why the monte carlo method is so important today,* Wiley Interdisciplinary Reviews: Computational Statistics **6**, 386–392 (2014).

[199] B. Bajaj, P. Lei, and S. T. Andreadis, *High efficiencies of gene transfer with immobilized recombinant retrovirus: kinetics and optimization,* Biotechnology progress **17**, 587–596 (2001).

[200] M. Aghi and R. L. Martuza, *Oncolytic viral therapies–the clinical experience,* Oncogene **24**, 7802 (2005).

[201] D. E. Durrant, A. Das, S. Dyer, S. Tavallai, P. Dent, and R. C. Kukreja, *Targeted inhibition of phosphoinositide 3-kinase (pi3k)/mammalian target of rapamycin (mtor) sensitizes pancreatic cancer cells to doxorubicin without exacerbating cardiac toxicity,* Molecular pharmacology , mol–115 (2015).

[202] G. Wollmann, K. Ozduman, and A. N. van den Pol, *Oncolytic virus therapy of glioblastoma multiforme–concepts and candidates,* Cancer journal (Sudbury, Mass.) **18**, 69 (2012).

[203] H. Rehman, A. W. Silk, M. P. Kane, and H. L. Kaufman, *Into the clinic: talimogene laherparepvec (t-vec), a first-in-class intratumoral oncolytic viral therapy,* Journal for immunotherapy of cancer **4**, 53 (2016).

[204] T. P. Cripe, M. C. Ngo, J. I. Geller, C. U. Louis, M. A. Currier, J. M. Racadio, A. J. Towbin, C. M. Rooney, A. Pelusio, A. Moon, *et al.*, *Phase 1 study of intratumoral pexa-vec (jx-594), an oncolytic and immunotherapeutic vaccinia virus, in pediatric cancer patients,* Molecular Therapy **23**, 602–608 (2015).

[205] S. J. Russell, K.-W. Peng, and J. C. Bell, *Oncolytic virotherapy,* Nature biotechnology **30**, 658 (2012).

[206] E. Kelly and S. J. Russell, *History of oncolytic viruses: genesis to genetic engineering,* Molecular therapy **15**, 651–659 (2007).

[207] E. A. Chiocca, *Oncolytic viruses,* Nature Reviews Cancer **2**, 938 (2002).

[208] P. K. Bommareddy, M. Shettigar, and H. L. Kaufman, *Integrating oncolytic viruses in combination cancer immunotherapy,* Nature Reviews Immunology **18**, 498 (2018).

[209] K. Molnar-Kimber, L. Kaiser, and T. Toyoizumi, *Combined therapy with a chemotherapeutic agent and an oncolytic virus for killing tumor cells in a subject,* (2002), uS Patent 6,428,968.

[210] J. Chen, D. Weihs, M. Van Dijk, and F. J. Vermolen, *A phenomenological model for cell and nucleus deformation during cancer metastasis,* Biomechanics and Modeling in Mechanobiology , 1–22 (2018).

[211] D. A. Lauffenburger and A. F. Horwitz, *Cell migration: a physically integrated molecular process,* Cell **84**, 359–369 (1996).

[212] A. F. Chambers, A. C. Groom, and I. C. MacDonald, *Metastasis: dissemination and growth of cancer cells in metastatic sites,* Nat Rev Cancer **2**, 563–572 (2002).

[213] I. J. Fidler, *The pathogenesis of cancer metastasis: the'seed and soil'hypothesis revisited,* Nat Rev Cancer **3**, 453–458 (2003).

[214] A. W. Lambert, D. R. Pattabiraman, and R. A. Weinberg, *Emerging biological principles of metastasis,* Cell **168**, 670–691 (2017).

[215] T. N. Seyfried and L. C. Huysentruyt, *On the origin of cancer metastasis,* Crit Rev Oncogenesis **18**, 43 (2013).

[216] G. P. Gupta and J. Massagué, *Cancer metastasis: building a framework,* Cell **127**, 679–695 (2006).

[217] K. Paňková, D. Rösel, M. Novotnỳ, and J. Brábek, *The molecular mechanisms of transition between mesenchymal and amoeboid invasiveness in tumor cells,* Cell Mol Life Sci **67**, 63–71 (2010).

[218] E. Sahai and C. J. Marshall, *Differing modes of tumour cell invasion have distinct requirements for rho/rock signalling and extracellular proteolysis,* Nat Cell Biol **5**, 711–719 (2003).

[219] S. Pinner and E. Sahai, *Imaging amoeboid cancer cell motility in vivo,* Journal of microscopy **231**, 441–445 (2008).

[220] K. Wolf, I. Mazo, H. Leung, K. Engelke, U. H. Von Andrian, E. I. Deryugina, A. Y. Strongin, E.-B. Bröcker, and P. Friedl, *Compensation mechanism in tumor cell migration,* The Journal of cell biology **160**, 267–277 (2003).

[221] J. B. Wyckoff, S. E. Pinner, S. Gschmeissner, J. S. Condeelis, and E. Sahai, *Rock-and myosin-dependent matrix deformation enables protease-independent tumor-cell invasion in vivo,* Curr Biol **16**, 1515–1523 (2006).

[222] T. Kalebic, S. Garbisa, B. Glaser, and L. Liotta, *Basement membrane collagen: degradation by migrating endothelial cells,* Science **221**, 281–283 (1983).

[223] K. Wolf, M. Te Lindert, M. Krause, S. Alexander, J. Te Riet, A. L. Willis, R. M. Hoffman, C. G. Figdor, S. J. Weiss, and P. Friedl, *Physical limits of cell migration: control by ecm space and nuclear deformation and tuning by proteolysis and traction force,* J Cell Biol **201**, 1069–1084 (2013).

[224] C. M. Denais, R. M. Gilbert, P. Isermann, A. L. McGregor, M. te Lindert, B. Weigelin, P. M. Davidson, P. Friedl, K. Wolf, and J. Lammerding, *Nuclear envelope rupture and repair during cancer cell migration,* Science **352**, 353–358 (2016).

[225] R. Rey and J. Garcia-Aznar, *A phenomenological approach to modelling collective cell movement in 2d,* Biomech Model Mechanobiol **12**, 1089–1100 (2013).

[226] C. Borau, W. J. Polacheck, R. D. Kamm, and J. M. García-Aznar, *Probabilistic voxel-fe model for single cell motility in 3d,* In Silico Cell Tissue Sci **1**, 2 (2014).

[227] R. F. van Oers, E. G. Rens, D. J. LaValley, C. A. Reinhart-King, and R. M. Merks, *Mechanical cell-matrix feedback explains pairwise and collective endothelial cell behavior in vitro,* PLoS Comput Biol **10**, e1003774 (2014).

[228] W. Marth and A. Voigt, *Signaling networks and cell motility: a computational approach using a phase field description,* J Math Biol **69**, 91–112 (2014).

[229] F. Vermolen and A. Gefen, *A phenomenological model for chemico-mechanically induced cell shape changes during migration and cell–cell contacts,* Biomech Model Mechanobiol , 1–23 (2013).

[230] F. Vermolen, M. Mul, and A. Gefen, *Semi-stochastic cell-level computational modeling of the immune system response to bacterial infections and the effects of antibiotics,* Biomechanics and modeling in mechanobiology **13**, 713–734 (2014).

[231] T. Odenthal, B. Smeets, P. Van Liedekerke, E. Tijskens, H. Van Oosterwyck, and H. Ramon, *Analysis of initial cell spreading using mechanistic contact formulations for a deformable cell model,* PLoS computational biology **9**, e1003267 (2013).

[232] M. Tozluoğlu, A. L. Tournier, R. P. Jenkins, S. Hooper, P. A. Bates, and E. Sahai, *Matrix geometry determines optimal cancer cell migration strategy and modulates response to interventions,* Nature cell biology **15**, 751 (2013).

[233] R. Moussavi-Baygi, Y. Jamali, R. Karimi, and M. R. Mofrad, *Brownian dynamics simulation of nucleocytoplasmic transport: a coarse-grained model for the functional state of the nuclear pore complex,* PLoS computational biology **7**, e1002049 (2011).

[234] X. Cao, E. Moeendarbary, P. Isermann, P. M. Davidson, X. Wang, M. B. Chen, A. K. Burkart, J. Lammerding, R. D. Kamm, and V. B. Shenoy, *A chemomechanical model for nuclear morphology and stresses during cell transendothelial migration,* Biophysical journal **111**, 1541–1552 (2016).

[235] P. Friedl, K. Wolf, and J. Lammerding, *Nuclear mechanics during cell migration,* Current opinion in cell biology **23**, 55–64 (2011).

[236] J. Galle, M. Loeffler, and D. Drasdo, *Modeling the effect of deregulated proliferation and apoptosis on the growth dynamics of epithelial cell populations in vitro,* Biophysical journal **88**, 62–75 (2005).

[237] D. Drasdo, R. Kree, and J. McCaskill, *Monte carlo approach to tissue-cell populations,* Physical review E **52**, 6635 (1995).

[238] G. Odell, G. Oster, B. Burnside, and P. Alberch, *A mechanical model for epithelial morphogenesis,* Journal of mathematical biology **9**, 291–295 (1980).

[239] C. D. Paul, P. Mistriotis, and K. Konstantopoulos, *Cancer cell motility: lessons from migration in confined spaces,* Nat Rev Cancer **17**, 131–140 (2017).

[240] M. Mak and D. Erickson, *A serial micropipette microfluidic device with applications to cancer cell repeated deformation studies,* Integr Biol **5**, 1374–1384 (2013).

[241] J. M. Steele, *Stochastic calculus and financial applications*, Vol. 45 (Springer Science & Business Media, 2012).

[242] J. A. Champion and S. Mitragotri, *Role of target geometry in phagocytosis,* P Natl Acad Sci USA **103**, 4930–4934 (2006).

[243] S. Jayaraman, N. S. Joo, B. Reitz, J. J. Wine, and A. Verkman, *Submucosal gland secretions in airways from cystic fibrosis patients have normal [na+] and ph but elevated viscosity,* Proceedings of the National Academy of Sciences **98**, 8119–8123 (2001).

[244] C. A. Brunner, A. Ehrlicher, B. Kohlstrunk, D. Knebel, J. A. Käs, and M. Goegler, *Cell migration through small gaps,* Eur Biophys J **35**, 713–719 (2006).

[245] M. Mak, C. A. Reinhart-King, and D. Erickson, *Elucidating mechanical transition effects of invading cancer cells with a subnucleus-scaled microfluidic serial dimensional modulation device,* Lab Chip **13**, 340–348 (2013).

[246] C. D. Paul, W.-C. Hung, D. Wirtz, and K. Konstantopoulos, *Engineered models of confined cell migration,* Annual review of biomedical engineering **18**, 159–180 (2016).

[247] M.-E. Myrand-Lapierre, X. Deng, R. R. Ang, K. Matthews, A. T. Santoso, and H. Ma, *Multiplexed fluidic plunger mechanism for the measurement of red blood cell deformability,* Lab Chip **15**, 159–167 (2015).

[248] K. Wolf, S. Alexander, V. Schacht, L. M. Coussens, U. H. von Andrian, J. van Rheenen, E. Deryugina, and P. Friedl, *Collagen-based cell migration models in vitro and in vivo,* in *Seminars in cell & developmental biology* (Elsevier, 2009).

[249] T. A. Springer, *Traffic signals for lymphocyte recirculation and leukocyte emigration: the multistep paradigm,* Cell **76**, 301–314 (1994).

[250] A. Chambers, A. Groom, and I. MacDonald, *â€ dissemination and growth of cancer cells in metastatic sites, â€ nat,* Rev. Cancer **2**, 563ā (2002).

[251] L. Kopfstein and G. Christofori, *Metastasis: cell-autonomous mechanisms versus contributions by the tumor microenvironment,* CMLS-Cell Mol Life S **63**, 449–468 (2006).

[252] T. Celià-Terrassa and Y. Kang, *Distinctive properties of metastasis-initiating cells,* Gene Dev **30**, 892–908 (2016).

[253] K. J. Luzzi, I. C. MacDonald, E. E. Schmidt, N. Kerkvliet, V. L. Morris, A. F. Chambers, and A. C. Groom, *Multistep nature of metastatic inefficiency: dormancy of solitary cells after successful extravasation and limited survival of early micrometastases,* The American journal of pathology **153**, 865–873 (1998).

[254] C. P. Huang, J. Lu, H. Seon, A. P. Lee, L. A. Flanagan, H.-Y. Kim, A. J. Putnam, and N. L. Jeon, *Engineering microscale cellular niches for three-dimensional multicellular co-cultures,* Lab on a Chip **9**, 1740–1748 (2009).

[255] I. K. Zervantonakis, S. K. Hughes-Alford, J. L. Charest, J. S. Condeelis, F. B. Gertler, and R. D. Kamm, *Three-dimensional microfluidic model for tumor cell intravasation and endothelial barrier function,* Proceedings of the National Academy of Sciences **109**, 13515–13520 (2012).

[256] S. Mahadevan, *Monte carlo simulation,* Mechanical engineering-New York and Basel-Marcel Dekker- , 123–146 (1997).

[257] P. M. Davidson, C. Denais, M. C. Bakshi, and J. Lammerding, *Nuclear deformability constitutes a rate-limiting step during cell migration in 3-d environments,* Cell Mol Bioeng **7**, 293–306 (2014).

[258] S. Abuhattum and D. Weihs, *Asymmetry in traction forces produced by migrating preadipocytes is bounded to 33%,* Med Eng Phy **38**, 834–838 (2016).

[259] F. Serrano-Alcalde, J. M. García-Aznar, and M. J. Gómez-Benito, *The role of nuclear mechanics in cell deformation under creeping flows,* Journal of theoretical biology **432**, 25–32 (2017).

[260] C. Giverso, A. Arduino, and L. Preziosi, *How nucleus mechanics and ecm microstructure influence the invasion of single cells and multicellular aggregates,* Bulletin of mathematical biology , 1–29 (2017).

[261] T. Lämmermann and M. Sixt, *Mechanical modes of 'amoeboid'cell migration,* Curr Opin Cell Biol **21**, 636–644 (2009).

[262] P. Zhao, W. Zhang, S.-J. Wang, X.-L. Yu, J. Tang, W. Huang, Y. Li, H.-Y. Cui, Y.-S. Guo, J. Tavernier, *et al.*, *Hab18g/cd147 promotes cell motility by regulating annexin ii-activated rhoa and rac1 signaling pathways in hepatocellular carcinoma cells,* Hepatology **54**, 2012–2024 (2011).

[263] E. Sahai, *Illuminating the metastatic process,* Nat Rev Cancer **7**, 737–749 (2007).

[264] J. Chen, D. Weihs, and F. J. Vermolen, *A model for cell migration in non-isotropic fibrin networks with an application to pancreatic tumor islets,* Biomech Model Mechanobiol , 1–20 (2017).

[265] J. Guck, S. Schinkinger, B. Lincoln, F. Wottawah, S. Ebert, M. Romeyke, D. Lenz, H. M. Erickson, R. Ananthakrishnan, D. Mitchell, *et al.*, *Optical deformability as an inherent cell marker for testing malignant transformation and metastatic competence,* Biophys J **88**, 3689–3698 (2005).

ACKNOWLEDGEMENTS

Time is fleeting, and soon I will end my PhD research in the Department of Applied Mathematics at Delft University of Technology, the Netherlands. As a biologist before, I never dared to think that one day I can graduate from the Department of Mathematics. For the interdisciplinary research, I had laughter and tears in the past four years, importantly, I have been accompanied, helped and supported by a number of people. Herewith I would like to express my gratitude to everyone.

First of all, I would like to extend my sincere gratitude to Dr. **Fred Vermolen**, who is one of my promoters and daily supervisor. I am very grateful that Fred gave me this opportunity to explore the sparks provoked by mathematics and biology. He taught me gently and patiently on how to use mathematics as a powerful tool to research biomedical science. Fred has always encouraged me to be confident whenever I have difficulties and frustrations during my PhD period. At many international conferences, he praised my oral presentations and built the bridge connecting me with other fellows. Besides academic research, Fred also helped me, as a good friend, regarding small issues and gave me lots of tips to survive better in the Netherlands. I feel pretty lucky and honored that I complete my PhD with his supervision and I think I could not have a better supervisor than him in my PhD life.

I would like to thank Prof. **Kees Vuik** for supporting me as one of my promoters. As the head of the section of Numerical Analysis, he provided me with a very wonderful academic environment and atmosphere. Kees is friendly to me and he never hesitated to help me whenever I need his help. I also want to thank DIAM department for the financial support for my doctoral education courses and conferences. Moreover, My great appreciation also goes to my co-supervisor Dr. **Daphne Weihs**. She is working in the Faculty of Biomedical Engineering at Technion-Israel Institute of Technology in Israel. For quite a long time, we had a monthly meeting by Skype and she helped me understand the biomedical phenomenon and gave me a lot of guidance from an experimental perspective in order to improve our mathematical models. In addition, I really grateful that she helped me a lot in terms of scientific writing and shared many valuables advises with me.

I greatly appreciate committee members for reading my thesis and accepting the invitation to my defense: Prof. **Arnold Heemink** and Prof. **Amir Zad-**

poor. I would like to thank Prof. **Lies Geris** for her encouraged and kind words at the SIAM workshop day 2017. Special thanks to Prof. **Anotida Madzvamuse**, who encouraged me at the AIMS 2018 conference that I am really grateful. Regarding official affairs and technical support, my appreciation goes to **Deborah Dongor**, **Kees Lemmens**, **Xiwei Wu**, **Carl Schneider** and **Wim van Horssen**. My special thanks go to **Cees Timmers** and **Franca Post** who helped me with my CSC scholarship application and relevant affairs. Certainly, I want to acknowledge to **China Scholarship Council** for offering me the CSC scholarship. Without financial support from China Scholarship Council, it is impossible for me to finish this wonderful PhD research in the Netherlands.

I sincerely thank Prof. **Ed van Bavel** in Amsterdam UMC, who arranged me interviews and offered me a Postdoc position in the Department of Biomedical Engineer and Physics. I was anxious and frustrated when I was looking for a position in the Netherlands since the opportunities are scarce and precious. I had many pleasant conversations with Ed, and he shared his experience on how to continue academia after PhD research with me. I appreaciate his encouragement and recognition. My new project is challenging, I am looking forward to working in collaboration with Ed.

Next, I want to thank my lovely office mates **Gabriela** and **Luis** for sharing Mexican foods and cultures with me. **Shuaiqiang**, thanks for your kind encouragements when I felt depressed and thanks for sharing your knowledge, opinions and homemade food. I also want to thank **Anne** for inviting me to her apartment for parties and adorable cats. Thanks to **Lisa**, I heard many interesting and exotic stories about Russia and thank you for sharing your happiness and sorrows with me. My thanks also goes to **Thomas**, who gave me smiles and some advice regarding looking for a job in a Dutch bank. Thank you **Hugo** for helping me with the Dutch translation of my thesis propositions, I liked the small chats with you and your jokes. I also want to thank **Luyu** for his snacks and tea from China.

I would like to acknowledge all my other cool colleagues in TU Delft: **Baljinnyam, Berna, Behrouz, Ginger, Giordano, Jing, Jochan, Lin, Menel, Mohamed, Marieke, Merel, Mousa, Peiyao, Prajatka, Qiyao, Reinaldo, Roel, Thea, Vandana, Xiujie, Yue, Zaza**. I also want to express my gratitude to **Domenico, Duncan, Deepesh, Joanna, Kees Osterlee, Kristof, Matthias, Martin, Neil**. In the past years, I got lots of help and suggestions from some of you and I had memorable moments with some of you. We had coffee/tea breaks, group lunches, various cakes, and homemade food whenever it is necessary. It is my great pleasure to spend my PhD life with you guys.

During 2016-2017, I was a board member, as a treasurer, of SIAM Student Chapter Delft. I have learned a lot from other board members **Anne, Gabriela, Patrick** and **Jörn** and we successfully organized some international scientific and social activities.

My Chinese friends in the Netherlands have brought me lots of laughter and happy time, which I cherish so much. Special thanks to **Meng, Yin** and **Tian**, we have spent much time together on exploring many places of the Netherlands and feeding each other homemade Chinese cuisine. The cold Dutch winter is full of wind and rain, but the moments were warm when we were playing Mahjong. I appreciate the help and kindness from **Jiakun** and **Xiaoyan**, who have a cute boy now. I liked to play a card game called 'Guandan' with card masters, **Qian, Xinmin** and **Ding**. Thanks to table tennis, I met many fellows and afterward we became close friends during practicing. Among them, I would thank **Jin** for helping me improve my table tennis skills and I enjoyed what **Yun** told about their previous love stories. **Flora** and **Yu** also helped me with Table tennis training. I was deeply impressed by the Korean BBQ prepared by **Wenjie** and **Xiangrong**, which was so delicious. **Junru** and **Xiaolin**, as a role model, told us how to balance life and work while taking care of two children. Since **Peiyao, Jing, Shuaiqiang, Lu** and I have lived in the same city Xi'an, we have endless topics to discuss every time we meet. I also had a great time chatting with **Shan, Ulaş**, and **Bolin**. Due to the relocation of the department of mathematics, I got a chance to know some Chinese friends **Senlei, Renfei** and **Xiao**. Thanks **Hong** and **Dongbin** inviting me to their house, where I met a lovely dog **Cindy**. I also want to thank **Hongxiao** for taking care of photography during my defense.

I have never regretted joining the Association of Chinese students and scholars (ACSSNL) in the Netherlands and served for the association for three years. I am very grateful to Chinese Embassy in the Netherlands for inviting me to participate in the New Year receptions and other wonderful events. I also would like to thank the Counsellor **Qingyu** and also **Yiwei, Xiaoxiao, Qianqian, Feifei, Wei** and **Tao** of the Education Office of the Embassy for their help and concern. As the leader of ACSSNL-Delft branch during 2015-2016, I was acquainted with many Chinese fellows: **Xinyuan, Yili, Chulin, Zhili, Xuliang, Hai, Shuai, Youwei, Zhihong, Yan, Mingzhao** and our experience in organizing events was very beautiful. Since 2016, I have been a director of CSC affairs in ACSSNL, I met more Chinese friends in the Netherlands, like **Qiyao, Yuxin, Haopeng, Liangfu** in Delft, **Xiaomei, Lingtong, Han, Quanxing** in Wageningen, **Guannan** in Rotterdam, **Yawen** in Eindhoven, **Huatang** in Groningen.

Last but not least, I would like to express my great gratitude to my husband **Fei** for his love and accompany. On the road of mathematical research, he shared lots of his experience with me regarding how to understand some mathematical concepts better and how to be patient during debugging. He is the spiritual pillar of my insistence on interdisciplinary research. In daily life, he helped me, tolerated me, comforted me, encouraged me, and facilitated me to become better my-self. In addition, I also really want to thank my **parents**, my younger **brother** and **parents-in-law** for their wholehearted support. Their comfort and care eased my homesickness a lot and I am very touched by what they have done for me. All in all, I love you all.

Jiao Chen
Delft, the Netherlands
December, 2019

CURRICULUM VITÆ

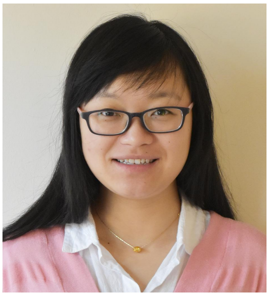

Jiao CHEN

05-Jan-1988	Born in Xian Yang, Shaanxi, China.

EDUCATION

2007–2011	B.Sc in Biotechnology Northwest University, Xi'an, China
2011–2014	M.Sc in Biochemistry and Molecular Biology Northwest A&F University, YangLing, China
2015–2019	Ph.D in Applied Mathematics Delft University of Technology, Delft, The Netherlands *Thesis*: 'Agent-based mathematical modeling of pancreatic cancer growth and several therapies'

WORK EXPERIENCE

2020–	Postdoc in the Department of Biomedical Engineering and Physics Amsterdam UMC, The Netherlands

LIST OF PUBLICATIONS

- **Publications in Refereed Journals**

  1. **J. Chen**, D. Weihs and F. J. Vermolen. *A cellular automata model of oncolytic virotherapy in pancreatic cancer*, **Submitted**.
  2. **J. Chen**, D. Weihs and F. J. Vermolen. *Computational modeling of therapy on initial pancreatic cancer*, Biomehcanics and modeling in mechanobiology, **1-18**, 2019.
  3. **J. Chen**, D. Weihs, M. Van Dijk and F. J. Vermolen *A phenomenological model for cell and nucleus deformation during cancer metastasis*, Biomehcanics and modeling in mechanobiology, **17 (5)**, 1429-1450, 2018.
  4. **J. Chen**, D. Weihs and F. J. Vermolen. *A model for cell migration in non-isotropic fibrin networks with an application to pancreatic tumor islets*, Biomehcanics and modeling in mechanobiology, **17 (2)**, 367-386, 2018.

- **Book Chapter**

  1. **J. Chen**, D. Weihs and F. J. Vermolen. *Computational cell-based modeling and visulization of cancer development and progression*, In New Developments on Computational Methods and Imaging in Biomechanics and Biomedical Engineering, pp. 93-119. Springer, Cham., 2019.

- **Publications in Refereed Proceedings**

  1. **J. Chen**, D. Weihs and F. J. Vermolen. *Monte Carlo uncertainty quantification in modeling cell deformation during cancer metastasis*, In CMBBE Conference Proceedings, 2018.
  2. **J. Chen** and F. J. Vermolen. *Several agent-based and cellular automata mathematical frameworks for modeling pancreatic cancer*, In ENUMATH Conference Proceeings, 2019.

- **Technical Report**

  1. **J. Chen** and F. J. Vermolen. *Literature study on cell-based semi-stochastic modeling for the dynamics of growth of cell colonies*, Delft University of Technology, 2016.

LIST OF PRESENTATIONS

- **Oral Presentations**
    1. European Numerical Mathematics and Advanced Applications Conference, Egmond aan Zee, The Netherlands, October 2019.
    2. 16th International Symposium on Computer Methods in Biomechanics and Biomedical Engineering and 4th Conference on Imaging and Visualization, New York City, USA, August 2019.
    3. The 12th AIMS Conference on Dynamical Systems, Differential Equations and Applications, Taipei, Taiwan, July 2018.
    4. 15th International Symposium on Computer Methods in Biomechanics and Biomedical Engineering and 3rd Conference on Imaging and Visualization, Lisbon, Portugal, March 2018.
    5. V International Conference on Particle-based Methods, Hannover, Germany, September 2017.
    6. SIAM Annual Meeting, Pittsburgh, USA, July 2017.
    7. Workshop 'Mathematical Modelling in Medicine Day', Delft, The Netherlands, May 2017.
- **Poster Presentations**
    1. The 44th Woundschoten conference, Zeist, The Netherlands, 2019.
    2. The 42th Woundschoten conference, Zeist, The Netherlands, 2017.
    3. The 41th Woundschoten conference, Zeist, The Netherlands, 2016.